1-1-2017

A Computational Study of Diesel and Diesel-Methane Dual Fuel Combustion in a Single-Cylinder Research Engine

Prabhat Ranjan Jha

A computational study of diesel and diesel-methane dual fuel combustion in a single-cylinder research engine

By

Prabhat Ranjan Jha

A Thesis
Submitted to the Faculty of
Mississippi State University
in Partial Fulfillment of the Requirements
for the Degree of Master of Science
in Mechanical Engineering
in the Department of Mechanical Engineering

Mississippi State, Mississippi

August 2017

A computational study of diesel and diesel-methane dual fuel combustion in a single-cylinder research engine

By

Prabhat Ranjan Jha

Approved:

_____

Sundar R. Krishnan
(Major Professor)

_____

Kalyan K. Srinivasan
(Minor Professor)

_____

Pedro J. Mago
(Committee Member)

_____

Yucheng Liu
(Graduate Coordinator)

_____

Jason M. Keith
Dean
Bagley College of Engineering

Name: Prabhat Ranjan Jha

Date of Degree: August 11, 2017

Institution: Mississippi State University

Major Field: Mechanical Engineering

Major Professor: Sundar R. Krishnan

Title of Study: A computational study of diesel and diesel-methane dual fuel combustion in a single-cylinder research engine

Pages in Study 114

Candidate for Degree of Master of Science

Dual fuel combustion is one strategy to achieve low oxides of nitrogen and soot emissions while maintaining the fuel conversion efficiency of IC engines. However, it also suffers from high engine-out carbon monoxide and unburned hydrocarbon emissions, and the incidence of knock at high loads.

The present work focused on CFD simulation of diesel-methane dual fuel combustion in a single-cylinder research engine (SCRE). For pure diesel combustion, a load sweep of 2.5 bar brake mean effective pressure (BMEP) to 7.5 bar BMEP was performed at a constant engine speed of 1500 rpm and a diesel injection pressure of 500 bar. For diesel-methane dual fuel combustion, a methane percent energy substitution sweep was performed from 30% to 90 % at 1500 rpm, 3.3 bar BMEP, 500 bar P_{inj}, and 355 crank angle degrees (CAD) diesel injection timing. Combustion, performance, and emissions results are presented and compared with experimental data where possible.

ACKNOWLEDGEMENTS

I would like to acknowledge my major professor Dr. Sundar R. Krishnan and co-major professor Dr. Kalyan K. Srinivasan for their excellent guidance, support, and Patient. I truly appreciated their advice and encouragement from day one. Thank you to Dr. Pedro J. Mago for readily agreeing to serve on my thesis committee. I am also grateful to my colleagues Hamid Mahabadipour, Kendyl Partridge and Michelle N. Price for their assistance in performing this work.

I would like to thank Convergent Science for giving us free copy of license to perform these work. The author gratefully acknowledges the support of the facilities support from High Performance Computing Collaboratory (HPC^2) at Mississippi State university. I would also like to thanks all academic staff and faculty at Mechanical department in the Bagley College of Engineering.

I would like to express my profound gratitude to my parents for their unconditional love, moral support and encouragement throughout this project period. I would therefore like to dedicate this thesis to my parents Jibachh Jha and Rekha Devi Jha

.

TABLE OF CONTENTS

LIST OF TABLES

LIST OF FIGURES

CHAPTER I

INTRODUCTION

1.1 Background

Diesel engines, due to their high fuel conversion efficiencies, robustness, and dependability, are the most preferred IC engines for heavy-duty applications. However, diesel engines produce pollutants like PM and NOx, which are very difficult to reduce simultaneously within the engine cylinders using conventional diesel combustion strategies. These pollutants are harmful not just for the environment but also to human health. Therefore, aftertreatment devices are used to reduce the tailpipe emissions of NOx and PM; however, aftertreatment devices are also expensive and result in fuel penalties. These drawbacks, coupled with the increasingly stringent engine emissions standards coupled with the requirements of high fuel conversion efficiencies by both engine manufacturers (for retaining their competitive edge) and customer fleets, alternative strategies for emissions reduction are desirable. One way to reduce engine exhaust emissions like PM and NOx simultaneously is by resorting to diesel-natural gas dual fuel combustion [1,2]. Recent EPA regulations call to reduce greenhouse gases while simultaneously increasing fuel efficiency for light duty trucks and will almost by double by 2025 from the 2011 value [3]. Many of these requirements can be achieved by using alternative fuels, like natural gas, in an advanced combustion strategy. Using premixed gaseous fuels as the primary fuel that replaces diesel fuel helps to decrease

local equivalence ratios and in-cylinder combustion temperatures, thereby lowering NOx and PM emissions. Natural gas is a good substitute for fossil fuels, especially when oil prices are high [3]. Due to the widespread availability of natural gas and the continuous growth in natural gas production in the US [3], natural gas is a leading alternative fuel to petroleum-based fuels. The main constituent of natural gas is methane. Theoretically, methane combustion can achieve the same energy output as diesel, with much less carbon dioxide (CO_2) production. This, combined with the fact that diesel engines can be directly used with minor modifications in the dual fuel combustion mode, methane (i.e., natural gas) is a leading candidate for the dual fuel combustion strategy. Methane (a low-cetane primary fuel) can be injected (or fumigated) directly into intake manifold, and diesel (a high-cetane secondary fuel) can be used as an ignition source for combustion initiation. If the initial cost can be justified by saving money in fuel costs using dual fuel engines, it can be one way to achieve better fuel economy with cleaner combustion. With that said, diesel-methane dual fuel combustion has its own problems of knock at high load and high HC and CO emissions at low loads. Many research efforts have attempted to find the causes of above problems [3-7]. Methane is the primary component of the HC emissions arising from diesel-methane dual fuel combustion. Since methane has a global warming potential 25 times greater than that of CO_2 over a 100 year period; methane emissions are a major concern even though methane is not currently regulated by the EPA[8].

Computational fluid dynamics serves as a good tool to study combustion inside of the cylinder while also gaining a better understanding of the physics of combustion. With improved understanding of combustion, it is easier to devise strategies for

alleviating the problems faced in IC engines. With increasing computational resources and capabilities, CFD's influence continues to increase with time and is helping achieve optimal combustion strategies for IC engines. Development of better reaction mechanisms and models has encouraged the development of computational models to simulate diesel-methane dual fuel engines. The aim of this study is to validate CFD models and sub models in CONVERGE CFD software against available engine experimental data for in-cylinder pressure, apparent heat release rate, NOx, HC and CO emissions, and combustion phasing (CA50). It also aims to analyze combustion characteristics of pure diesel and diesel-methane dual fuel combustion. To achieve this, a 3D scan of the piston was done to obtain a piston profile of a single cylinder research engine (SCRE). The obtained profile was fed into Converge Studio, resulting in a 45-degree sector mesh. Since the injector had 8 nozzle holes, the engine computational domain was divided into 8 parts (considering symmetry) to save computational time. Injector tip penetration was also measured. CONVERGE CFD was used to simulate engine combustion from intake valve closing (IVC) to exhaust valve opening (EVO). The compression ratio was determining by running a motoring (non-firing) simulation with available experimental pressure data. Different model parameters were calibrated like the modified Kelvin-Helmholtz (KH) and the Rayleigh-Taylor (RT) spray breakup models to represent atomization and breakup inside cylinder due to in-cylinder characteristics. All sub models were calibrated for pure diesel experimental data for various loads (BMEPs from 2.5 bar to 7.5 bar) at two different rail pressures of 500 bar and 1300 bar. Then, using the same model constants (except the constants for the

modified KH-RT spray breakup model), dual fuel combustion was simulated for varying methane PES from 30 to 90.

1.2 Organization of the work

This work is organized into different chapters that assist in understanding the simulation of pure diesel and diesel-methane dual fuel combustion.

The second chapter reviews the currently available published literature on diesel and dual fuel engine combustion phenomena and dual fuel combustion modeling. The third chapter explain different governing equation, models and sub models used in this simulation work. It also includes methodology applied to perform in-cylinder computational study. Fourth chapter discuss results obtain from simulation of pure diesel and diesel-methane cases and compares it with experimentally available data. A brief parametric study is also discussed in fourth chapter. Fifth chapter include conclusion and recommendation for future work.

CHAPTER II

LITERATURE REVIEW

In conventional direct injection (DI) diesel engines, diesel is introduced to the combustion chamber just before top dead center (TDC) in the compression stroke. High injection pressures are used and fuel atomization and evaporation occur in sequence, eventually leading to combustion after an ignition delay period (composed of both physical and chemical components) [10]. According to Heywood, conventional DI engine heat release profiles can be categorized into four distinct stages: Ignition delay, rapid combustion phase, mixing controlled combustion phase, and late combustion phase [10]. More recently, Dec's model of diesel combustion [11] is widely accepted as a conceptual model of combustion phenomena occurring in modern diesel compression ignition engine that utilize high-pressure common-rail injection systems. Dec used a wide variety of laser and optical imaging tools to study in-cylinder combustion phenomena. In conventional diesel combustion, the fuel-air mixture first starts as a very rich mixture, especially in the interior regions of the diesel jet (with fuel-air equivalence ratios in the range of $2 < \Phi < 4$), and then moves towards a more stoichiometric mixture ($\Phi \sim 1$) [11-12]. Dec explains that the formation of NOx takes place near the periphery of the diffusion flame, which is stoichiometric, while particulate matter (PM) or soot is formed in the rich interior regions of the fuel jet. Despite significant research efforts over the past several decades, it is generally accepted that engine-out exhaust emissions from

conventional diesel combustion engines cannot be reduced (while employing only in-cylinder emissions reduction strategies) to meet present and future emissions regulations both within the United States and other parts of the world. Consequently, exhaust aftertreatment devices are used to treat raw engine exhaust to reduce NOx and PM emissions. Examples of such devices are the urea-based selective catalytic reduction (SCR) and diesel particulate filter (DPF) systems, which are used for NOx and PM reduction, respectively. These devices are not without their disadvantages; for example, they require regular maintenance and have high initial costs and additional operating costs (e.g., urea-based diesel exhaust fluid for the SCR). To eliminate or to reduce the use of aftertreatment devices, the formation of pollutants inside the cylinder must be controlled. This requires a thorough understanding of the in-cylinder combustion mechanics.

With better understanding of the In-cylinder combustion, past research focused on achieving homogeneous combustion at lean equivalence ratios (to avoid the formation of soot) and at lower local temperatures (to avoid the formation of NOx). For example, in the homogenous charge compression ignition (HCCI) concept, fuel is homogenously mixed with air well before the start of combustion. This is one way to reduce both NOx and soot simultaneously; however, it is limited by poor combustion efficiencies at low loads and high pressure rise rates at high loads [12]. Another popular concept to achieve low NOx and soot emissions is partially premixed compression ignition (PPCI) combustion, in which the charge is less homogenously distributed when compared to HCCI, but this mode has issues with high CO and HC emissions [18]. Other low

emission strategies are presented by Hanson et al. 2010, Northrop et al. 2009, and Splitter et al. 2010 [14-16].

To address the high NO and soot levels, several alternative fuels have been used to decrease exhaust emissions and to achieve fuel conversion efficiencies similar to conventional diesel combustion. Krishnan et al. achieved very low NOx values by using natural gas as primary fuel with early direct injection of a very small quantity of diesel being used as a pilot fuel to ignite the natural gas-air mixture [13]. Other alternative fuels such as propane, ethane, biodiesel, etc., have been used by different researchers to achieve similar results [3-7, 13, 19-23]. In dual fuel engines, the primary fuel, which has a low-cetane number, is injected either through a port or directly into the combustion chamber to form a premixed charge, while the secondary fuel with a high-cetane number is used as a pilot to ignite the premixed charge. Diesel-methane [23], Diesel-propane [22], soy-based methyl-easter biodiesel diesel [15] and natural gas-diesel [2], among others, are some of the popular fuel combinations. There are three ways of introducing gaseous fuels in diesel engines: (i) gaseous fuel inducted in the intake manifold with liquid fuel, such as diesel, used as a pilot through direct injection; (ii) high pressure direct injection of gaseous fuel into the cylinder, which is ignited by direct injection of liquid fuel; (iii) gaseous fuel is ignited by using a hot ignition source like a glow plug [24].

The concept of dual fuel combustion is explained by Karim 2003 [23]. According to Karim 2003, the heat release shape in conventional dual fuel combustion can be considered to consist of three overlapping components. The first component is due to combustion of the pilot fuel, the second is due to the gaseous fuel present near the ignition zone, and the third is due to the pre-ignition reaction activity and flame

propagation [21]. Wei and Geng [4] have performed a literature review of dual fuel engines. A summary of this literature review, describing the effects of duel fuel combustion strategy on exhaust emissions is given below.

In diesel engines, most of the fuel is consumed during the mixing control combustion phase. In dual fuel combustion, however, there is little to no mixing controlled combustion. Flame propagation of the gaseous fuel (e.g., natural gas) occurs in dual fuel mode. NOx formation is reduced due to longer ignition delays, combined with lower combustion temperatures. The specific heat ratio of natural gas is also higher than air, which decreases mean temperatures at the end of the compression stroke, thereby adding to the reduction of NOx. The CO emissions increase with dual fuel combustion due to four main reasons: firstly, competition between HC and CO oxidation; secondly, some regions within cylinder are too lean to sustain flame propagation; thirdly some gaseous fuel can be trapped in crevices, leading to higher amounts of HC that may or may not be partially oxidized by the end of combustion; lastly, due to natural gas present in the quench layer due to long residence times within the cylinder. There are tradeoffs between HC and NOx emissions in diesel-natural gas dual fuel combustion. There is an increase in HC emissions due to trapped natural gas in the crevice regions, the quench layers within the cylinder, and the flame not able to sustain itself at locally lean conditions. It was also found that most of the HC emissions for diesel-natural gas dual fuel combustion was unburned methane. The CO_2 emissions decrease because natural gas has a lower carbon-to-hydrogen (C/H) ratio and because there may be incomplete oxidation of CO formed in the combustion process to CO_2. Due to the longer ignition delays associated with dual fuel combustion, the time available for fuel-air

mixing is higher, which reduces the local equivalence ratios, thereby reducing PM formation.

Compared to diesel combustion, dual fuel combustion has a high coefficient of variation of indicated mean effective pressure (COVIMEP) due to increasing variations in the ignition and flame propagation processes; the higher COVIMEP is more pronounced at higher gaseous fuel substitutions. In one conventional dual fuel combustion study [3], the maximum COVIMEP was found to be 12% at 95 percentage energy substitution (PES) and it was also found that COVIMEP increases with increasing PES of natural gas. Fredrick et al. [25] studied the effect of in cylinder flows on emissions, heat release, and combustion characteristics of dual fuel combustion. They found that with increasing swirl ratio, the oxidation of hydrocarbons and combustion efficiencies increased [25].

There are various parameters that affect the combustion characteristics and emissions of a dual fuel engine. To improve emissions and performance, a detailed knowledge of the dual fuel combustion process is needed. Numerical studies can play a vital role in achieving this goal. Several numerical studies have been performed to understand dual fuel combustion. For example, Singh et al. [26] used the KIVA -3V code to simulate dual fuel combustion up to 90 PES of natural gas and studied the effect of intake temperature on combustion and emissions. The experimentally observed decrease in NOx and increase in HC with increased natural gas substitution was captured by the simulations. Zhang et al. [27] used a sector mesh to simulate dual fuel combustion and found that diesel fuel quantity, injection timing, and the rate of injection have a significant influence on emissions. The characteristic time combustion model was used

to simulate dual fuel combustion by Donateo et al. [28] to observe the effects of piston bowl geometry on emissions. Not only are numerical simulations cheaper than experiments, but they also reduce the time needed to obtain a fundamental understanding, from which future experiments can be performed. Other researchers have also used other combustion models and software such as ECFM-3Z (in STAR-CD), AVL fire ESE, KIVA-3V, among others, to simulate dual fuel combustion and to perform parametric studies [29-32]. The effects of natural gas on the chemical kinetics of diesel is explained by Wang et al. [33]. It was found that initial temperatures have a more significant effect on the ignition of n-heptane than the simple dilution effect of methane. Many researchers have developed reduced chemical kinetic mechanisms for dual fuel combustion. For example, Rahimi et al. [34] have optimized the chemical kinetic mechanisms available for n-heptane and natural gas to be used for simulating dual fuel combustion [34]. A genetic algorithm-based approach was used to optimize the combined chemical kinetics mechanism for n-heptane and natural gas to arrive at a reduced kinetic mechanism, which includes 76 chemical species and 464 reactions. This mechanism was used by Sameera et al. [35] and they found good prediction results for large bore medium speed diesel-natural gas dual fuel combustion.

CHAPTER III

COMPUTATIONAL TOOL OVERVIEW AND ENGINE MODELING

3.1 Computational Modeling

The engine CFD software CONVERGECFD 2.3 was used to perform the computational simulations of the single cylinder research engine (SCRE). For a given grid and control parameters, CONVERGE automatically generates the appropriate orthogonal structured grid at runtime. This feature of CONVERGE was very helpful in setting up moving boundary problems such as those encountered in internal combustion engines.

3.1.1 Gridding Method

CONVERGE uses a modified cut-cell Cartesian grid generation method to automatically generate the computational grid at runtime [36]. Converge requires only surface geometry represented as a closed triangulated surface. It saves user time to a great extent and only requires information about the various boundary surfaces in the surface file. Converge provides complete user control over the mesh resolution by easily changing the global mesh resolution and the local mesh resolution by providing additional files to control fixed embedding, Adaptive Mesh Refinement (AMR), and grid scaling [36].

The Single Cylinder Research Engine (SCRE) is equipped with a diesel injector with 8 nozzle holes; so, a $1/8^{th}$ sector of the cylinder is utilized for simulation such that

each sector includes the diesel spray plume emanating from one nozzle hole of the injector. In this work AMR and fixed embedding are utilized to obtain finer mesh where and when required to get better accuracy at reasonable computational cost. The base grid is taken to be 1.4 mm in all three directions. Fixed embedding is applied to the piston, the cylinder head and the nozzle region for all simulations. Senecal et al. [37] recommended that the optimum grid size for spray simulations was 0.25 mm, keeping in mind both accuracy and computational cost. With the above recommendation, fixed embedding around nozzle to resolve spray is used with a minimum grid size of 0.25 mm. Around the boundary and the cylinder head, fixed embedding is employed with a minimum grid size of 0.5 mm. To resolve the flow field instead of globally embedding the grid, it is more economical to locally add higher grid resolution in the regions where property gradients are significant. This is achieved using adaptive mesh refinement (AMR). In this study, AMR is employed in passive data, species data, temperature field, and velocity field. The embedding is controlled using the equation provided below.

$$dx\_embed = \frac{dx_{base}}{2^{embed\_scale}} \tag{3.1}$$

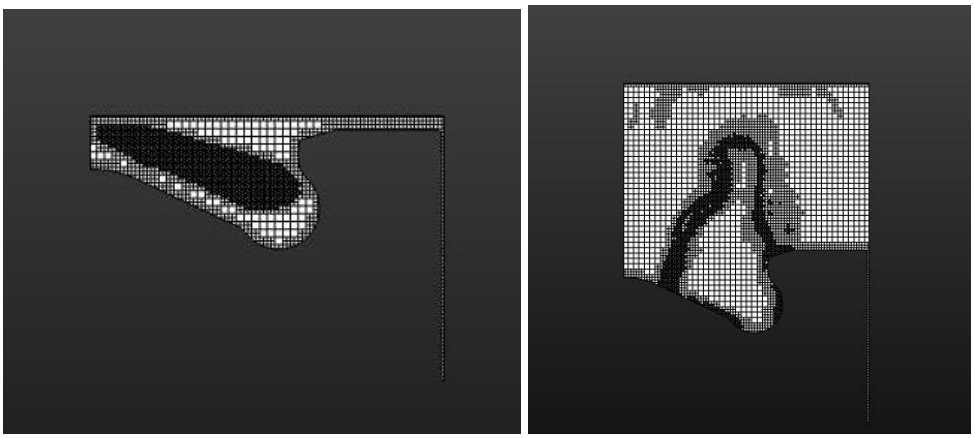

Figure 3.1 Grid embedding at spray penetration and automatic grid refinement around fuel droplets

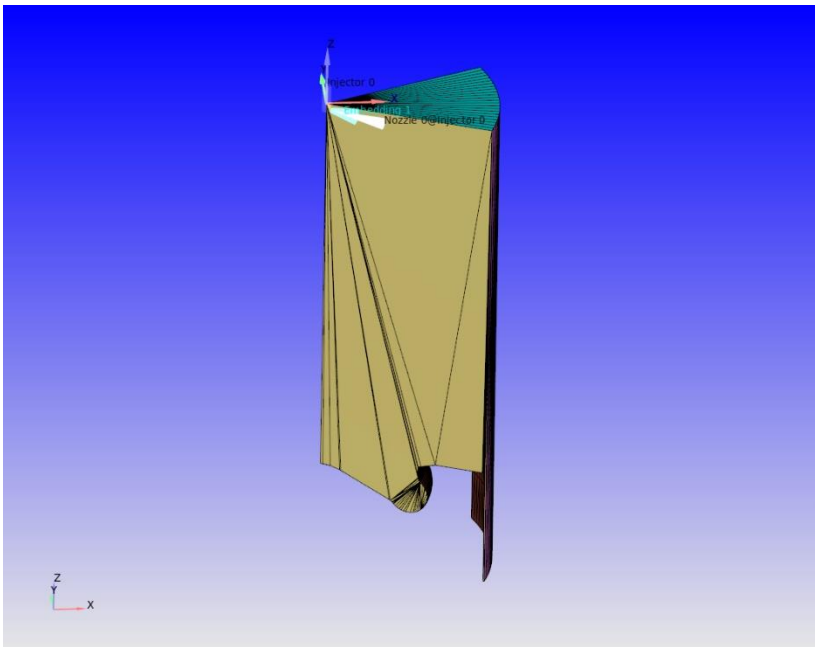

Figure 3.2 Sector geometry for the SCRE at bottom dead center with injector nozzle

3.1.2 Extract Profile Utility

This tool helps to generate piston bowl or cylinder head profiles from almost any geometry file. By using the *make_surface* utility tool, complete or sector meshes can be created and subsequently used for simulations.

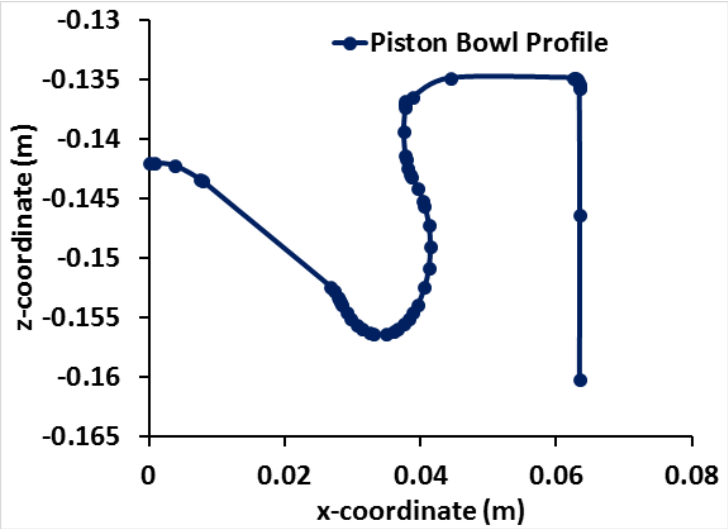

Figure 3.3 SCRE piston bowl profile.

3.1.3 Governing Equations

Parameters related to the governing equations in Converge are included in "input.in," "species.in," and "solver.in" input files. The equations for conservation of mass, momentum, and energy, turbulence and the transport of passive scalars and species are solved to resolve the reactive flow dynamics.

3.1.3.1 Mass and Momentum Transport

The mass and momentum equations are solved together for proper calculation of the pressure gradient in the momentum equation.

The compressible form of the mass conservation equation is:

$$\frac{\partial \rho}{\partial t} + \frac{\partial u_i}{\partial x} = \mathcal{S} \tag{3.2}$$

The compressible form of the momentum transport equation is:

$$\frac{\partial \rho u_i}{\partial t} + \frac{\partial \rho u_i u_j}{\partial x_j} = -\frac{\partial P}{\partial x_i} + \frac{\partial \sigma_{ij}}{\partial x_j} + \mathcal{S}_i \tag{3.3}$$

where the viscous tensor (σ_{ij}) is defined as:

$$\sigma_{ij} = \mu\left(\frac{\partial u_i}{\partial x_j} + \frac{\partial u_j}{\partial x_i}\right) + (\mu' - \frac{2}{3}\mu)(\frac{\partial u_k}{\partial x_k}\delta_{ij}) \tag{3.4}$$

When the turbulence model is activated, the viscosity (μ) is represented by the turbulent viscosity (μ_t):

$$\mu_t = \mu + C_\mu \rho \frac{k^2}{\varepsilon} \tag{3.5}$$

where u is the velocity, ρ is the density, $\mathcal{S}$ is the source term (may be due to evaporation, gravitational acceleration or other sources), P is the pressure, μ is the viscosity, μ' is the dilatational viscosity (assigned a value of zero), δ_{ij} is the Kronecker delta, C_μ is a constant in the turbulence model, k is the turbulent kinetic energy and ε is the turbulent dissipation.

3.1.3.2 Equation of State

To couple density, pressure and temperature for compressible flows, the equation of state is needed. The ideal gas. Redlich -Kwong (RK), Redlich-Kwong-Soave (RKS), and Peng-Robinson (PR) equations of state are some of the options available in Converge.

The well know ideal gas equation of state is:

$$\frac{P}{\rho} = (\frac{R}{W})(\mathrm{T}) \tag{3.6}$$

The general form of the RK, RKS, and PR equations of state can be written as follows:

$$P = \frac{RT}{v-b} - \frac{a}{v^2+ubv+wb^2} \tag{3.7}$$

where R is the universal gas constant, W is the molecular weight, and u, w, a and b are coefficients of the RK, RKS and PR equations of state.

3.1.3.3 Energy Transport

The energy conservation equation for compressible flows can be written as follows:

$$\frac{\partial \rho e}{\partial t} + \frac{\partial u_i \rho e}{\partial x_j} = -P\frac{\partial u_j}{\partial x_j} + \sigma_{ij}\frac{\partial u_i}{\partial x_j} + \frac{\partial}{\partial x_j}\left(K\frac{\partial T}{\partial x_j}\right) + \frac{\partial}{\partial x_j}\left(\sum_m h_m \frac{\partial Y_m}{\partial x_j}\right) + \mathcal{S} \tag{3.8}$$

where ρ is the density, e is the specific internal energy, K is the thermal conductivity,Y_m is the mass fraction of species m, T is the local temperature, D is the mass diffusion coefficient, P is the pressure, σ_{ij} is the stress tensor, and h_m is the specific enthalpy. The turbulent conductivity (K_t) replaces the conductivity when the turbulent model is activated.

$$K_t = K + C_p\frac{\mu_t}{pr_t} \tag{3.9}$$

where, μ_t is the turbulent viscosity and pr_t is the turbulent Prandtl number.

3.1.3.4 Species Transport

The compressible form of the species transport equation is:

$$\frac{\partial \rho_m}{\partial t} + \frac{\partial \rho_m u_j}{\partial x_j} = \frac{\partial}{\partial x_j}\left(\rho D\frac{\partial y_m}{\partial x_j}\right) + \mathcal{S}_m \tag{3.10}$$

$$\rho_m = Y_m \rho \tag{3.11}$$

$$D = \frac{v}{Sc} \tag{3.12}$$

$$D_t = \frac{v_t}{Sc_t} \tag{3.13}$$

where, Equation 3.13 is for turbulent case. u is the velocity, $\mathcal{S}_m$ is the source term, D is the mass diffusion coefficient, D_t is the turbulent mass diffusion coefficient, ρ is the density, ρ_m is the species density, Sc is the Schmidt number, Sc_t is the turbulent Schmidt number and Y_m is the mass fraction of species m.

3.1.3.5 Passive Transport

In Converge, the soot model is solved using passive transport; i.e., this passive transport equation does not affect the solution of the other transport equations. Passives are defined in "species.in and Converge solves the following passive transport equation.

$$\frac{\partial \rho \phi}{\partial t} + \frac{\partial \rho u_i \phi}{\partial x_i} = \frac{\partial}{\partial x_i}(\rho D \frac{\partial \phi}{\partial x_i}) + \mathcal{S} \tag{3.14}$$

$$D = \frac{v}{Sc} \tag{3.15}$$

Where u is the velocity, $\mathcal{S}$ is the source term, D is the mass diffusion coefficient, ρ is the density, Sc is the Schmidt number and ϕ is the passive scalar.

3.1.4 Numerics

The finite volume method is used to numerically solve the integral forms of the conservation equations. This method conserves transported quantities for regular or irregularly shaped cells. Converge stores all values at the center of each computational cell. Where values are required at cell surfaces, they are obtained either by simple cell averaging or to upwind the surface value.

$$\phi_{i+\frac{1}{2}} = \frac{1}{2}\phi_i + \frac{1}{2}\phi_{i+1} \tag{3.16}$$

$$\phi_{i+\frac{1}{2}} = \phi_i \tag{3.17}$$

Evenly interpolated surface values can be obtained using Equation 3.16 and upwind scheme can be obtained using Equation 3.17.

3.1.4.1 PISO Algorithm

The Pressure Implicit with Splitting of Operators (PISO) algorithm is used for pressure and velocity coupling in Converge. It starts with a predictor step where the momentum equation is solved and the pressure is corrected and re-applied to the momentum equation. Other transport equations are solved in series after the momentum predictor and the first corrector step are completed. If second corrector is applied to solve pressure, momentum is updated with new pressure value and other transport equations are re-solved with the second corrector with new value. Additional details of the PISO algorithm can be found in CONVEEGE 2.3 manual [36] and Issa (1986) [38].

3.1.4.2 Rhie-Chow Algorithm

Pressure and velocity decoupling occur as Converge stores all transport quantities at the center of each cell. Solution of pressure and velocity occur in checker-board pattern due to decoupling. To eliminate checker-boarding, the Rhie-Chow scheme is used in Converge to eliminate it maintaining colocated variable. Additional details can be found in the CONVERGE manual 2.3 [36].

3.1.4.3 Time Step Control

The selection of appropriate Courant-Friedrichs-Lewy (CFL) numbers is very important to obtain accurate and computationally inexpensive results. For a given time

step, the CFL number determines the number of cell solutions that will move forward. Given below are mathematical representations of the speed of sound CFL number, the convective CFL number, and the diffusive CFL number.

$$clf_{mach} = c\frac{\Delta t}{\Delta x} \tag{3.18}$$

$$clf_{u} = u\frac{\Delta t}{\Delta x} \tag{3.19}$$

$$clf_{v} = c\frac{\Delta t}{\Delta x^2} \tag{3.20}$$

where, c is the speed of sound, u is the cell velocity, ν is the viscosity, Δt is the time-step and Δx is the grid spacing. Either a fixed time step can be specified or a variable time step can be calculated internally by Converge. If, after a specified number of iterations, the solution does not converge with the variable time step option, then the time step is reduced [36]. The user can specify the maximum number of iterations for each governing equation and the maximum CFL number, which limits the time step. There are also time step restrictions for sub-models. For example, the time step for spray evolution in the spray sub-model is calculated using the following equation:

$$dt_{spray} = \min\left[\frac{\Delta x}{\text{parcel}_{\text{velocity}}}\right] * mult\_dt\_spray, \tag{3.21}$$

When *mult_dt_spray*=1, the spray parcel in one-time step cannot travel more than one cell. Similarly, the combustion time step is controlled by the combustion time scale calculated using the following equation:

$$dt\_chem = dt\_prev * min\left[\frac{\mathrm{T}}{\Delta T}\right] * mult\_dt\_chem \tag{3.22}$$

where mult_dt_chem is a parameter that controls the maximum change in temperature permitted in one-time step, T is the temperature, ΔT is the change in temperature.

3.2 Turbulence Model

The specific turbulence model plays an integral part in the prediction of dual fuel combustion. Mixing of species, momentum, and energy are greatly affected by turbulence. For this work, the so-called Renormalization Group (RNG) k-ε turbulence model is used. It is a two–equation Reynolds-Averaged Navier Stokes (RANS) turbulence model that is extensively used in scenarios where it is critical to obtain spatially resolved results without too much computational expense. In this model, the actual velocity is decomposed into two velocity components: the ensemble averaged velocity and the fluctuating velocity as given below

$$u_i = \bar{u}_i + u_i' \tag{3.23}$$

where u_i is the instantaneous velocity, $\bar{u}_i$ is the ensemble averaged velocity component and u'_i is the fluctuating velocity component. Then the compressible forms of the mass and momentum conservation equations become:

$$\frac{\partial \bar{\rho}}{\partial t} + \frac{\partial \bar{\rho}\tilde{u}_j}{\partial x_j} = 0 \tag{3.24}$$

$$\frac{\partial \bar{\rho}\tilde{u}_i}{\partial x} + \frac{\partial \bar{\rho}\tilde{u}_i\tilde{u}_j}{\partial x_j} = -\frac{\partial \bar{P}}{\partial x_i} + \frac{\partial}{\partial x_j}\left[\mu\left(\frac{\partial \tilde{u}_i}{\partial x_j} + \frac{\partial \tilde{u}_j}{\partial x_i}\right) - \frac{2}{3}\frac{\partial \tilde{u}_k}{\partial x_k}\delta_{ij}\right] + \frac{\partial(-\bar{\rho}\widetilde{u_i'u_j'})}{\partial x_j} \tag{3.25}$$

where the so-called Favre average is defined for velocity as

$$\tilde{u}_i \equiv \frac{\overline{\rho u}_i}{\bar{\rho}} \tag{3.26}$$

Reynolds stresses that represent the effects of turbulence is given as

$$t_{ij} = -\bar{\rho}\widetilde{u_i' u_j'}) \tag{3.27}$$

3.2.1 k-ε turbulence models

In the present work, the RNG k-ε model is chosen over the standard k-ε model. Turbulent normal stress values are maintained positive in the RNG k-ε model while they can have negative values in the standard k-ε model. For the RNG k-ε model, the Reynolds stress is given by

$$t_{ij} = -\bar{\rho}\widetilde{u_i' u_j'} = 2\mu_t S_{ij} - \frac{2}{3}\delta_{ij}(\rho k + \mu_t \frac{\partial \tilde{u}_i}{\partial x_j}) \tag{3.28}$$

The turbulent kinetic energy, k, is defined as

$$k = \frac{2}{3}\widetilde{u_i' u_i'} \tag{3.29}$$

The turbulent viscosity, μ_t, is defined as

$$\mu_t = C_\mu \rho \frac{k^2}{\varepsilon} \tag{3.30}$$

where, ε is the dissipation of turbulent kinetic energy and C_μ is a model constant, which may be different for different flow fields.

The mean stress tensor, S_{ij}, is defined as

$$S_{ij} = \frac{1}{2}\left(\frac{\partial \tilde{u}_i}{\partial x_j} + \frac{\partial \tilde{u}_j}{\partial x_i}\right) \tag{3.31}$$

The turbulent conductivity and turbulent diffusion terms that account for energy transport and mass transport, respectively, are given by the following equations:

$$K_t = \frac{1}{Pr_t}\mu_t \mu c_p \tag{3.32}$$

$$D_t = \frac{1}{Sc_t}\mu_t \tag{3.33}$$

where, K_t is the turbulent conductivity, D_t is the turbulent diffusion, Pr_t is the turbulent Prandtl number (fixed at 0.9 for all simulations) and Sc_t is the turbulent Schmidt number (assigned a value of 0.53).

The transport equations for turbulent kinetic energy(k) and dissipation of turbulent kinetic energy(ε) are written as follows:

$$\frac{\partial \rho k}{\partial t} + \frac{\partial \rho u_i k}{\partial x_i} = \tau_{ij}\frac{\partial u_i}{\partial x_j} + \frac{\partial}{\partial x_j}\frac{\mu}{Pr_k}\frac{\partial k}{\partial x_j} - \rho\varepsilon + \frac{c_s}{1.5}S_s \tag{3.34}$$

$$\frac{\partial \rho \varepsilon}{\partial t} + \frac{\partial \rho u_i \varepsilon}{\partial x_i} = \frac{\partial}{\partial x_j}\left(\frac{\mu}{Pr_\varepsilon}\frac{\partial \varepsilon}{\partial x_j}\right) + \rho\varepsilon c_{\varepsilon 3}\frac{\partial u_i}{\partial x_i} + \left(c_{\varepsilon 1}\frac{\partial u_i}{\partial x_j}\tau_{ij} - c_{\varepsilon 1}\rho\varepsilon + c_s S_s\right)\frac{\varepsilon}{k} + S - \rho R \tag{3.35}$$

where, S_s is source term from interaction with the diesel spray and S is the user specified source term. Compression and expansion are accounted for by $c_{\varepsilon 1}$, $c_{\varepsilon 2}$ and $c_{\varepsilon 3}$ are model constants. The variable R is given by

$$R = \frac{C_\mu \eta^3 (1-\eta/\eta_0)}{(1+\beta\eta^3)} - \frac{\varepsilon^2}{k} \tag{3.36}$$

where

$$\eta = \frac{k}{\varepsilon}|S_{ij}| = \frac{k}{\varepsilon}\sqrt{2S_{ij}S_{ij}} \tag{3.37}$$

3.3 Spray Model

After injection, the diesel fuel spray undergoes several processes (such as breakup, collision, and coalescence) until evaporation. A summary of the main fuel spray processes as represented in the spray model is discussed here. A group of identical drops with the same radius, temperature, velocity and so on are represented as a parcel. A Lagrangian approach is used to solve the dynamics of these parcels from injection until

vaporization. For this study DIESEL2 from the CONVERGE library is chosen as the single-component liquid species for all simulations performed in this thesis. Viscosity, surface tension, heat of vaporization, vapor pressure, conductivity, density, and specific heat as a function of critical temperature are provided for DIESEL2. The blob injection approach is considered for modeling spray evolution. In this approach, the size of injected drop is set to the effective nozzle hole diameter of the injector [39]. For sector mesh simulations, the diesel quantity for the defined sector is calculated and given as injected mass quantity. Injection velocity for each time interval is specified in the injection rate shape (profile) for a specified injection duration. It must be noted that only the rate profile is important but not the magnitude. Because CONVERGE scales the rate profile to ensure that the specified fuel mass is injected over the specified injection duration. Flow contraction may occur while fuel flows through the nozzle hole. This is considered by introducing a contraction coefficient.

$$C_a = \frac{C_d}{C_v} \tag{3.38}$$

where, C_a is the contraction coefficient, C_d is the discharge coefficient and C_v is the velocity coefficient. The magnitude of drop velocities increases when the effective area of the nozzle decreases. A dynamic drag model is used for all simulations performed in this work. In this model, the drop shape varies per a distortion parameter, *y*. The Taylor Analogy Breakup (TAB) model is used to determine this distortion parameter. Details of the TAB model can be found in O'Rourke and Amsden, 1987 [40]. Prediction of the correct drop shape is very critical to evaluate proper drag. As is well known, the drag on a spherically shaped drop will be less than disk-shaped drop. The drag coefficient is given by

$$C_D = C_{D,sphere}(1 + 2.632y) \tag{3.39}$$

where, y is drop distortion from the TAB model and is given as

$$y(t) = We_c + e^{-\frac{t}{t_d}}[(y(0) - We_c)\cos(\omega t) + \frac{1}{\omega}\left(\frac{dy}{dt}(0) + \frac{y(0) - We_c}{t_d}\right)\sin(\omega t)] \tag{3.40}$$

where

$$We_c = \frac{C_f}{C_k C_b} We_g \tag{3.41}$$

$$We_c = \frac{\rho_g u^2 r_0}{\sigma} \tag{3.42}$$

$$\frac{1}{t_d} = \frac{C_d}{2}\frac{\mu_l}{\rho_l r_0^2} \tag{3.43}$$

$$\omega^2 = C_k \frac{\sigma}{\rho_l r_0^3} - \frac{1}{t_d} \tag{3.44}$$

ω is the droplet oscillation, C_k, C_f, C_d, and C_b are constants, σ is liquid surface tension, ρ_l is the liquid phase density, We_g is the droplet Weber number. A modified Kelvin-Helmholtz and Rayleigh-Taylor (KH-RT) droplet breakup model is used to model spray breakup. In the KH-RT model, the primary breakup of the intact liquid core is predicted by the KH instability model. Both KH and RT instabilities are utilized to predict secondary breakup of each droplet. The RT break-up model only affect drops beyond the break-up length. In the modified KH-RT model, the RT breakup model affects all drops outside the intact liquid core of the jet. Additional details of the KH-RT model for spray breakup model can be found in the CONVERGE manual, Reitz, 1987 [41] and Beale et al 1999 [42]. CONVERGE considers parcels for collision, which drastically reduce computational cost. The no time counter (NTC) collision model of Schmidt and Rutland [43] is used for all simulations performed in this thesis. In the NTC

model, the outcome of droplet collision can be grazing collision or coalescence. In case of grazing collision, the temperature and size of the droplet are conserved and the velocity changes. In case of coalescence, the size, temperature and velocity of the droplet are updated and removed from the original parcel. Due to grid dependency of the droplet collision process, an adaptive collision mesh is made available in CONVERGE. Collision mesh is not used in the present work. Proper care should also be taken to account for drop-wall interactions. This directly affects the total mass of combustible fuel available in the combustion chamber with an opportunity to participate in the ensuing combustion process. The rebound/slide model is used for spray wall interaction, details of which can be found in Naber and Reitz, 1988 [44].

3.4 Chemistry and Emission Model

To solve for the chemical kinetics of the combustion process, the SAGE model [45] is activated for both pure diesel and diesel-methane dual fuel combustion. The SAGE model inputs are in CHEMKIN format. The transport equation is solved by the CFD solver, while SAGE calculates the reaction rates of all species. Multi-step reactions, following Turns (1996) [35], can be written as follows:

$$\sum_i^i v'_{ij} X_i \Leftrightarrow \sum_i^i v''_{ij} X_i \text{ for j=1, 2,…..J} \quad (3.45)$$

where, v'_{ij} and v''_{ij} are the stochiometric coefficients for reactants and products, i.e., for species i participating in reaction j; J is the total number of reactions. The chemical symbol for species i is represented by X_i. The net production rate of species i is

$$\dot{\omega}_i = \sum_{j=1}^{J} (v''_{ij} - v'_{ij}) q_j \quad \text{for i=1,2,….I} \quad (3.46)$$

where, I is the total number of species. The rate of progress of the j^{th} reaction is given by q_j

$$q_j = k_{fj} \prod_{i=1}^{I} [X_i]^{v'_{ij}} - k_{rj} \prod_{i=1}^{I} [X_i]^{v''_{ij}} \tag{3.47}$$

where, $[X_i]$ is the mole fraction of species I, the forward and reverse reaction coefficients of reaction j are k_{fj} and k_{rj}, respectively. The forward and reverse reaction coefficients are evaluated as

$$k_{fj} = A_j T^{bj} e^{E_j/TR_u} \tag{3.48}$$

$$k_{rj} = \frac{k_{fj}}{k_{cj}} \tag{3.49}$$

where, k_{cj} is the concentration-based chemical equilibrium constant for reaction j, which is given by:

$$k_{cj} = k_{pj} \left(\frac{P_{atm}}{RT}\right)^{\sum_{i=1}^{I} v_{ij}} \tag{3.50}$$

where, A_j is the pre-exponential factor, R_u is universal gas constant, R is the gas constant, b_j is the temperature exponent, T is the temperature, E_j is the activation energy and P_{atm} is the atmospheric temperature. K_{pj} is partial pressure-based equilibrium constant given as

$$k_{pj} = exp\left(\frac{\Delta S_j^0}{R} - \frac{\Delta H_j^0}{RT}\right) \tag{3.51}$$

where, Δ is the change that occurs in passing completely from reactants to products in the j^{th} reaction The changes in entropy (S) and enthalpy (H) of the reaction are obtained from the following equations:

$$\frac{\Delta S_j^0}{R} = \sum_{i=1}^{I} v_{ir} \frac{S_i^0}{R} \tag{3.52}$$

$$\frac{\Delta H_j^0}{RT} = \sum_{i=1}^{I} \nu_{ir} \frac{H_i^0}{RT} \tag{3.53}$$

For a given computational cell with the chemical kinetic equations discussed above, the mass and energy conservation equations can be solved as follows:

$$\frac{d[X_i]}{dt} = \dot{\omega}_\iota \tag{3.54}$$

and

$$\frac{dT}{dt} = \frac{V\frac{dp}{dt} - \sum_i \bar{h}_i \dot{\omega}_\iota}{\sum_i [X_i] \bar{c}_{p,i}} \tag{3.55}$$

where, $\bar{h}_i$ is the molar specific enthalpy and $\bar{c}_{p,i}$ is the molar constant pressure specific heat of species i. At each time step, the species concentrations are updated using the equation provided above. Chemical kinetics are solved in a given computational cell only above a certain temperature and minimum mole fraction of CO, H_2 and the hydrocarbon species. Also, multi-zone modeling is utilized to solve combustion calculations, which also expedites the chemical kinetics calculation. For single fuel combustion, SAGE utilizes a two-dimensional zoning strategy. In the two-dimensional zoning algorithm, cells are grouped based on similar temperature and equivalence ratio. For dual fuel combustion, a three-dimensional zoning strategy is utilized. In the three-dimensional zoning strategy, similar temperature, equivalence ratio, and diesel mass fraction are considered for grouping cells. For two cells to be grouped in the same zone, the cube root of the diesel mass fraction in both cells should be less than $Y_i^{1/3}$ along with meeting other criteria for temperature and pressure. Additional details about the multi-zone modeling approach can be found in the CONVERGE manual [36].

3.4.1 Emission models

The Hiroyasu model of soot formation and Nagle-Strickland-Constable (NSC) model for soot oxidation are activated for soot prediction. The production of soot mass in a cell can be computed by considering the rate of soot mass formation minus the rate of soot mass oxidation as follows:

$$\frac{dM_s}{dt} = \frac{dM_{sf}}{dt} - \frac{dM_{so}}{dt} \tag{3.56}$$

where,

$$\frac{dM_{sf}}{dt} = A_{sf} P^{0.5} \exp\left(-\frac{E_{sf}}{R_u T}\right) M_{form} \tag{3.57}$$

where, P is the cell pressure, T is the cell temperature, R_u is the universal gas constant, E_{sf} is the activation energy for soot formation, A_{sf} is the Arrhenius pre-exponential factor and M_{form} is mass of soot formation species. Additional details can be found in Nagle and Strickland-Constable

(1962) (NSC) [35] and Hiroyasu and Kadota (1976) [37].

The extended Zel'dovich mechanism [10] is employed to calculate NO formation. More details about the model can be found in the CONVERGE manual. In the extended Zel'dovich model, the following set of reactions are used to calculate NO formation:

$$O + N_2 \leftrightharpoons NO + N \tag{3.58}$$

$$N + O_2 \leftrightharpoons NO + O \tag{3.59}$$

$$N + OH \leftrightharpoons NO + H \tag{3.60}$$

Assuming steady state for N-atoms, the NO formation can be written as:

$$\frac{d[NO]}{dt} = 2k[O][N2] \tag{3.61}$$

where, k is the reaction rate coefficient constant and [ ] indicates the mole fraction of different species.

3.4.2 Computational Resource

The CFD simulations in the present work were performed on "Shadow," a high performance computing resource at Mississippi State University. **Shadow** is a Cray CS300-LC cluster with 4800 Intel Ivy Bridge processor cores and 28,800 Intel Xeon Phi cores. The system has a total 70 TB of RAM, with each node having either 512 GB of RAM (45%), 128 GB of RAM (45%) or 64 GB of RAM (10%). Shadow can perform 593 teraFLOPS (trillion floating point operations per second) at its peak performance.

3.5 Initial Condition

3.5.1 Initial Mass Fraction

The initial mass fractions of methane, oxygen, nitrogen, carbon dioxide and water are given by:

$$MF_{ch4} = \frac{M_f}{S_s} \tag{3.62}$$

$$MF_{o2} = \frac{M_{o2}}{S_s} \tag{3.63}$$

$$MF_{n2} = \frac{M_{n2}}{S_s} \tag{3.64}$$

$$MF_{co2} = \frac{M_{co2}}{S_s} \tag{3.65}$$

$$MF_{h20} = \frac{M_{h2o}}{S_s} \tag{3.66}$$

Where MF_f is the mass flow rate of methane into cylinder, MF_{o2} is the mass flow rate of oxygen into the cylinder, MF_{n2} is mass flow rate of nitrogen into cylinder, MF_{co2}

is mass flow rate of carbon dioxide into cylinder, MF_{h20} is the mass flow rate of water vapor into the cylinder and S_s is the total mass flow rate of all species into the cylinder.

3.5.2 Initial Turbulence

The initial turbulence kinetic energy is given by

$$k = \frac{3}{2} V_f{}^2 \tag{3.67}$$

where, V_f is the velocity fluctuation given by

$$V_f = C_4 \frac{2 S_c N}{60} \tag{3.68}$$

Where S_c is stroke of cylinder, N is engine speed and C_4 is constant.

The initial turbulence dissipation rate is given as

$$\varepsilon = \frac{(0.09)^{\frac{3}{4}} k^{\frac{3}{2}}}{0.025(B)} \tag{3.69}$$

where, B is the cylinder bore.

3.6 Boundary Condition

The wall boundary conditions for cylinder wall and cylinder head were opted to be fixed and moving for piston. Periodic boundary conditions were opted for the sides of the sector mesh. All boundaries (except the sides of the sector mesh) uses the so-called "law of the wall" boundary condition for temperature and velocity. The piston, cylinder liner, and cylinder head boundaries use Neumann conditions for species, passive, turbulent kinetic energy (tke) and pressure. Dirichlet boundary condition was applied for the turbulent dissipation (eps). Smooth wall condition is assigned by specifying a wall roughness value of 0.

CHAPTER IV

RESULTS AND DISCUSSION

4.1 Engine specification and test condition

A single cylinder research engine (SCRE) is used for all experiments and computational simulations performed in this work. The specifications of the SCRE are given in Table 4.1. The nominal compression ratio provided for this engine by the engine manufacturer is 17.1:1. However, based on simulations performed to match the experimentally measured motoring (i.e., non-firing) pressures, the compression ratio was determined to be 16.2:1. Figure 4.1 shows the match between predicted and measured motoring pressure curves. The motoring data is obtained at 1500 rpm engine speed and 1.5 bar intake pressure. For the firing cases, the fuel injection rate profile is not known; therefore, it is assumed to be a "top hat" profile, which is typical of many common-rail injection systems. The actual swirl ratio of the engine is not known; however, based on the observed bowl geometry combined with the fact that the SCRE is based on a heavy-duty diesel engine, a low swirl ratio value of 0.05 is assumed. The sector mesh closed cycle simulations were performed from IVC to EVO and all experiments were performed in the Advanced Combustion Engine (ACE) laboratory at Mississippi State University. Details of the experiments performed at engine load of 3.3 bar BMEP for diesel-methane dual fuel combustion can be found in Raihan[46]. Experimental results for pure diesel

operation for loads of 2.5 bar, 3.3 bar, 5 bar and 7.5 bar BMEP (see Ref. [47]) were made available for purposes of model calibration and validation.

A schematic of the experimental setup from Ref. [47] is modified for dual fuel operation and shown in Figure 4.2.

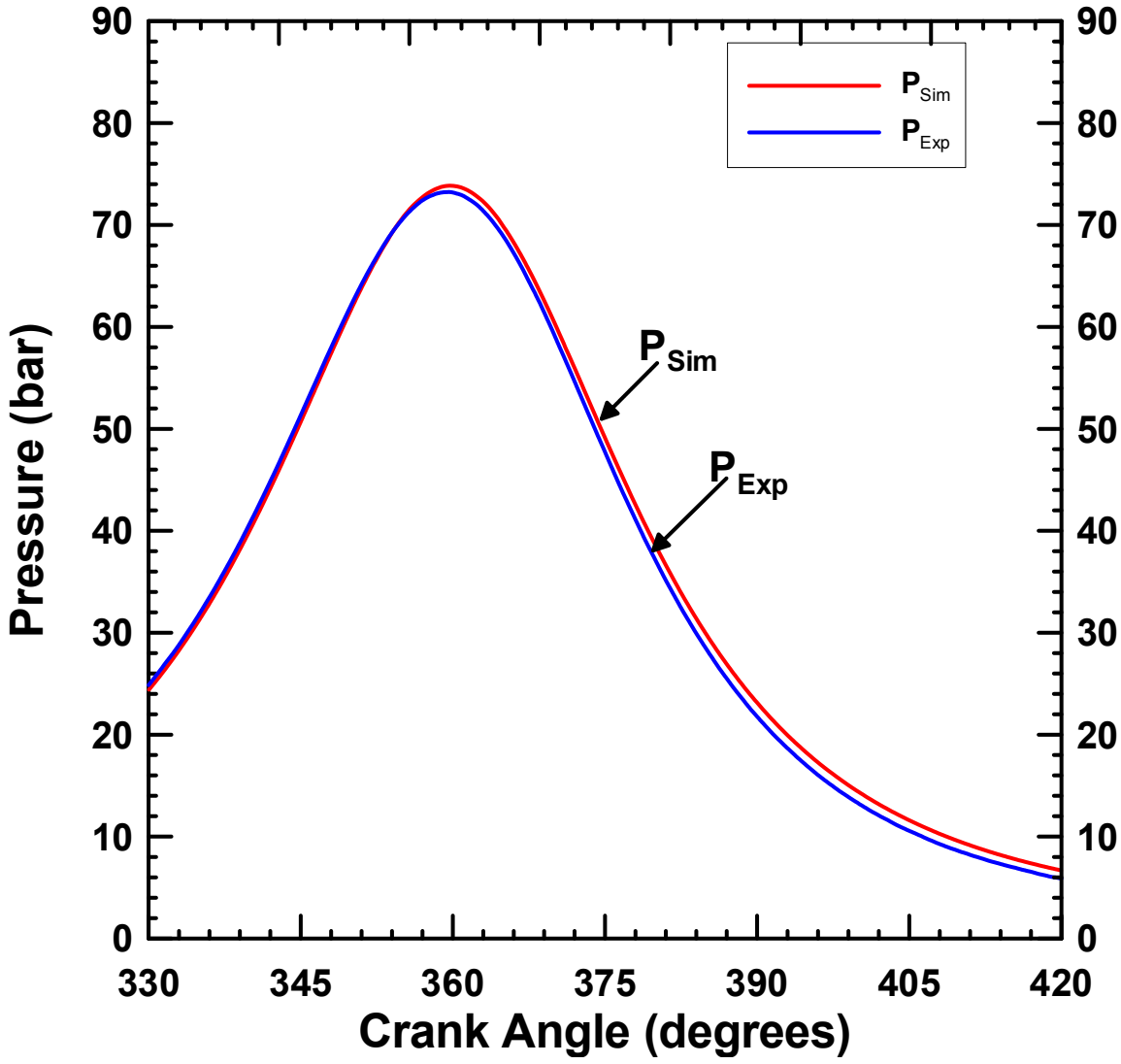

Figure 4.1 Motoring pressure curve at 1500 engine speed and 1.5 bar intake pressure

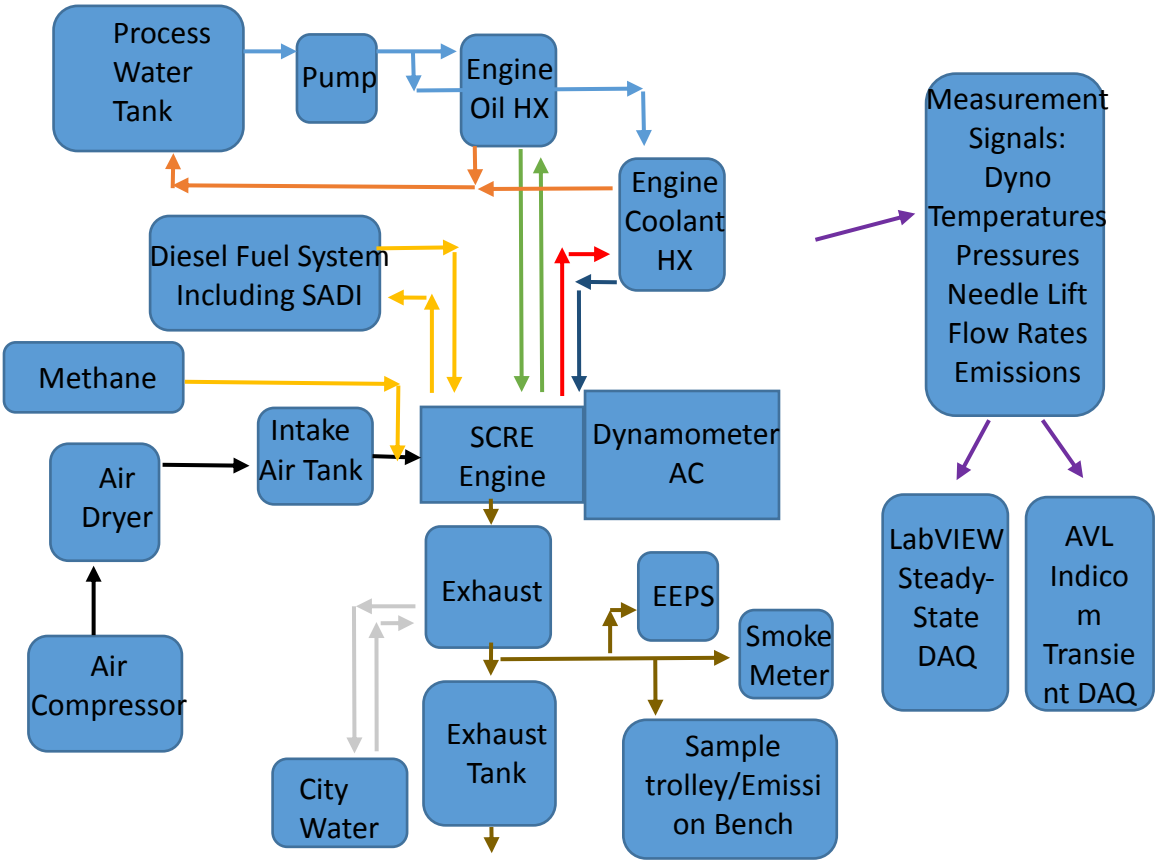

Figure 4.2 Schematic of experimental setup

The SCRE is coupled to a 250 HP AC regenerative dynamometer. Speed and load on the engine are controlled using a Dyne Systems Inter-Loc V controller. Exhaust samples are passed through an EGAS2M emissions bench for the measurement of NO, NOx, HC, CO, CO_2, and O_2. The emissions bench measures NO and NOx using two chemiluminescence detection cells and measures oxygen using a paramagnetic detector. The total hydrocarbons are measured using a heated flame ionization detector. Carbon dioxide and carbon monoxide are measured by the emissions bench using a nondispersive infrared analyzer. An AVL smoke meter (415S) is used to measure exhaust smoke

emissions in filter smoke number (FSN) units. Emerson Micro Motion coriolis mass flow meters are used to measure flow rates of diesel and methane. A DRIVVEN stand-alone diesel injection (SADI) system is utilized to control diesel injection parameters. Omega K-type thermocouples are used to measure the temperature of exhaust, oil, coolant, intake air, fuel, and ambient air. A Kistler model 6052C pressure sensor and a Kistler 5010B type charge amplifier are used to obtain in-cylinder pressure data at a resolution of 0.1 crank angle degree. The SCRE injector is instrumented with a Wolff hall effect sensor to obtain needle lift data. A Flow Maxx sonic orifice is used for air mass flow rate measurement. The data are collected using National Instruments PXI hardware and a LabVIEW-based data acquisition software.

Table 4.1 Single Cylinder Research Engine Specification

Parameter	**Value**
Bore	128 mm
Stroke	142 mm
Connecting rod	228 mm
Compression ratio used for simulations	16.2:1
Nominal swirl ratio	0.05 (assumed)
Intake valve closing (IVC)	198 CAD
Exhaust valve opening (EVO)	532 CAD
Combustion Chamber Geometry	Mexican hat
Diesel fuel injection system	Bosch CP3 common –rail
Injector nozzle hole diameter	0.197 mm
Number of nozzle holes	8
Methane fueling	Fumigation into manifold
Maximum Engine speed (rpm)	1900

4.2 Computational Setup

The piston surface was scanned using a Go!Scan 3D scanner by Creaform and a software called VXelements. The scan was postprocessed using Geomagic Design Direct software to obtain a ".prt" file. Solidworks was then used to get the piston into a ".stl" format. The piston profile was then obtained using CONVERGE Studio and a sector mesh was created using the same software. The squish height was also defined using the "make surface utility" command in CONVERGE Studio. Closed cycle simulations are performed from IVC to EVO. The minimum number of cells are as low as 9000 near top dead center in the compression stroke before diesel injection while the maximum number of cells are as high as 600000 in the expansion phase. The number of cells with respect to crank angle for 80 PES diesel-methane dual fuel combustion case is shown in Figure 4.3. The longest computational time for diesel methane dual fuel combustion was 15 hours. Pure diesel for 3.3 bar BMEP took around 7 hours to complete while the 6.5 bar BMEP case took around 12 hours to complete.

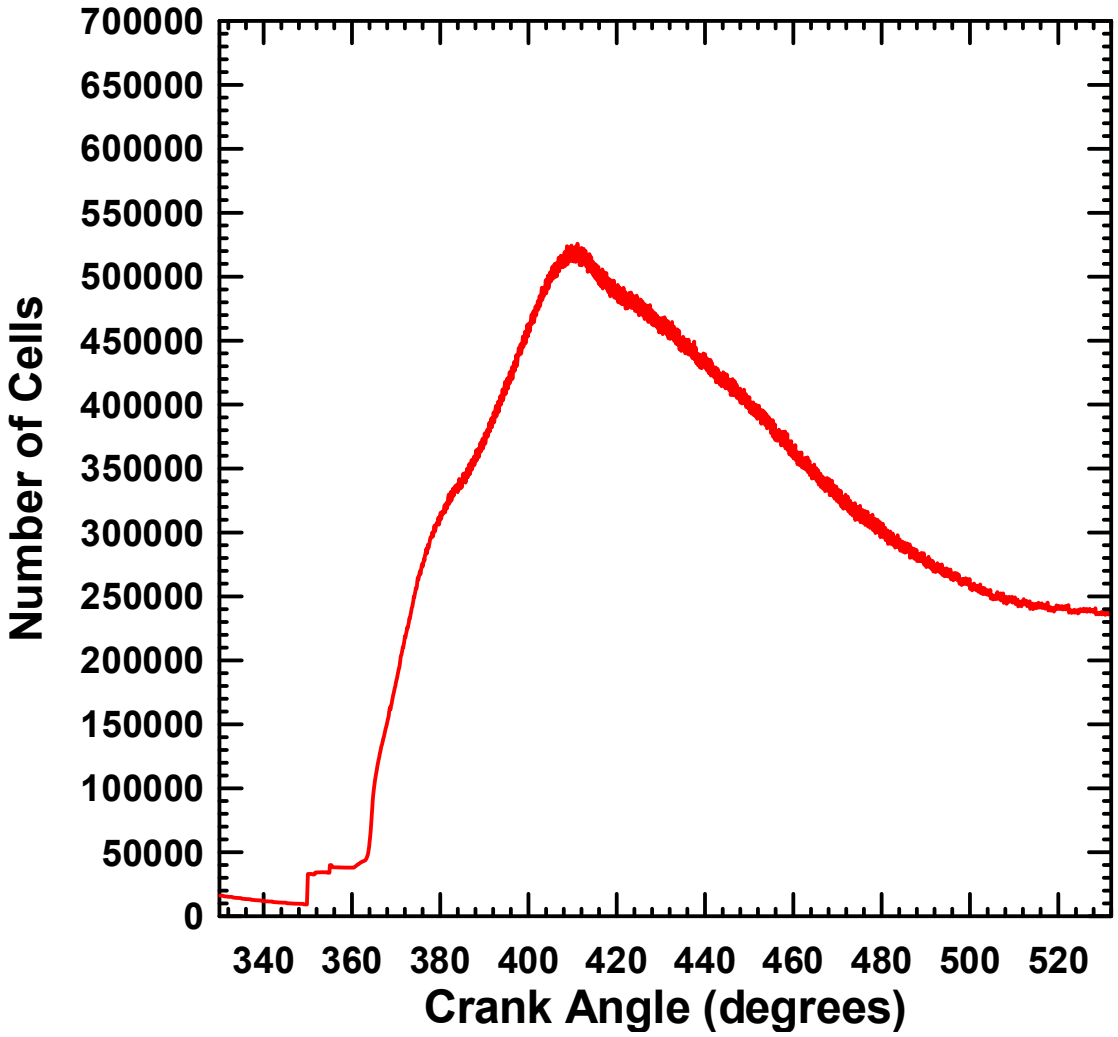

Figure 4.3 Total number of cells in a domain for 80 PES diesel-methane dual fuel (BMEP = 3.3 bar) case

4.3 Diesel combustion simulation results

Four different engine loads are simulated for diesel combustion. The initial and boundary conditions are listed in Table 4.2. The temperature and pressure at intake valve closing are determined using a Wiebe function-based combustion model in the 1D GT POWER software. The residual gas fraction is also obtained from the GT POWER simulations. A "top-hat-shaped" injection profile is assumed for all cases as

experimental injection rate profiles were not available. The delay between the actual opening of the injector and the signal given from DRIVVEN is assumed to be 4.2 CAD. The SOI used for the simulations is 362.2 CAD.

Table 4.2 Pure diesel simulation test cases

Load	PIVC (bar)	TIVC (K)	Fuel injected (kg/cycle/cyl)	Cylinder head Temp.(K)	Liner Temp. (K)	Piston Temp. (K)
2.5	1.61	363	4.1E-05	420	400	450
3.3	1.61	367	4.9E-05	430	410	470
5	1.61	371	6.6E-05	470	430	510
7.5	1.62	375	9.3E-05	490	450	530

A comparison of predicted and experimental in-cylinder pressure, apparent heat release rate (AHRR), indicated specific oxides of nitrogen (NOx), and combustion phasing (CA50) for pure diesel combustion is provided in Figures 4.4 through Figure 4.9. Figure 4.10 shows the temperature evolution with respect to crank angle degrees (CAD) for diesel combustion. The color maps are presented in a section (i.e., XZ plane) that was obtained by cutting the computational domain (viewing from the top) in the middle of the sector along the cylinder axis. The color maps of evolution of temperature, NOx, the hydroxyl radical (OH), and equivalence ratio with respect to CAD for different loads are shown from Figure 4.11 through Figure 4.25. From Figures 4.4 through 4.7, it is evident that the in-cylinder pressure traces are predicted well compared to the experimental measurements. The experimental heat release value become negative just after SOI as fuel vaporization cools in- cylinder [46]. The model is able to predict the start of ignition well for all cases and the initial portion of the AHRR is also predicted well for all cases

except for the BMEP of 7.5 bar, which shows a slight overprediction. However, the AHRR for the mixing controlled combustion period (the second phase of AHRR) is not predicted as accurately as the initial phase of the AHRR. This may be attributed (at least partially) to uncertainties in the diesel injection rate profile and initial conditions such as swirl ratio and temperature at IVC. We are more concerned about trends of combustion than the exact value as reduced mechanism is used with uncertainty in initial condition. So, to look for trends is major objective considering computational time and accuracy.

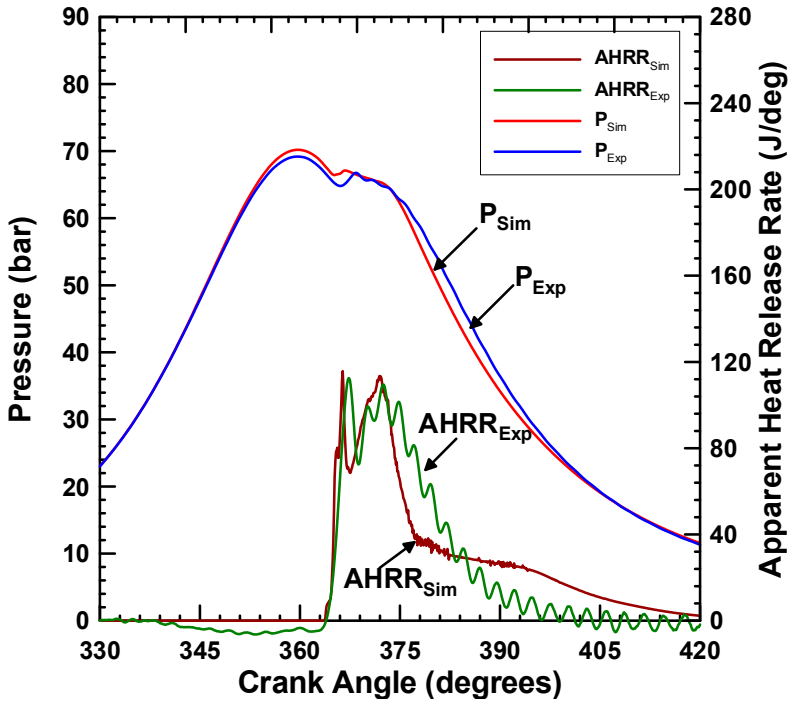

Figure 4.4 Pressure and AHRR comparisons for BMEP = 2.5 bar

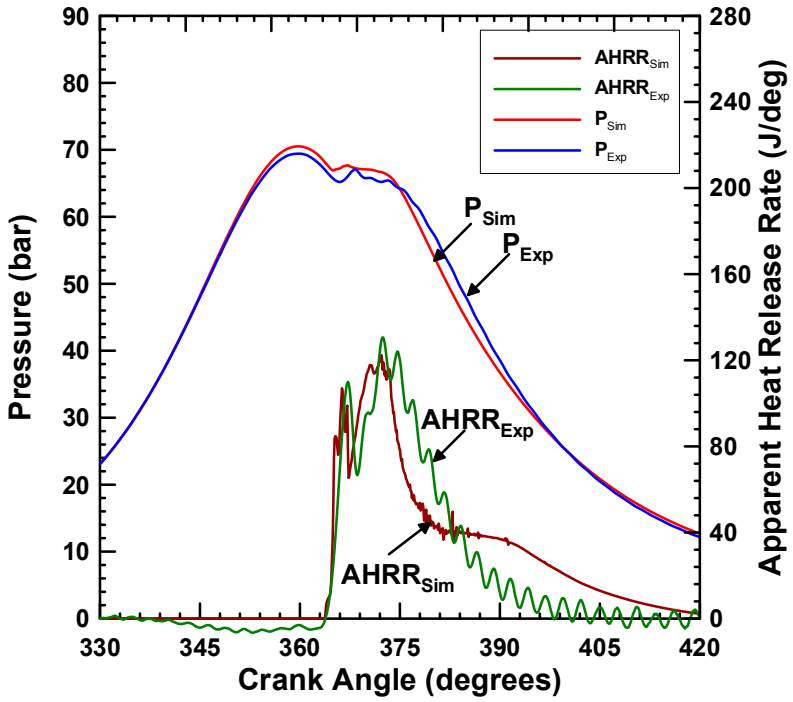

Figure 4.5 Pressure and AHRR comparisons for BMEP = 3.3 bar

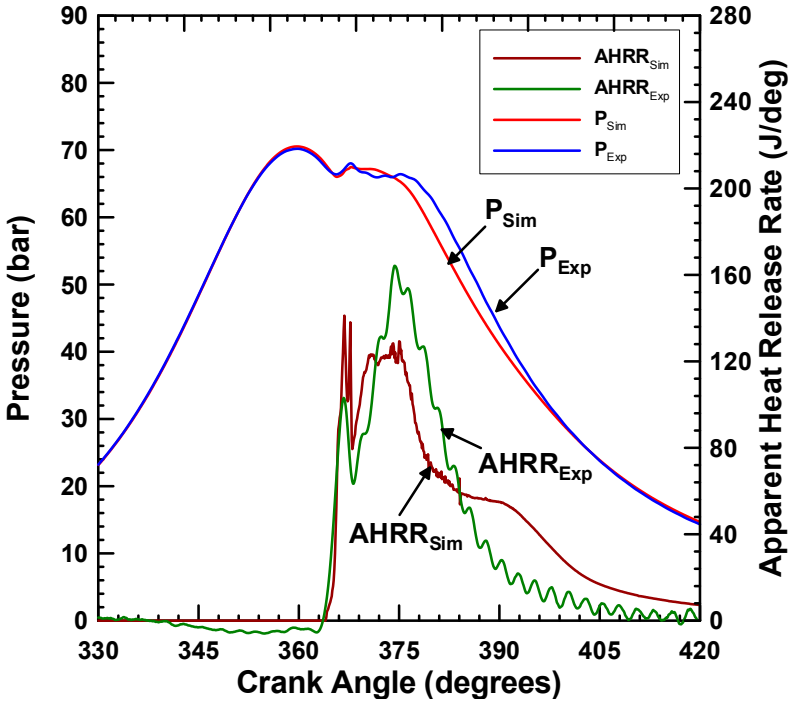

Figure 4.6 Pressure and AHRR comparisons for BMEP = 5.0 bar

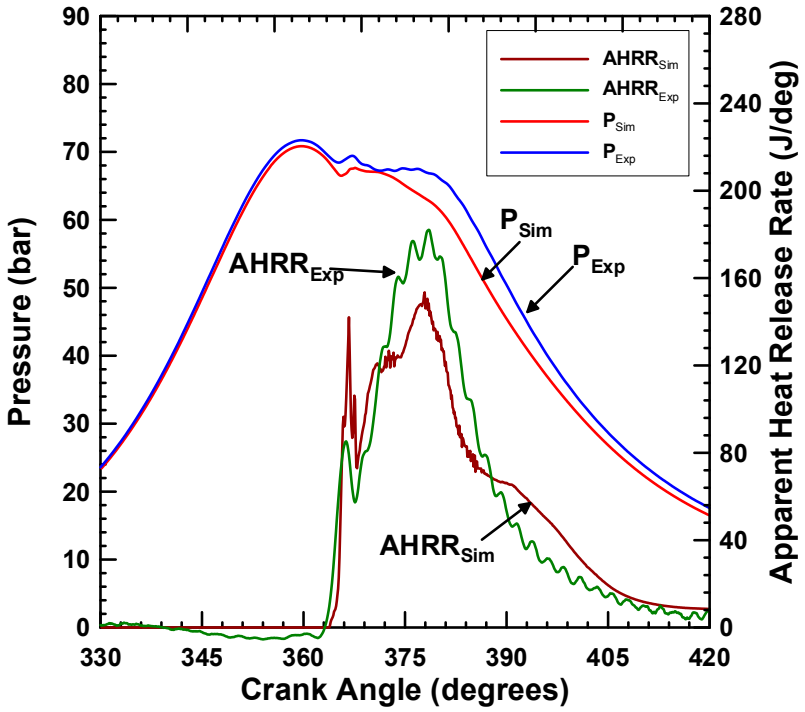

Figure 4.7 Pressure and AHRR comparisons for BMEP = 7.5 bar

The trends for combustion phasing as well as NOx are correctly predicted when compared to the experiments, although NOx and CA50 are slightly underpredicted for intermediate loads such as BMEP = 5 bar. The slight but systematic underprediction of CA50 for many loads may be attributed to uncertainties in the initial conditions as well as slight mismatches in the AHRR curves. The slight decrease in NOx at BMEP = 7.5 bar is likely due to the cooling effect of additional diesel fuel injected at the higher load since the duration of diesel injection is longer. This is confirmed by the crank angle-resolved maximum temperature plot for different BMEPs shown in Figure 4.10, which shows a slightly higher maximum temperature for 5 bar BMEP compared to 7.5 bar BMEP at 378 CAD. The mass of NOx produced for 7.5 bar BMEP is 2.23E-06 and for 5.5 bar BMEP case is 1.88E-06. It can be noted that NOx formed is slightly higher for 7.5 bar BMEP

than 5.0 bar BMEP but the indicated power is higher for 7.5 bar BMEP case which decrease ISNOx.

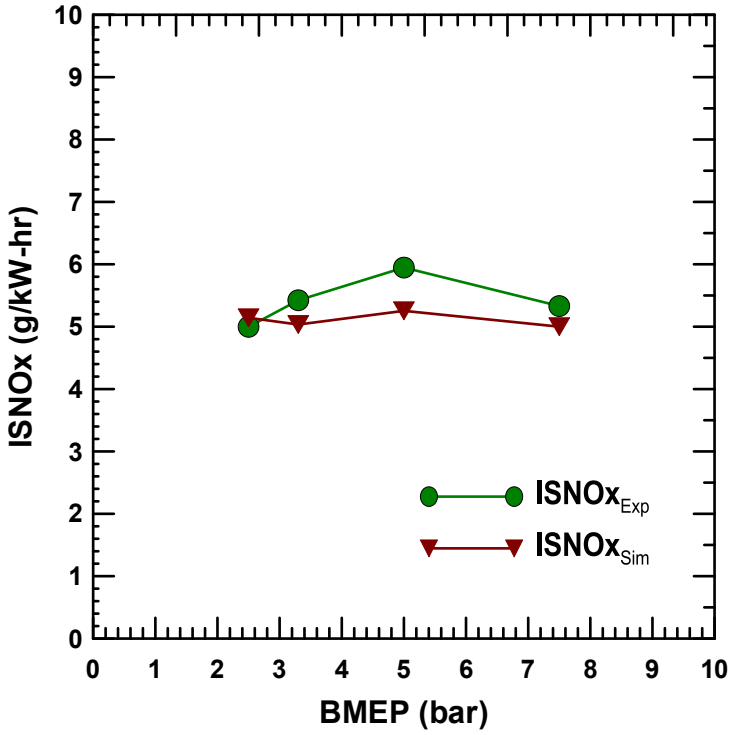

Figure 4.8 ISNOx trends for BMEPs of 2.5, 3.3, 5.0, and 7.5 bar for pure diesel combustion

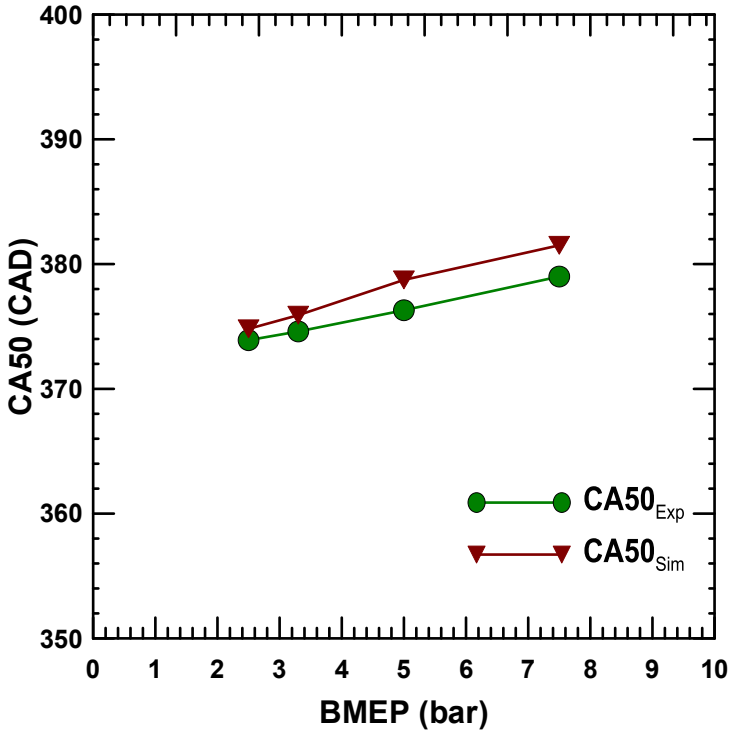

Figure 4.9 CA50 trends for BMEPs of 2.5, 3.3, 5.0, and 7.5 bar for pure diesel combustion

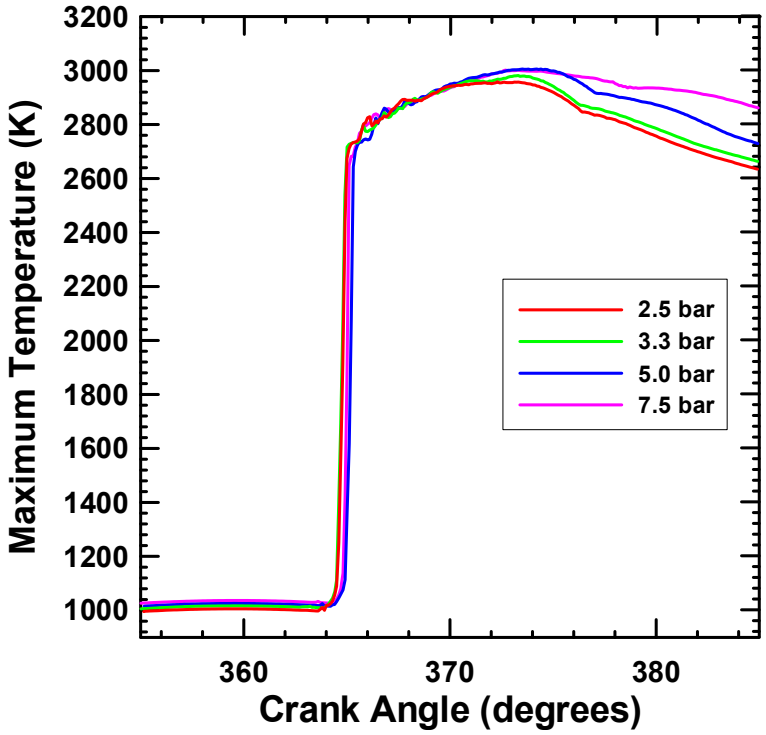

Figure 4.10 Maximum temperature plot for different BMEPs (2.5, 3.3 5.0 and 7.5 bar) for pure diesel combustion

Figure 4.11 to 4.14 show sectional color maps of the local temperature, NOx, OH, and equivalence ratio for the BMEP of 2.5 bar. It is evident from the color maps that, for all loads, NOx formation can be seen to occur near the lifted diffusion flame where combustion is near stoichiometric. This is also consistent with Dec [11], who explained in his conceptual model of diesel combustion that the highest local temperatures and NOx concentrations are present near the periphery of the diffusion flame. The simulation also predicts OH distributions (see Figure 4.13) that are consistent with Dec's conceptual model. Up to 378 CAD, the OH concentration is confined to a narrow region around the diffusion flame, where the equivalence ratio is near stoichiometric (see Figure 4.14). Since OH is both a precursor of hot autoignition and a marker for high temperature

combustion regions, the diesel combustion process starts where there is first occurrence of OH. It can be seen clearly that there is some spray impingement on the piston and rebound into the piston bowl, and to some extent, into the squish area. Due to the shorter injection duration and smaller quantity of diesel injected, the combustion process is largely concentrated in the piston bowl region.

Figures 4.15 through 4.18 show color maps of the local temperature, NOx, OH, and equivalence ratio for the BMEP of 3.3 bar. In general, the trends are similar to those observed for the 2.5 bar BMEP case. However, due to longer injection duration and more injected diesel quantity, the fuel is distributed throughout the combustion chamber. Similarly, Figures 4.19 through 4.22 show plots of local temperature, NOx, OH, and equivalence ratio for the BMEP of 5.0 bar and Figures 4.23 through 4.26 show the corresponding plots for the BMEP of 7.5 bar. For BMEP = 7.5 bar, due to higher local equivalence ratios and the higher fuel injected quantity, the fuel is distributed more widely within the combustion chamber, and consequently, the hot combustion zones are also more widely distributed.

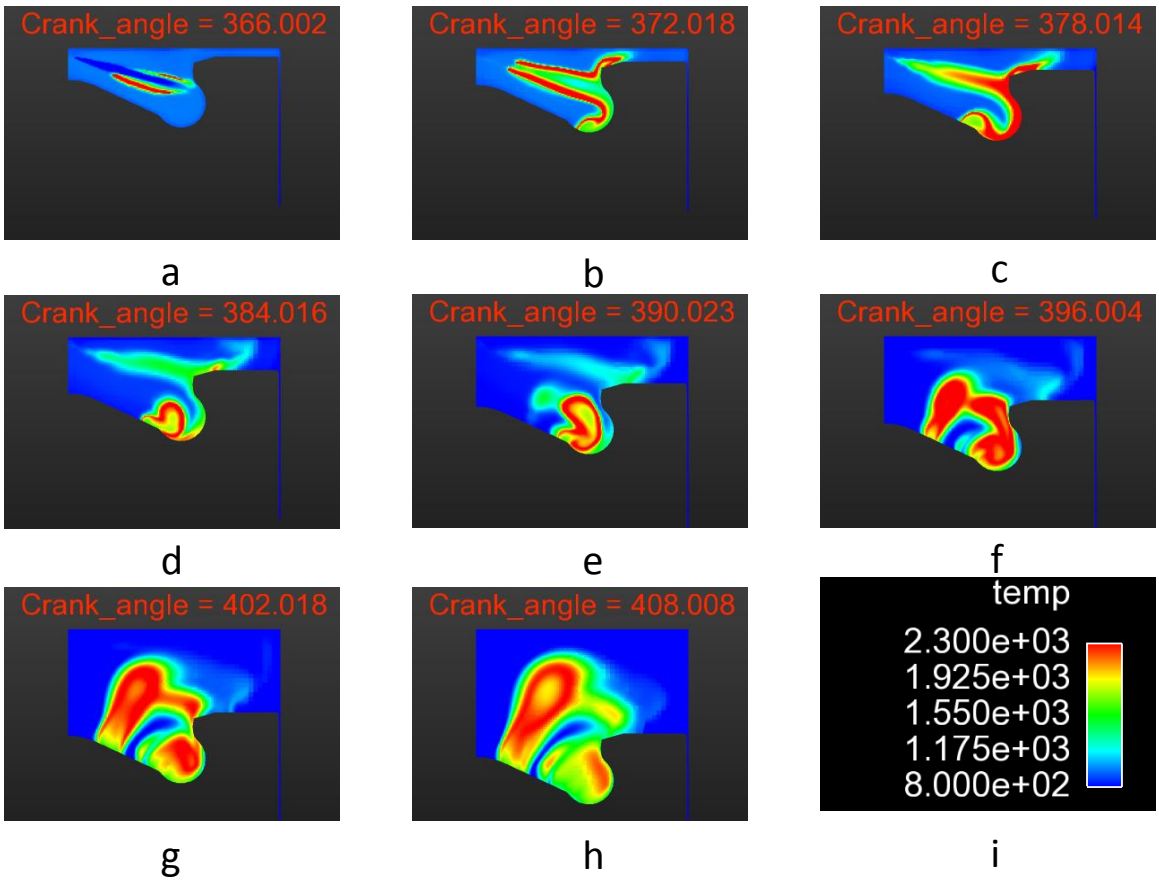

Figure 4.11 Local temperature evolution for BMEP = 2.5 bar from (a) 366 CAD to (h) 408 CAD; (i) shows the scale for temperature in Kelvin

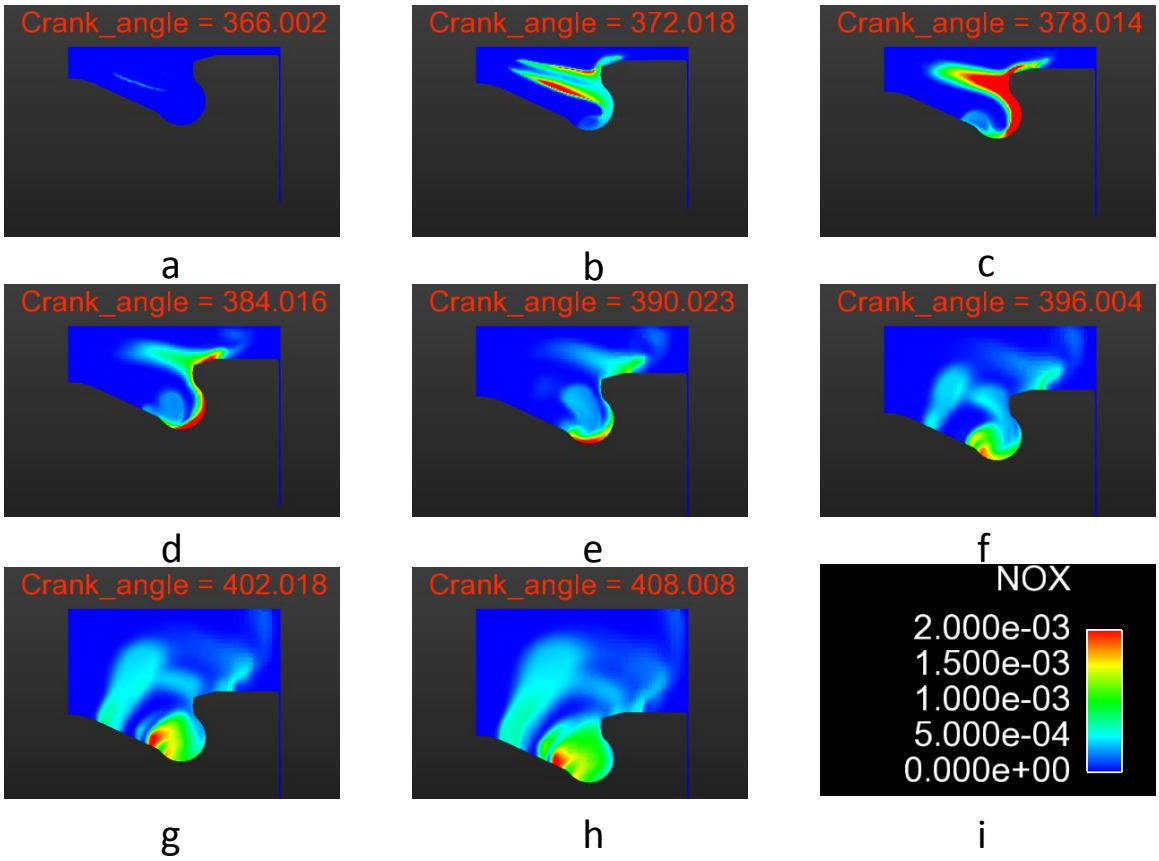

Figure 4.12 NOx evolution for BMEP=2.5 bar from (a) 366 CAD to (h) 408 CAD; (i) shows the scale for NOX in mass fraction

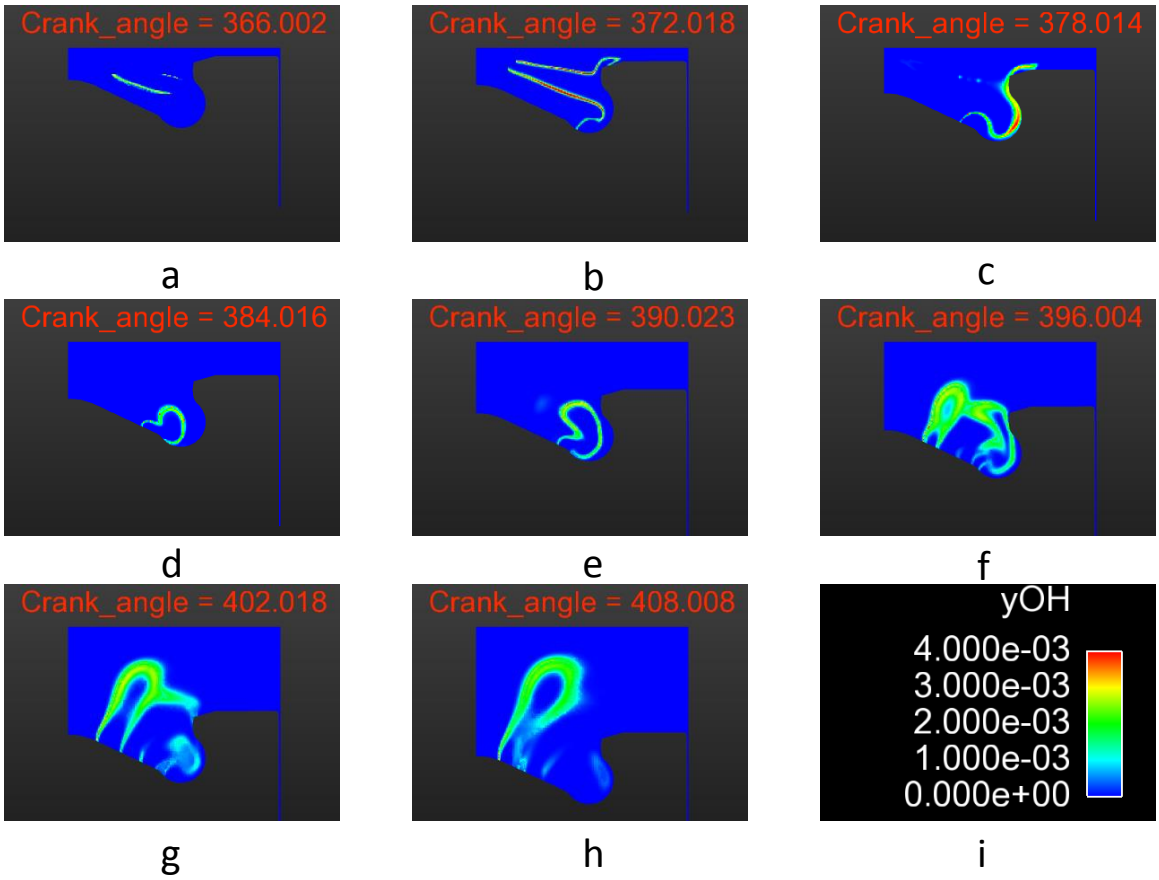

Figure 4.13 OH evolution for BMEP=2.5 bar from (a) 366 CAD to (h) 408 CAD; (i) shows the scale for OH in mass fraction

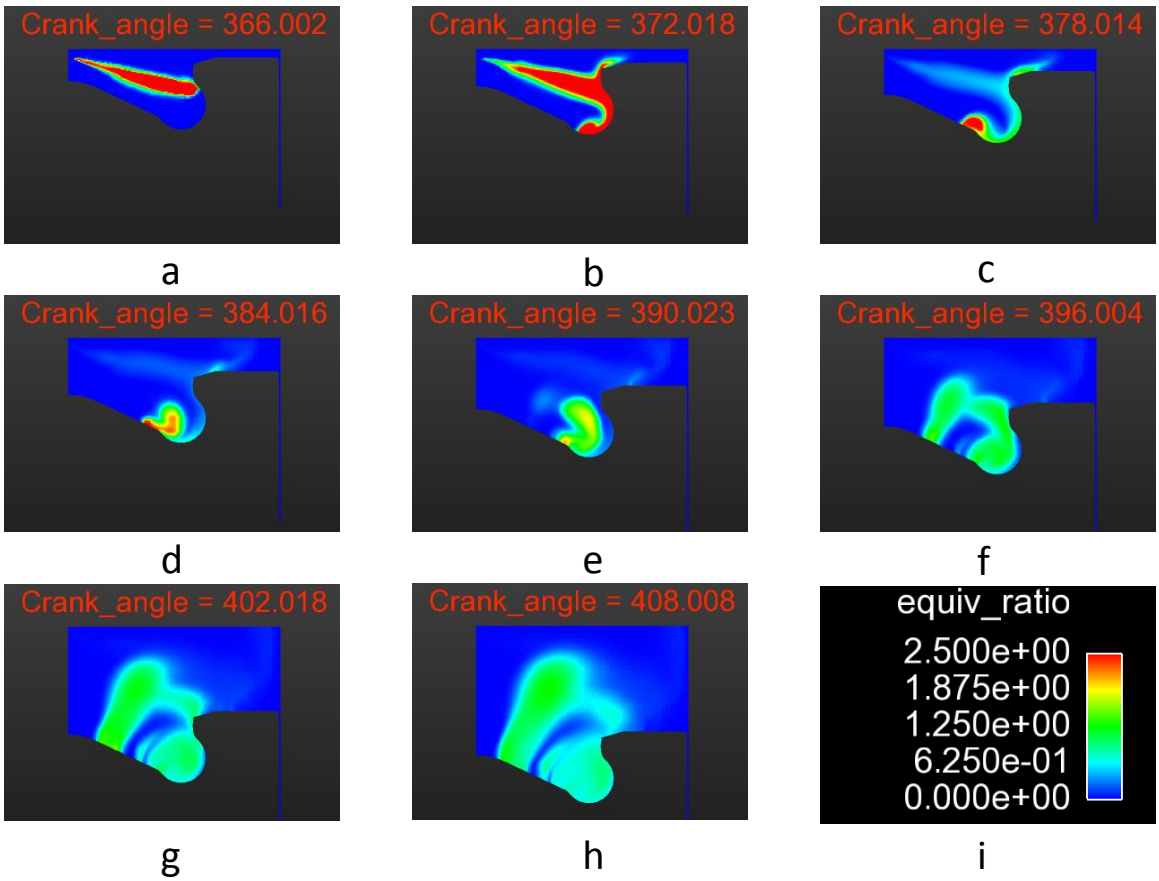

Figure 4.14 Equivalence ratio evolution for BMEP=2.5 bar from (a) 366 CAD to (h) 408 CAD; (i) shows the scale for equivalence ratio

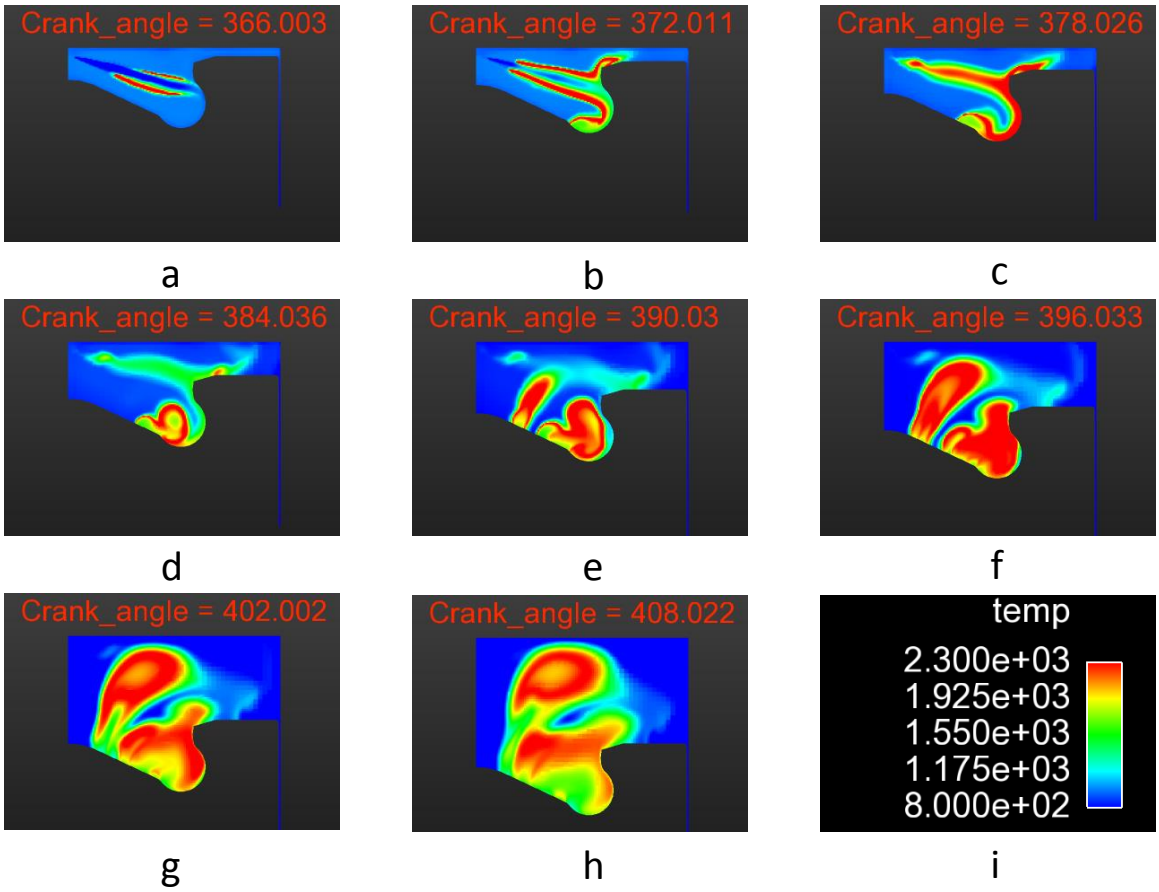

Figure 4.15 Local temperature evolution for BMEP=3.3 bar from (a) 366 CAD to (h) 408 CAD; (i) shows the scale for temperature in Kelvin.

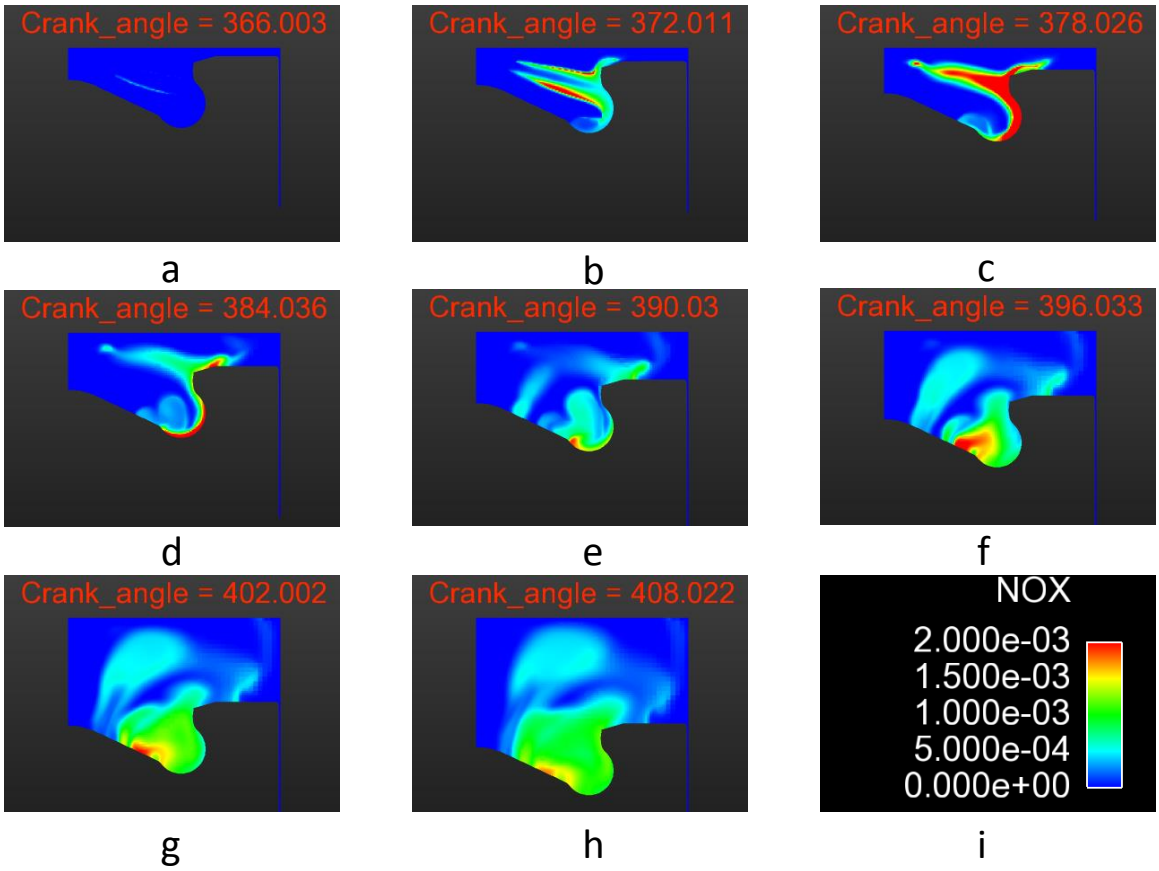

Figure 4.16 NOx evolution for BMEP=3.3 bar from (a) 366 CAD to (h) 408 CAD; (i) shows the scale for mass fraction

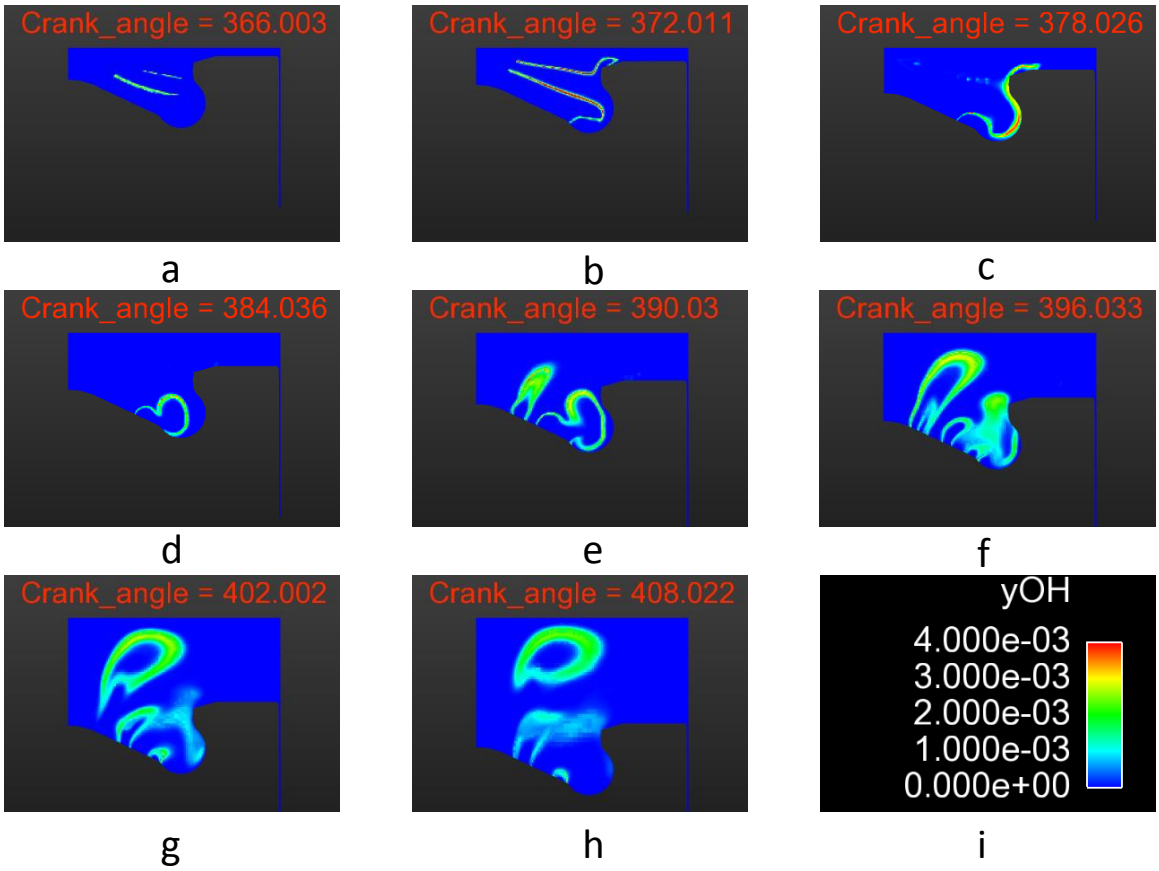

Figure 4.17 OH evolution for BMEP=3.3 bar from (a) 366 CAD to (h) 408 CAD; (i) shows the scale for OH in mass fraction

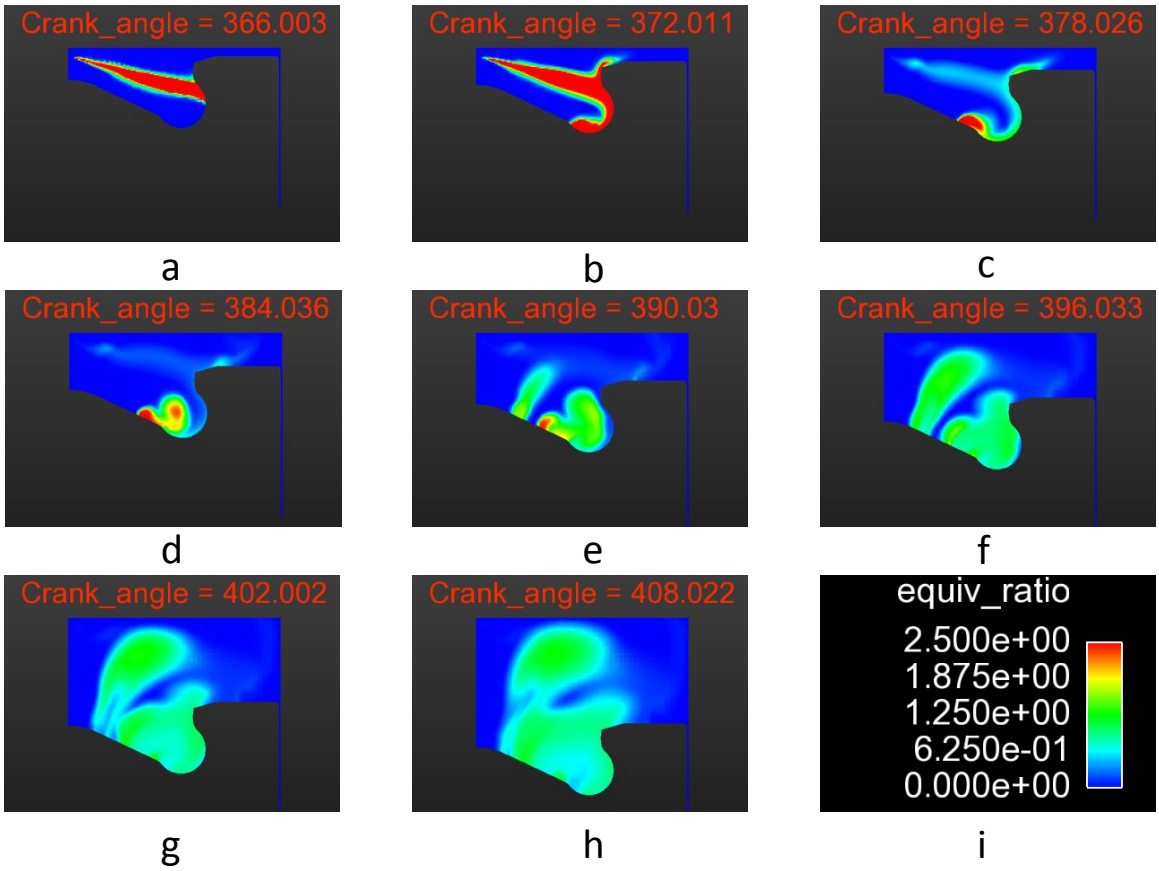

Figure 4.18 Equivalence ratio evolution for BMEP=3.3 bar from (a) 366 CAD to (h) 408 CAD; (i) shows the scale for equivalence ratio

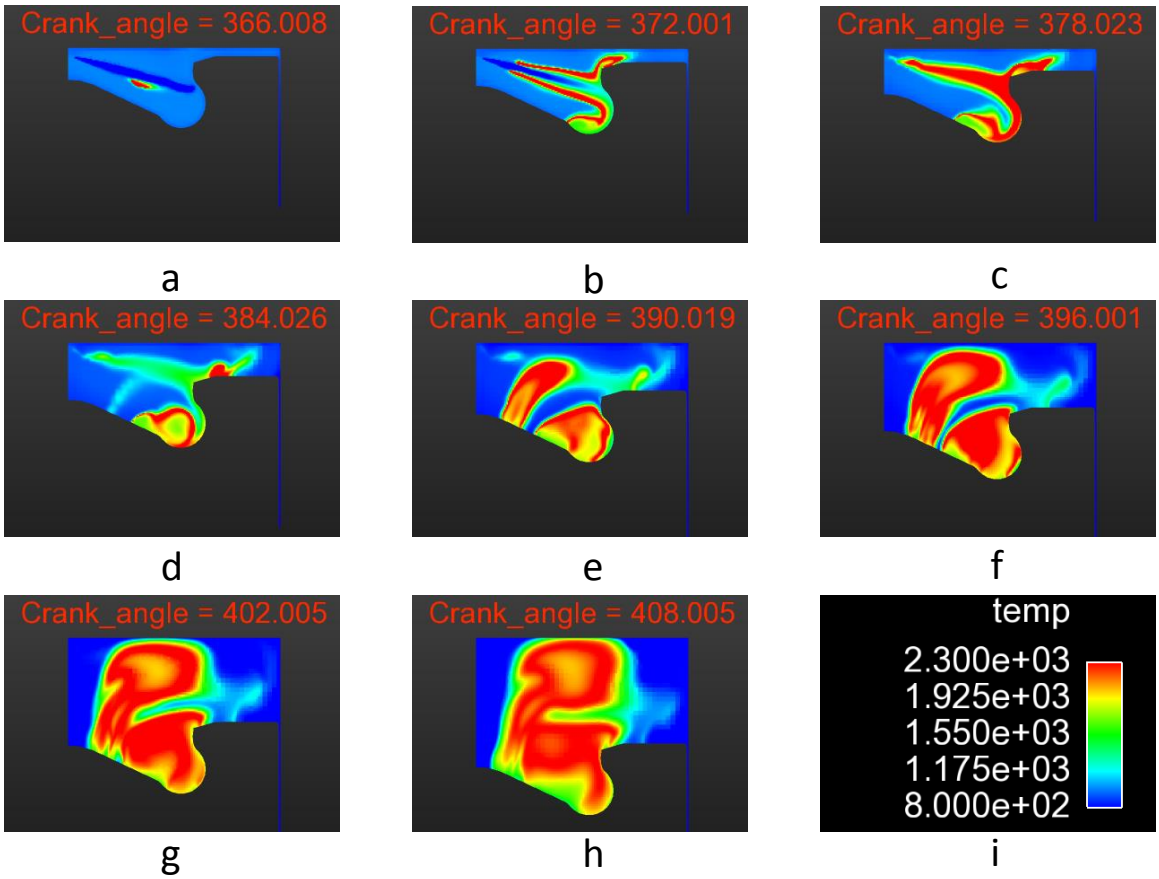

Figure 4.19 Local temperature evolution for BMEP=5.0 bar from (a) 366 CAD to (h) 408 CAD; (i) shows the scale for temperature in Kelvin

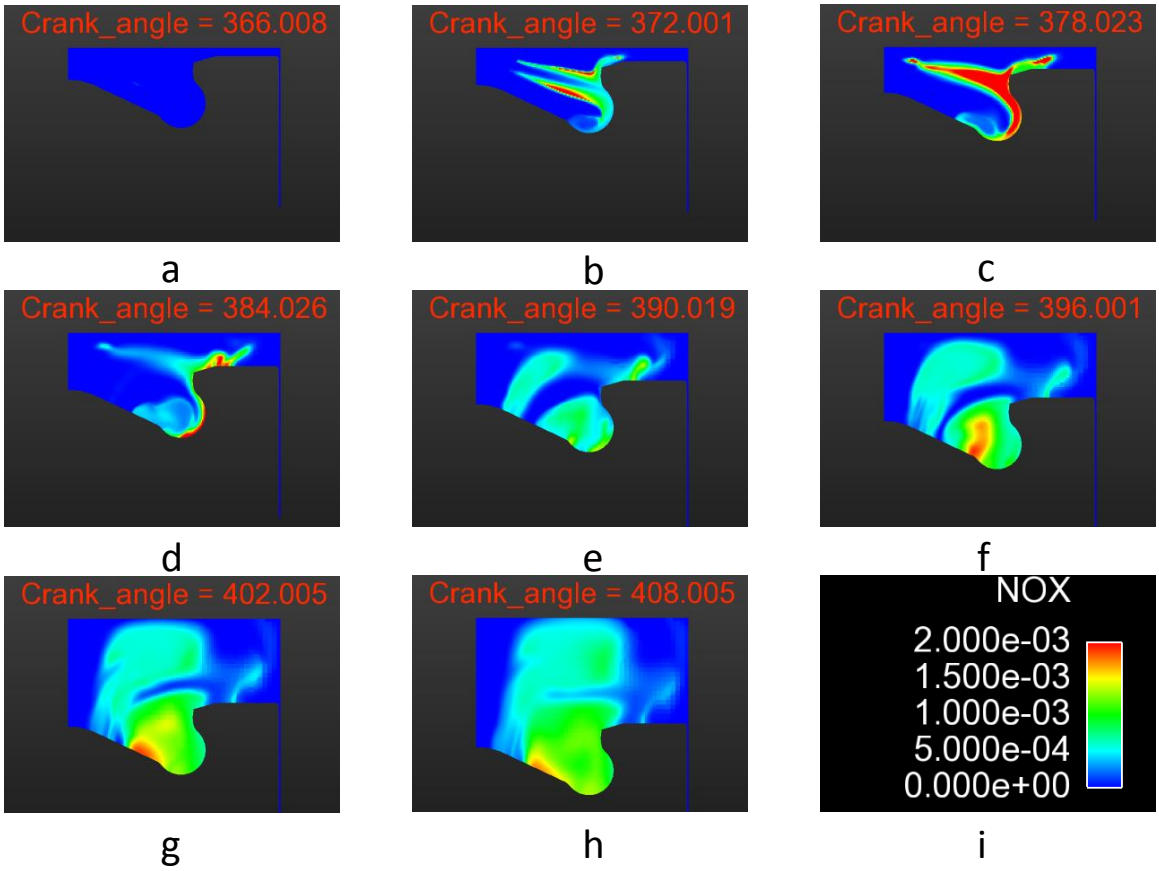

Figure 4.20 NOx evolution for BMEP=5.0 bar from (a) 366 CAD to (h) 408 CAD; (i) shows the scale for NOx in mass fraction

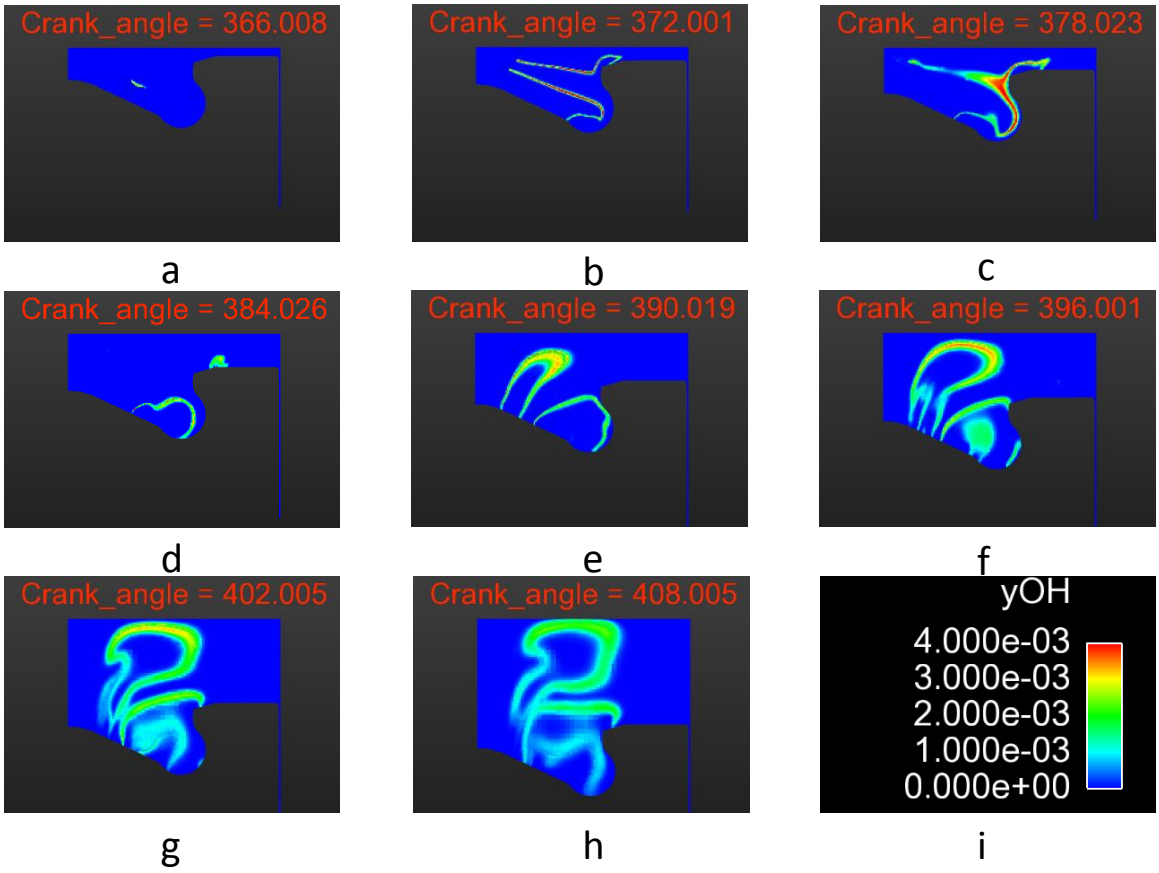

Figure 4.21 OH evolution for BMEP=5.0 bar from (a) 366 CAD to (h) 408 CAD; (i) shows the scale for OH in mass fraction

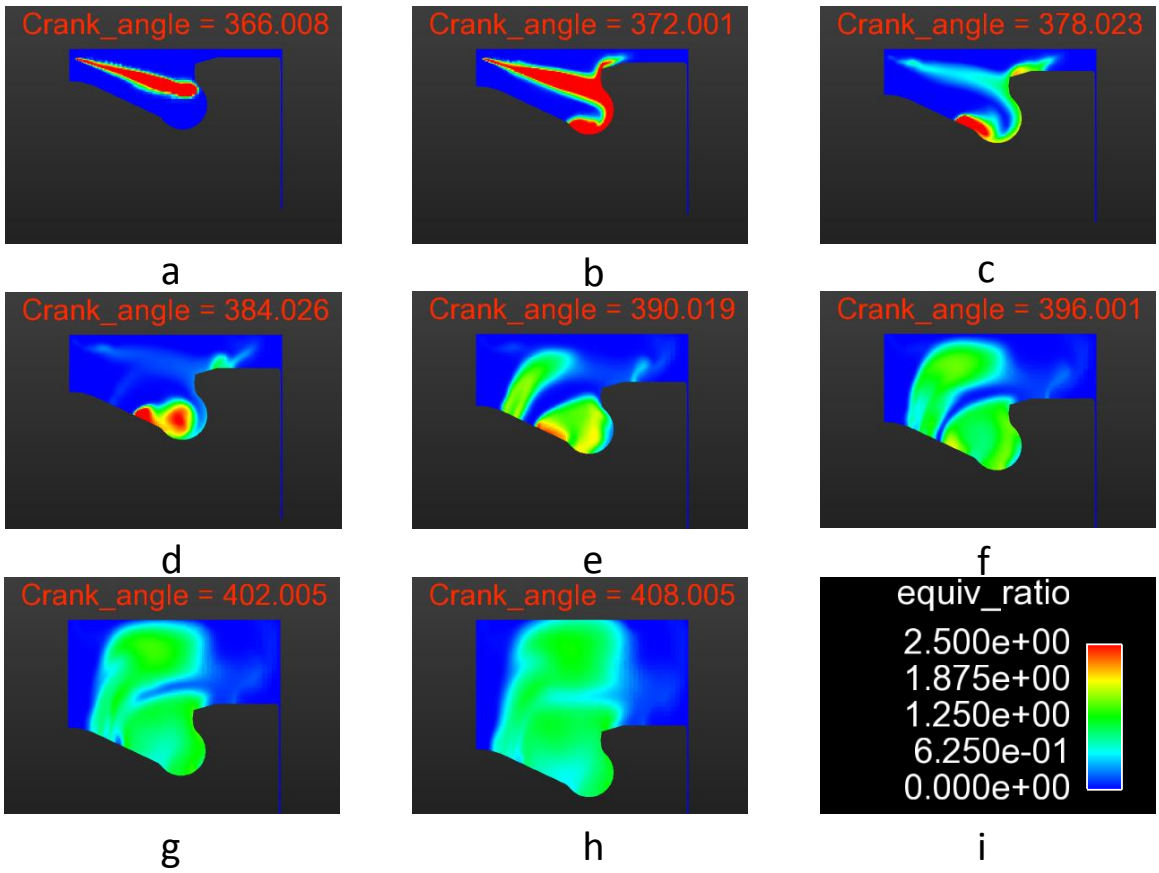

Figure 4.22 Equivalence ratio plot evolution for BMEP=5.0 bar from (a) 366 CAD to (h) 408 CAD; and (i) is shows the scale for equivalence ratio

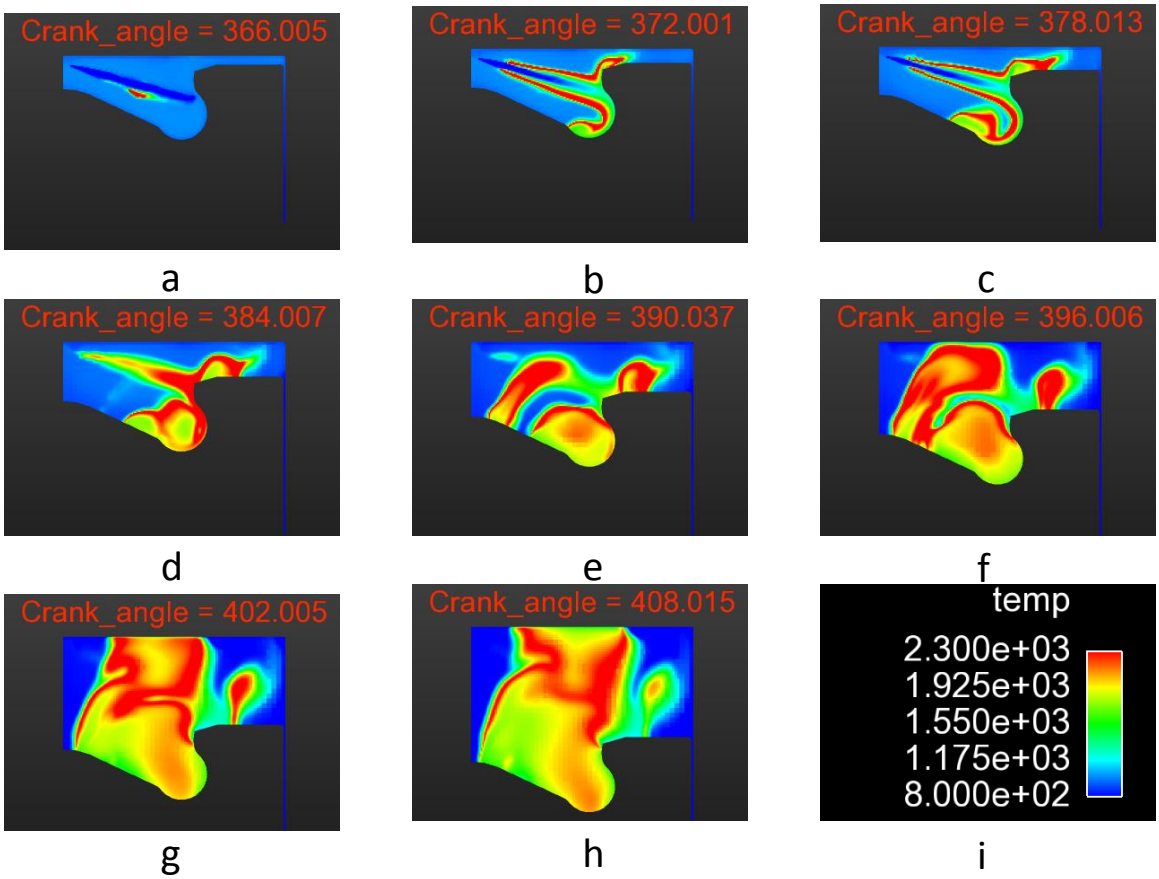

Figure 4.23 Local temperature evolution for BMEP=7.5 bar from (a) 366 CAD to (h) 408 CAD; (i) shows the scale for temperature in Kelvin

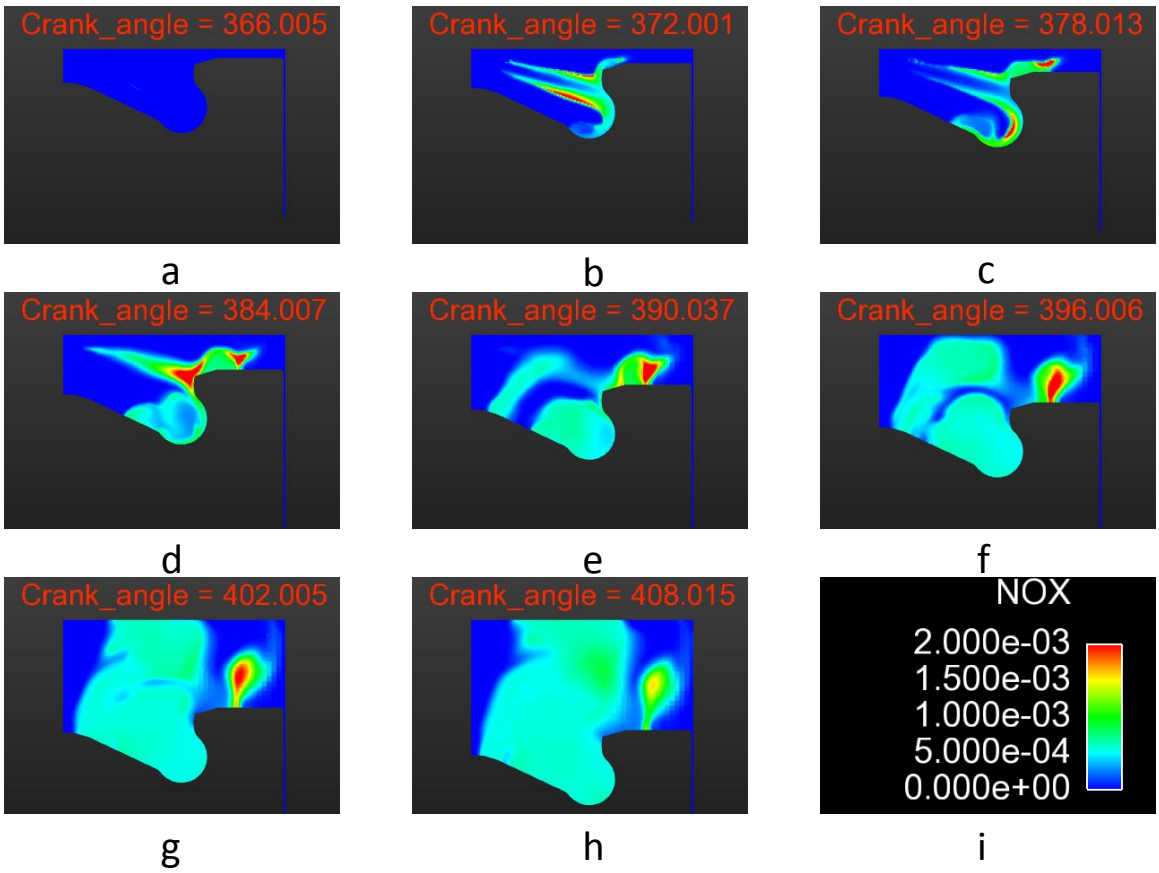

Figure 4.24 NOx evolution for BMEP=7.5 bar from (a) 366 CAD to (h) 408 CAD; (i) shows the scale for NOx in mass fraction

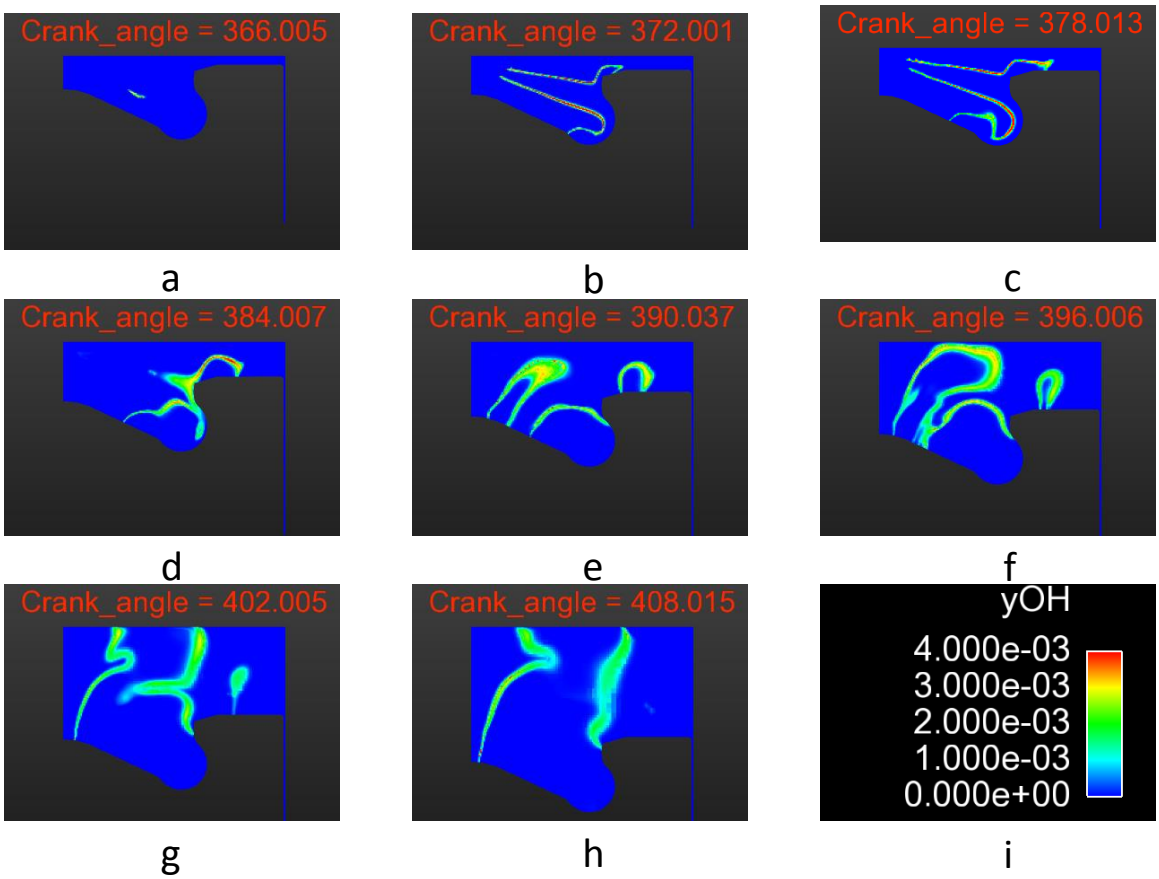

Figure 4.25 OH evolution for BMEP=7.5 bar from (a) 366 CAD to (h) 408 CAD; (i) shows the scale for OH in mass fraction

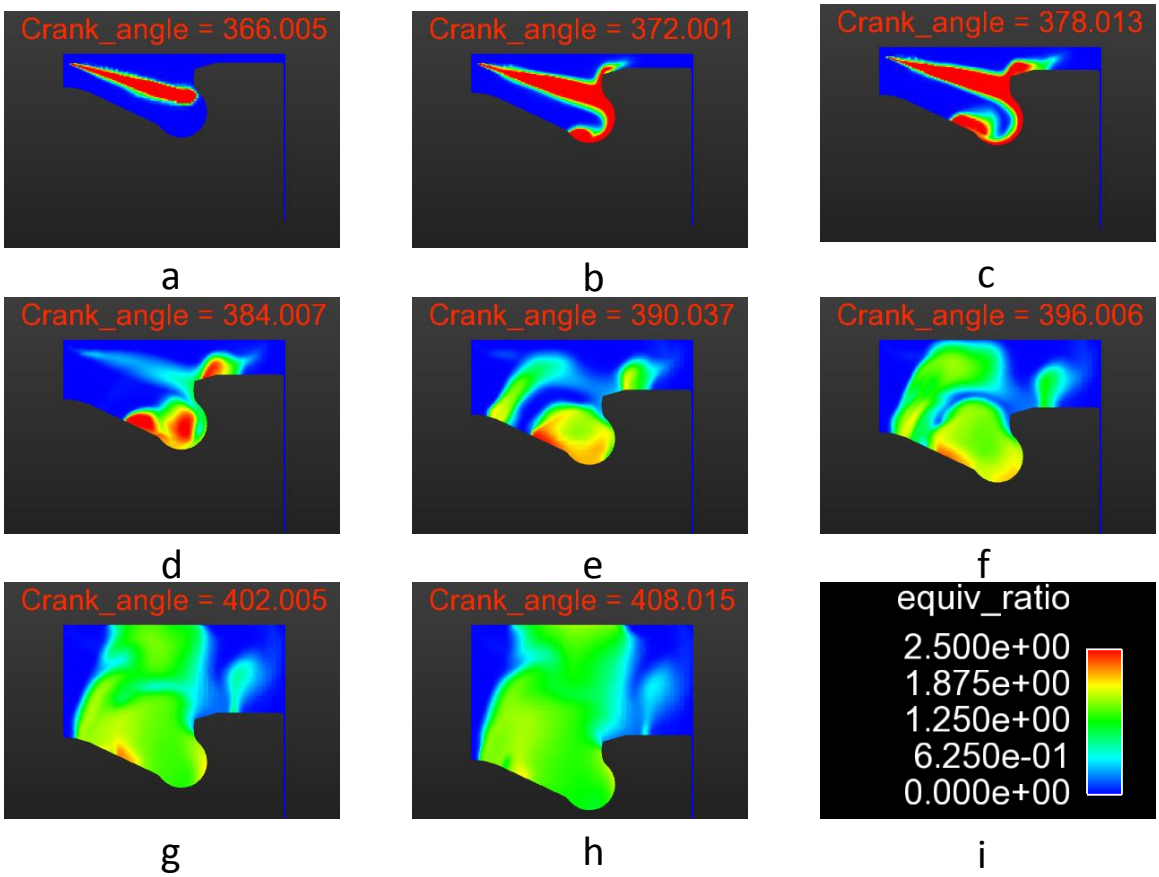

Figure 4.26 Equivalence ratio evolution for BMEP=7.5 bar from (a) 366 CAD to (h) 408 CAD; (i) shows the scale for equivalence ratio

4.4 Diesel-methane dual fuel combustion simulation results

Diesel-methane dual fuel combustion is simulated at seven different methane percentage energy substitution (PES) values at 3.3 bar BMEP; other operating conditions are listed in Table 4.3. The temperature and pressure at intake valve closing are determined using the Wiebe function-based model in GT POWER for pure diesel combustion at 3.3 bar BMEP and the same values are used for all dual fuel cases. The residual gas fraction is also obtained from the GT POWER simulations. A "top-hat-shaped" injection profile is again assumed for all dual fuel cases as measured injection

rate profiles were not available. The delay between the actual opening of the injector and the signal given from DRIVVEN is assumed to be 4.2 CAD. The SOI used for the simulations is 359.2 CAD.

Table 4.3 Diesel-methane dual fuel simulation test cases

Methane PES	PIVC (bar)	TIVC (K)	Diesel injected (kg/cycle/cyl)	Methane injected (kg/cycle cyl)	Cylinder head Temp.(K)	Liner Temp. (K)	Piston Temp. (K)
30	1.61	367	3.8E-05	1.3E-05	430	410	470
40	1.61	367	3.4E-05	1.9E-05	430	410	470
50	1.61	367	2.9E-05	2.6E-05	430	410	470
60	1.61	367	2.5E-05	3.3E-05	430	410	470
70	1.61	367	1.9E-05	4.3E-05	430	410	470
80	1.61	367	1.5E-05	5.7E-05	430	410	470
90	1.61	367	8.1E-06	6.8E-05	430	410	470

A comparison of predicted and experimental in-cylinder pressure, apparent heat release rate (AHRR), indicated specific oxides of nitrogen (NOx), indicated specific hydrocarbons (ISHC), indicated specific carbon monoxide (ISCO), and combustion phasing (CA50) are given in Figures 4.27 through Figure 4.37 for all PES cases. Figures 4.38 through Figure 4.41 show crank angle-resolved maximum temperature, NOx, HC, and CO evolution for all PES cases. All plots are clipped in the middle of the computational sector in the Y plane. Figure 4.42 shows the injection pressure profile obtained from the simulation. The maximum injection pressure obtained for all PES cases is around 500 bar, which matches the experimental injection pressure. This gives confidence in the strategy used to evaluate the coefficient of discharge (CD) of the injector nozzle. The color maps are presented in a section (i.e., XZ plane) that was

obtained by cutting the computational domain (viewing from the top) in the middle of the sector along the cylinder axis. The color map of the evolution of local temperature, NOx, OH, equivalence ratio, CO_2, CO, and CH_4 with respect to CAD is shown in Figures 4.43 through Figure 4.70 for 30, 60, 80 and 90 PES cases. Again, in general, the predictions of in-cylinder pressure and AHRR are reasonably good for all PES cases with some exceptions. Compression pressures in all cases are slightly over-predicted in all cases because the initial pressure and temperature at IVC are taken from GT POWER simulations for pure diesel case at a BMEP of 3.3 bar. It is evident that the first stage heat release is overpredicted in all cases. This may be attributed to uncertainties in the chemical kinetic mechanism used for the dual fuel simulations, the injection rate profile, and initial conditions like swirl ratio and temperature at IVC. The start of ignition is well predicted for all cases except for 90 PES. This can be explained based on the fact that the chemistry mechanism used for the dual fuel simulation was originally tailored for dual fuel homogenous charge compression ignition (HCCI) combustion inside the cylinder. However, it must be noted that the actual dual fuel combustion will not be homogeneous throughout the cylinder, and the chemical kinetic mechanism may not perform as well under heterogeneous conditions.

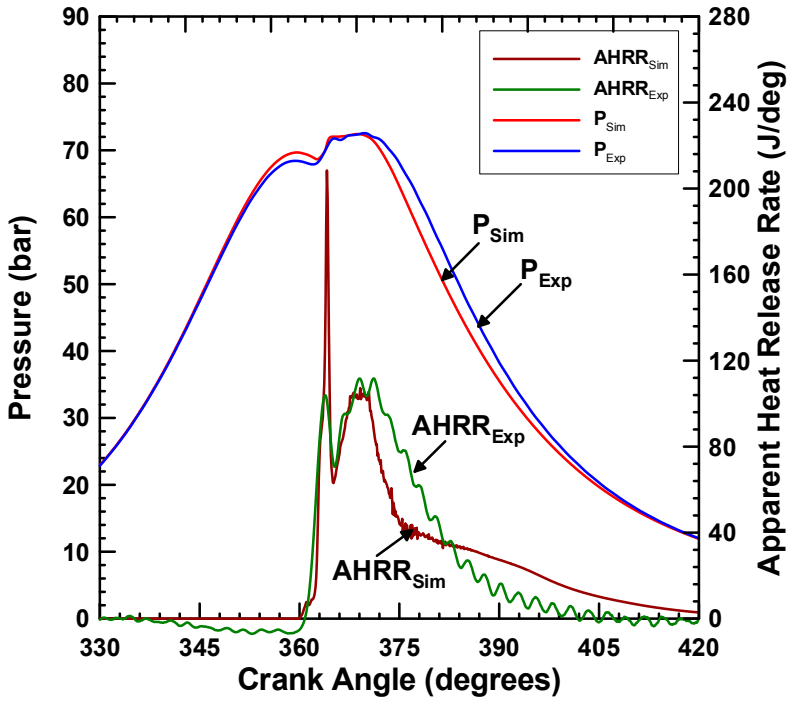

Figure 4.27 Pressure and AHRR comparisons for 30 PES at BMEP =3.3 bar

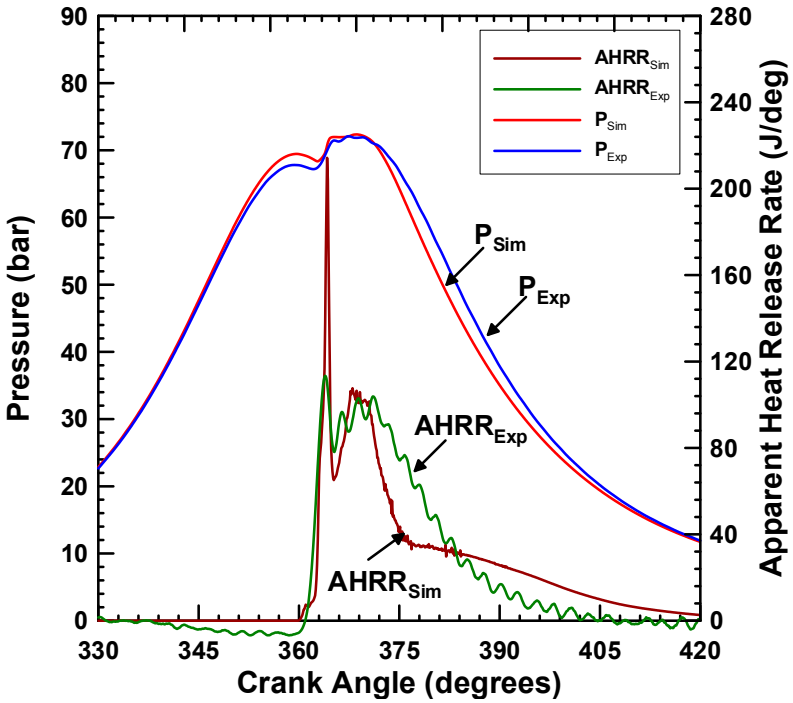

Figure 4.28 Pressure and AHRR comparisons for 40 PES at BMEP= 3.3 bar

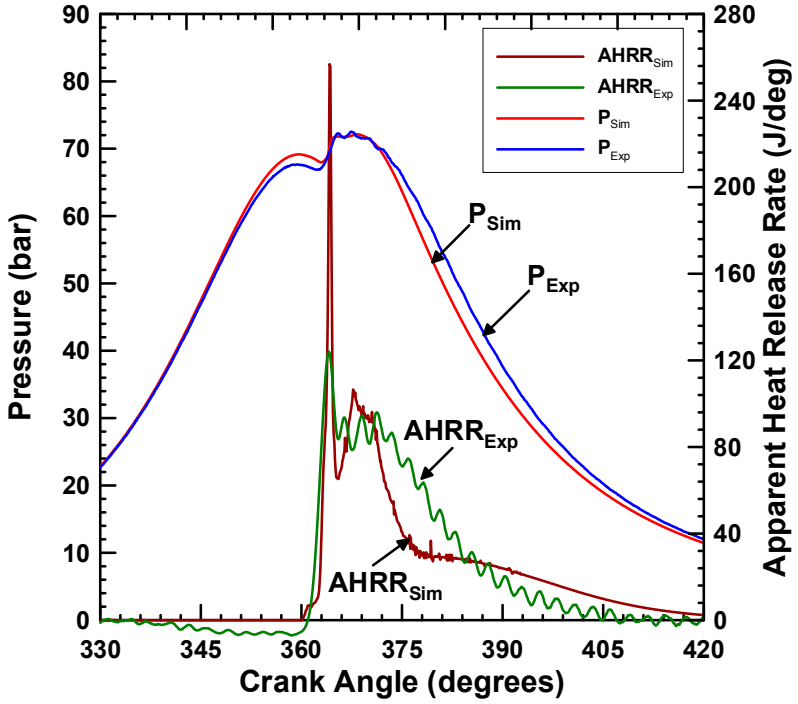

Figure 4.29 Pressure and AHRR comparisons for 50 PES at BMEP =3.3 bar

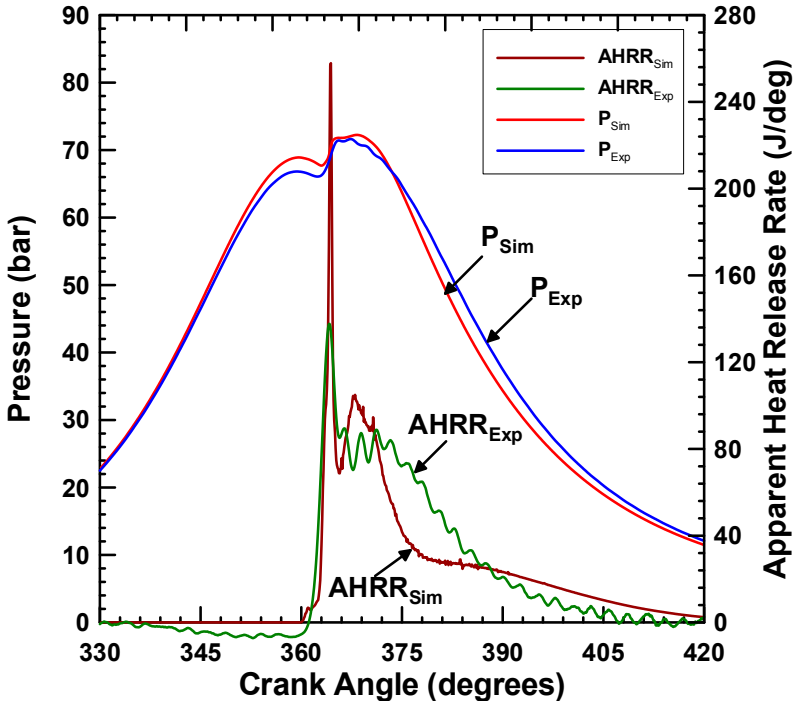

Figure 4.30 Pressure and AHRR comparisons for 60 PES at BMEP =3.3 bar

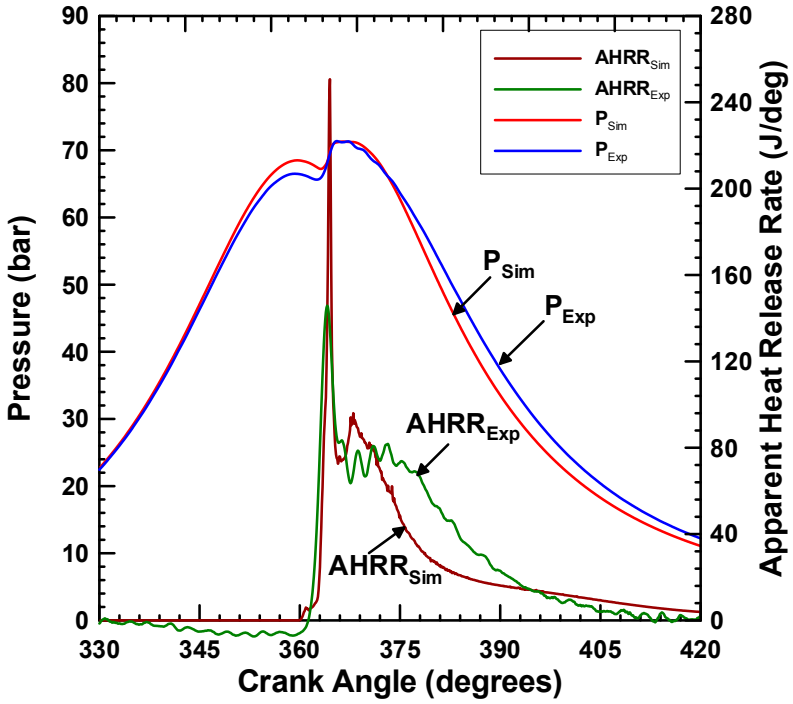

Figure 4.31 Pressure and AHRR comparisons for 70 PES at BMEP =3.3 bar

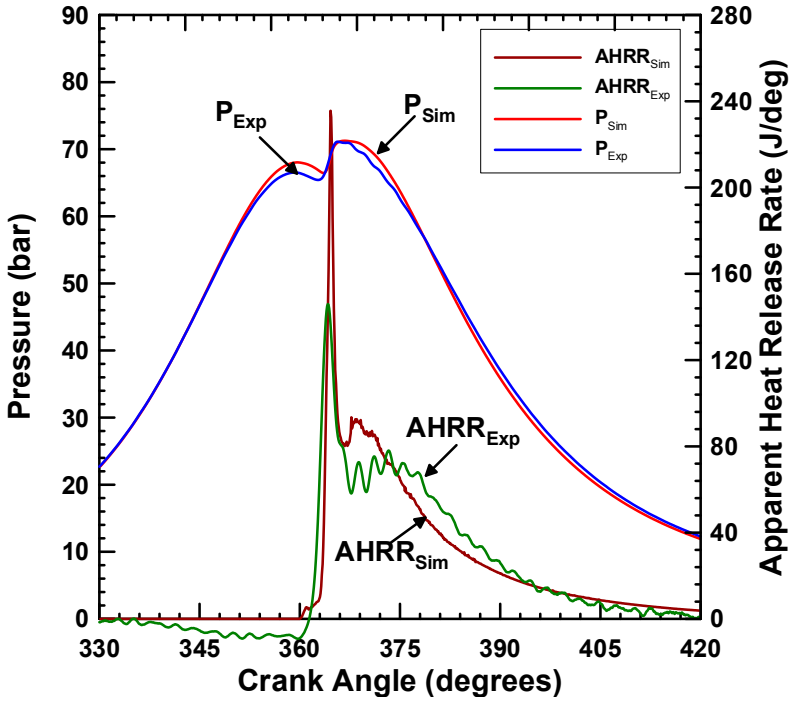

Figure 4.32 Pressure and AHRR comparisons for 80 PES at BMEP =3.3 bar

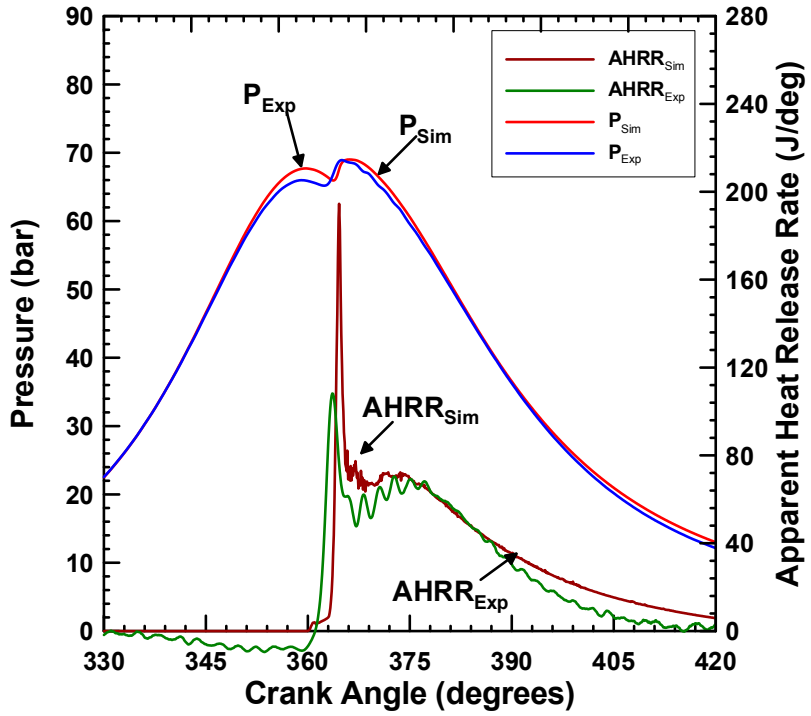

Figure 4.33 Pressure and AHRR comparisons for 90 PES at BMEP =3.3 bar

Combustion phasing trends as well as the actual values are correctly predicted compared to the experiments. On the other hand, while NOx trends are predicted correctly compared to the experiments (i.e., decreasing NOx trend with increasing PES), the predicted values are higher than the experimental values from 30% to 70 PES, and match at 80 PES, and are lower at 90 PES. Higher NOx predictions may be because of higher prediction of compression pressure, which lead to higher in-cylinder temperature. Higher NOx may have been caused due to lower Schmidt number value which is kept constant as used in pure diesel simulation. As different mechanism is used for diesel-methane dual fuel simulation, it makes more sense to change that value in future work. Lower NOx predicted at 80 and 90 PES may be because ignition is delayed, which causes

combustion to occur later in the expansion process, leading to lower maximum temperatures and lower NOx formation within the cylinder. The predicted NOx trends can be also observed in the NOx mass formation plot in Fig 4.39. The ISHC emission trend (i.e., increasing ISHC with increasing PES) is correctly predicted from 30 - 70 PES; however, the further experimentally observed increase in ISHC at 80 and 90 PES are not captured in the predictions. Experimental HC emissions for cases above 70 PES exceeded the operational limit of 10000 ppm of the heated flame ionization detection (HFID) analyzer used in the experiments. For all those cases, the ISHC was reevaluated keeping $\Phi_{emission}$ within 5% of measured equivalence ratio [46]. The decrease in ISHC emissions at 90 PES may be because of error in assigning initial condition like intake temperature, swirl ratio, initial kinetic energy and chemical kinetic mechanism used for the dual fuel simulations. The CO emissions trend is well captured by the simulation results. The CO formation and oxidation rate are highest for 30 methane PES and lowest for 90 methane PES. This indicates that the majority of CO arises from diesel at lower PES and due to higher in cylinder temperatures the CO oxidation rate is also higher. The amount of CO formed at high methane PES is lower but due to lower in-cylinder temperatures, most of the CO does not get oxidized. This behavior can be confirmed from the CO mass plot shown in Fig 4.41.

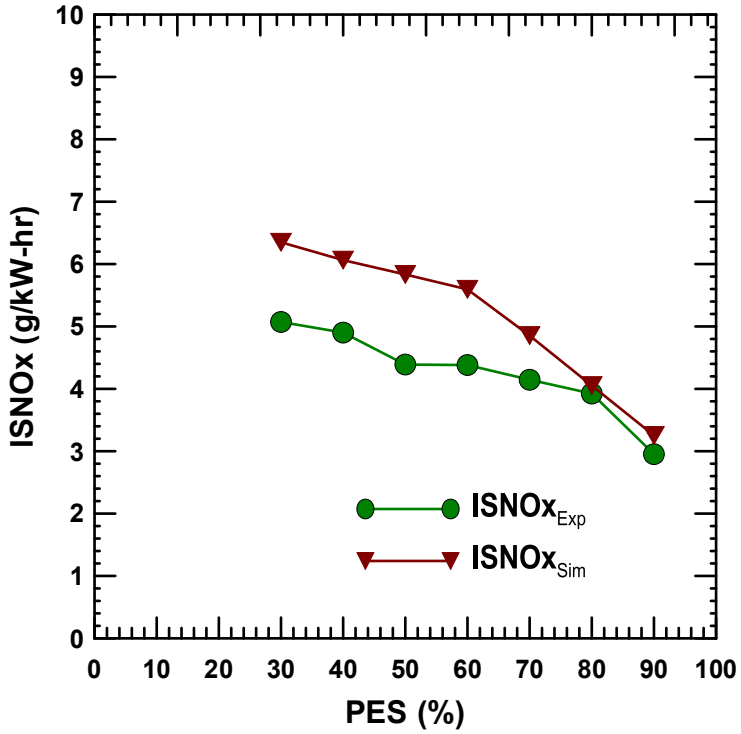

Figure 4.34 Experimental and simulation ISNOx trend comparisons for PES (30-90) at BMEP =3.3 bar

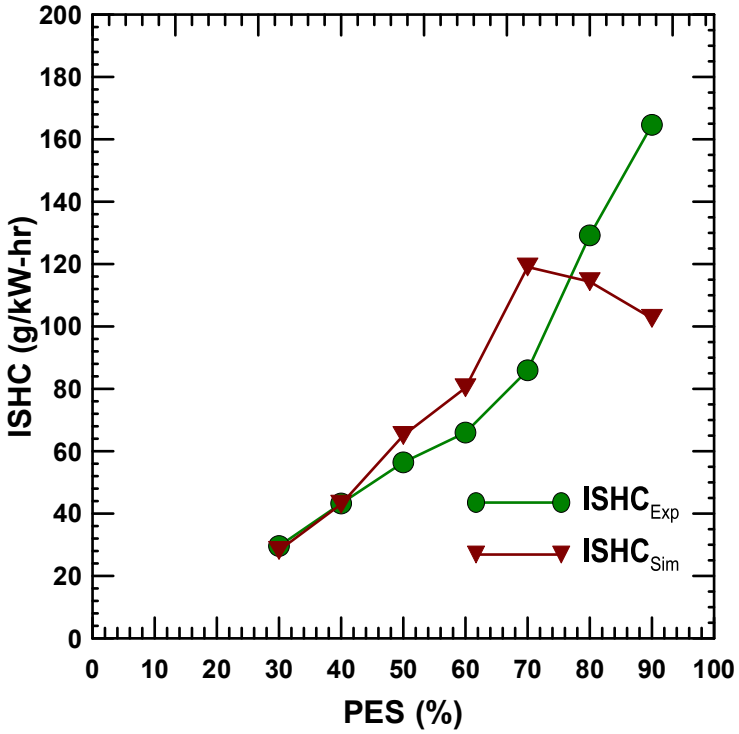

Figure 4.35 Experimental and simulation ISHC trend comparisons for PES (30-90) at BMEP =3.3 bar

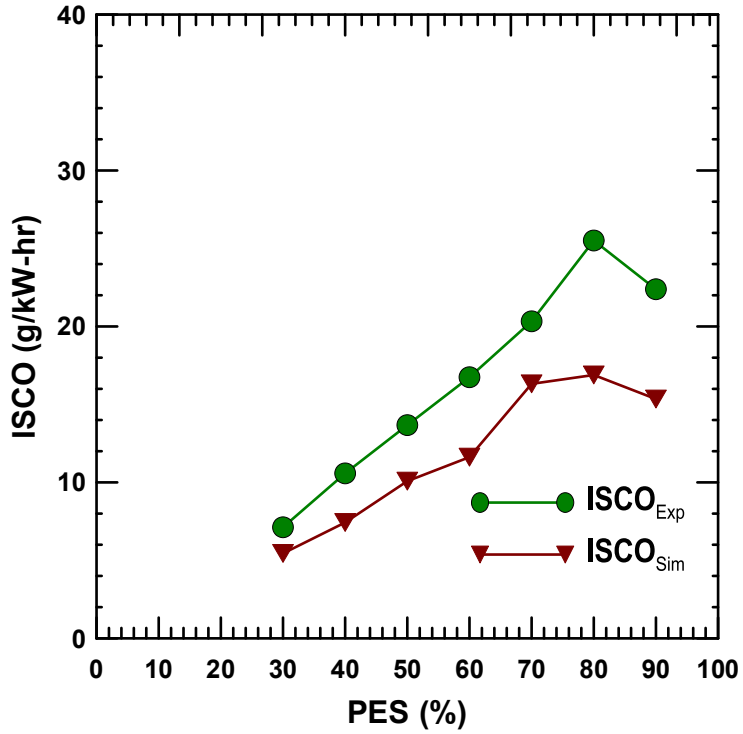

Figure 4.36 Experimental and simulation ISCO trend comparisons for PES (30-90) at BMEP =3.3 bar

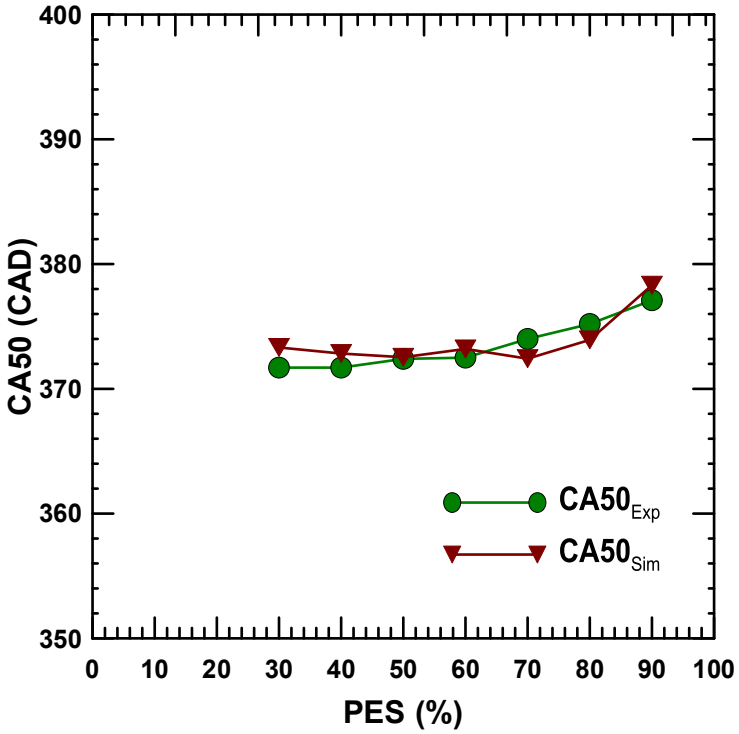

Figure 4.37 Experimental and simulation combustion phasing (CA50) trend comparisons for PES (30-90) at BMEP =3.3

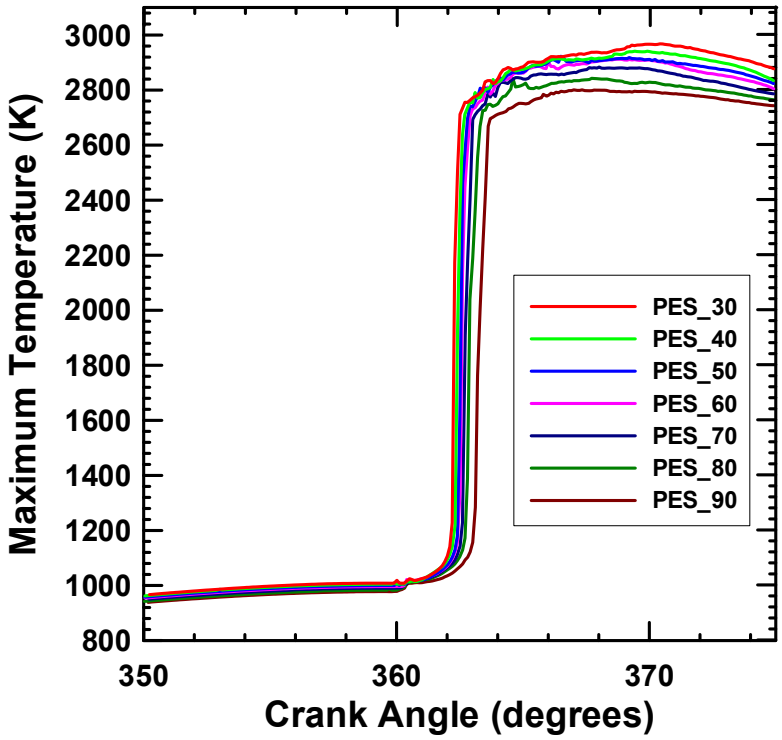

Figure 4.38 Maximum temperature plot for PES (30-90) at BMEP =3.3 bar

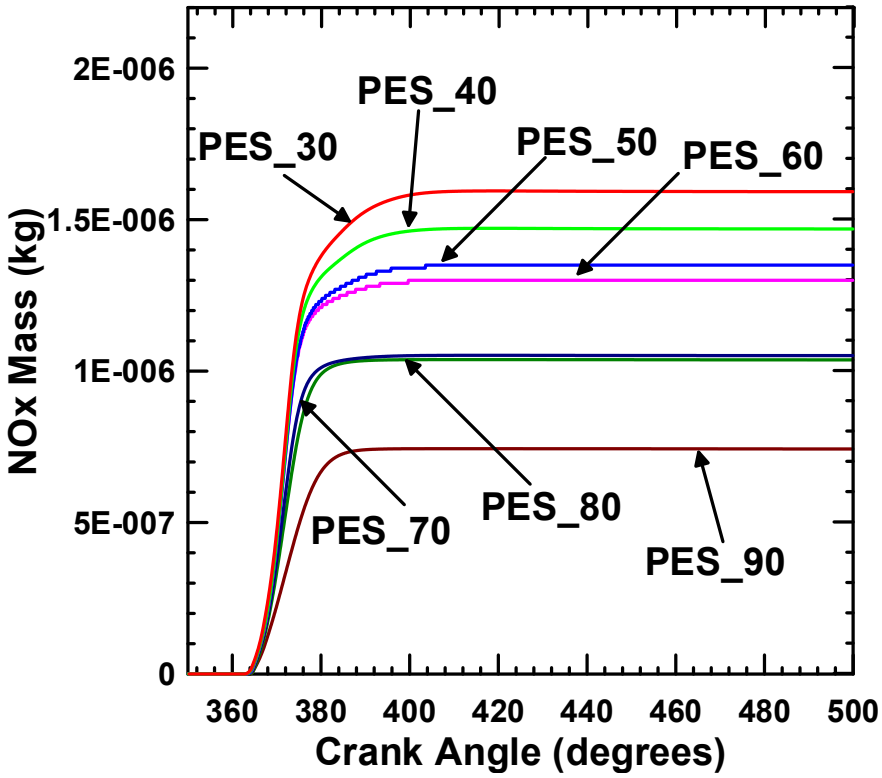

Figure 4.39 NOx formation plot for PES 30-90 at BMEP 3.3 bar.

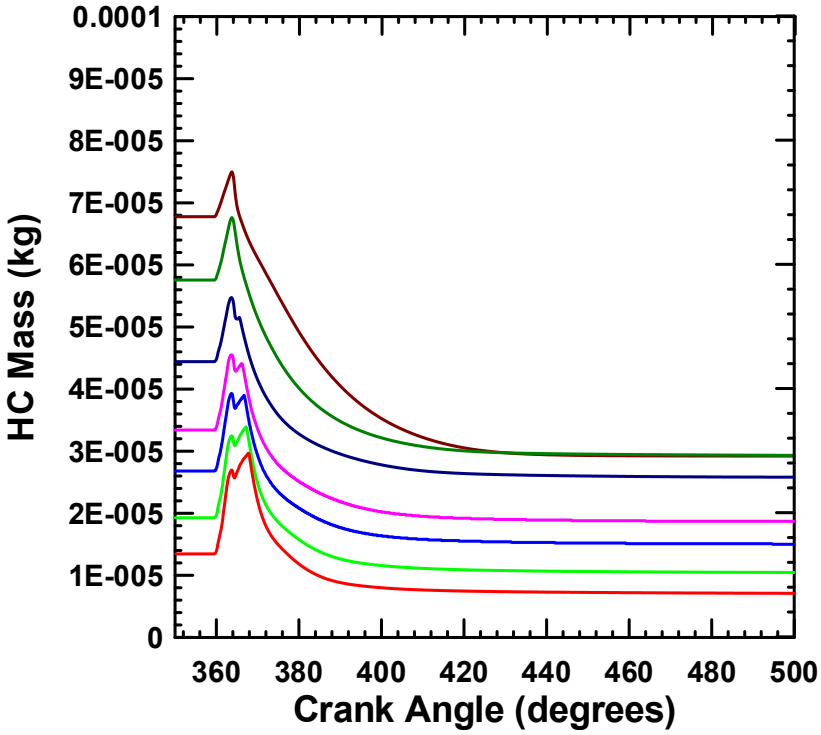

Figure 4.40 HC formation plot for PES (30-90) at BMEP =3.3 bar

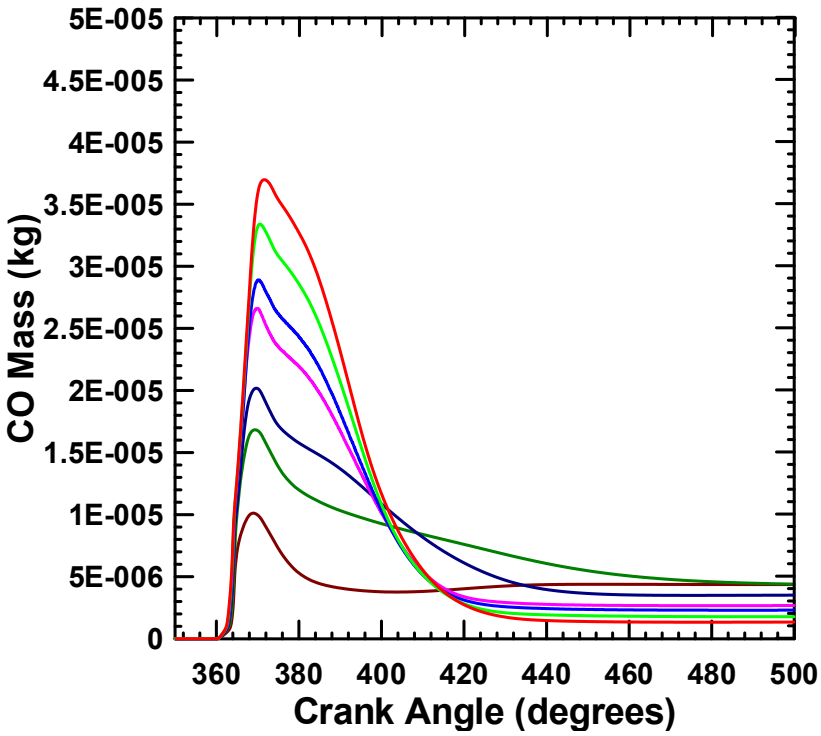

Figure 4.41 CO formation plot for PES (30-90) at BMEP =3.3 bar

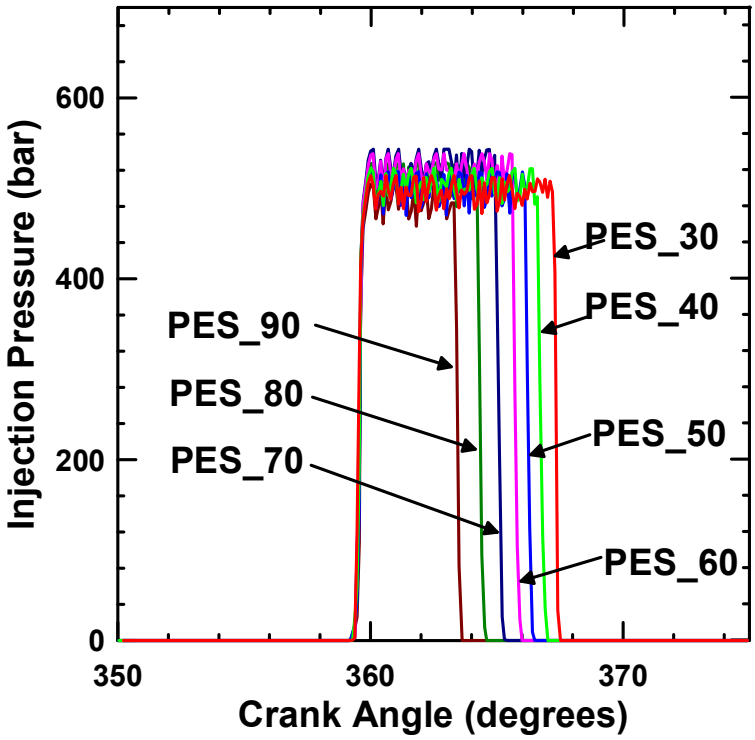

Figure 4.42 Injection pressure plot for PES (30-90) at BMEP =3.3

Figures 4.43 through 4.49 show color maps of the local temperature, NOx, OH, equivalence ratio, CO_2, CO, and CH_4 for the BMEP of 3.3 bar at 30 PES. Similar to diesel combustion, the NOx formation can be seen to occur just outside the diffusion flame where the local equivalence ratios are near stoichiometric. High OH concentrations are confined to a narrow region around the diffusion flame, where the equivalence ratio is near stoichiometric. From Figures 4.48 and 4.49, it may be observed that CO and HC oxidation occur in the same spatial regions, and due to the competition between the two oxidation processes, CO remains unoxidized. From Figure 4.49, it can be seen that most of the HC are present near the cylinder wall and crevices, and therefore, do not participate in the combustion process, becoming the primary cause of HC emissions. Further, Figure 4.47 shows the reduced formation of CO_2 around the cylinder

wall and crevices, thereby confirming combustion inactivity in those regions. Figures 4.50 through 4.70 show color maps of local temperature, NOx, OH, equivalence ratio, CO_2, CO, and CH_4 for the BMEP of 3.3 bar at PES values of 60, 80, and 90, respectively. Similar trends as described above for 30 percentage for all other cases. From these plots, it can seen that combustion spreads further into other regions within the cylinder (not directly affected by the diesel jet) with increasing methane PES. This is partly due to the presence of higher amounts of methane in the diesel jet surroundings and partly due to the fact that a greater fraction of the charge becomes combustible with increasing equivalence ratio. This increase in the size of the combusting regions with increasing methane PES can also be confirmed with the OH evolution color maps.

The major differences between pure diesel combustion and diesel-methane dual fuel combustion at 80 PES are summarized now. From Figure 4.10, Fig 4.15, Fig 4.38 and Figure 4.57, it can be concluded that dual fuel combustion is generally cooler than pure diesel combustion. This can be attributed to a variety of factors, including the higher specific heat ratio of methane, which decreases temperature at the end of compression and higher ignition delay due to the lower reactivity of methane. The NOx emissions are lower for 80 PES than pure diesel combustion because of lower in-cylinder temperatures. Hydrocarbon emissions increase with dual fuel combustion due to incomplete combustion of methane around the cylinder wall and in the cylinder crevices compared to pure diesel combustion. Carbon monoxide emissions are also higher for 80 PES, either due to the apparent competition between HC and CO oxidation in dual fuel combustion; for example at lower PES (e.g., 30 PES), the CO formation may be higher but the net CO emissions are lower due to more rapid CO oxidation compared to 80 PES.

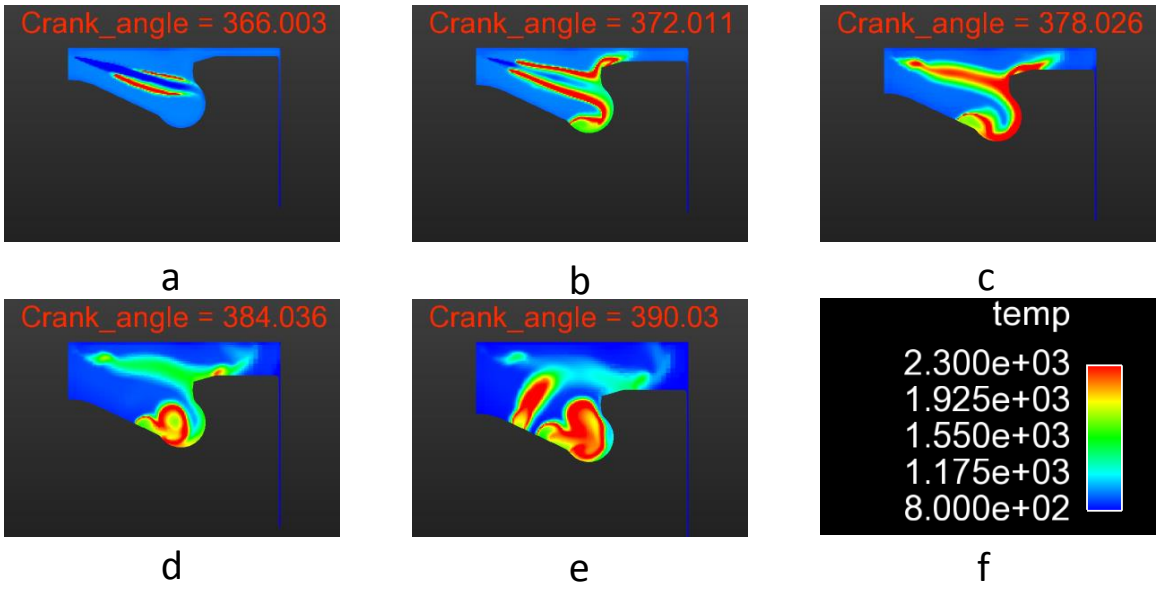

Figure 4.43 Local temperature evolution for BMEP=3.3 bar at 30 PES from (a) 366 CAD to (e) 390 CAD; (f) shows the scale for temperature in Kelvin

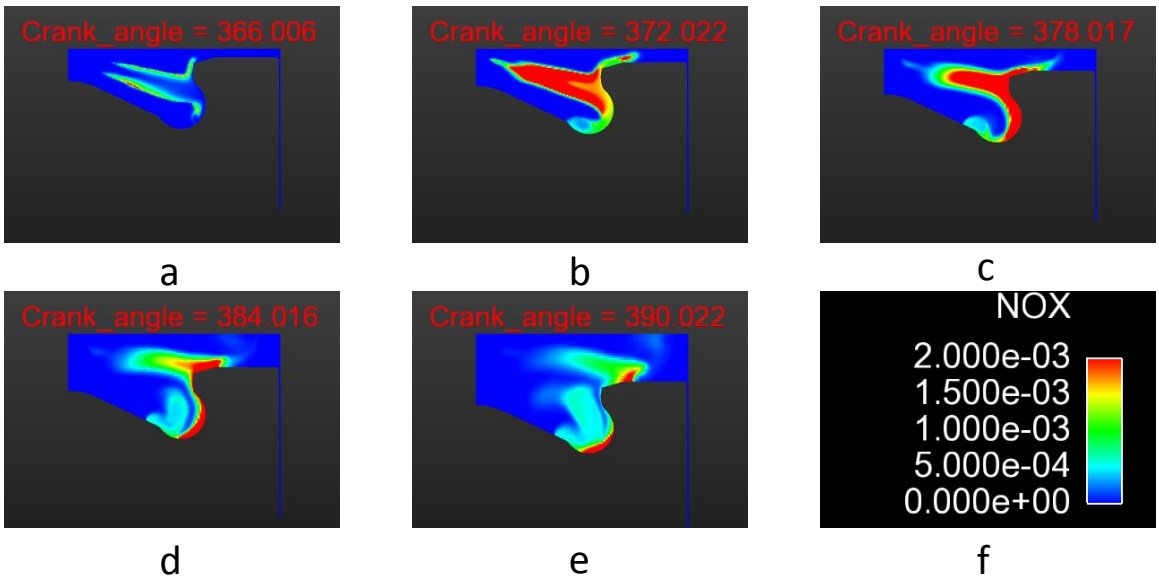

Figure 4.44 NOx evolution for BMEP=3.3 bar at 30 PES from (a) 366 CAD to (e) 390 CAD; (f) shows the scale for NOx in mass fraction

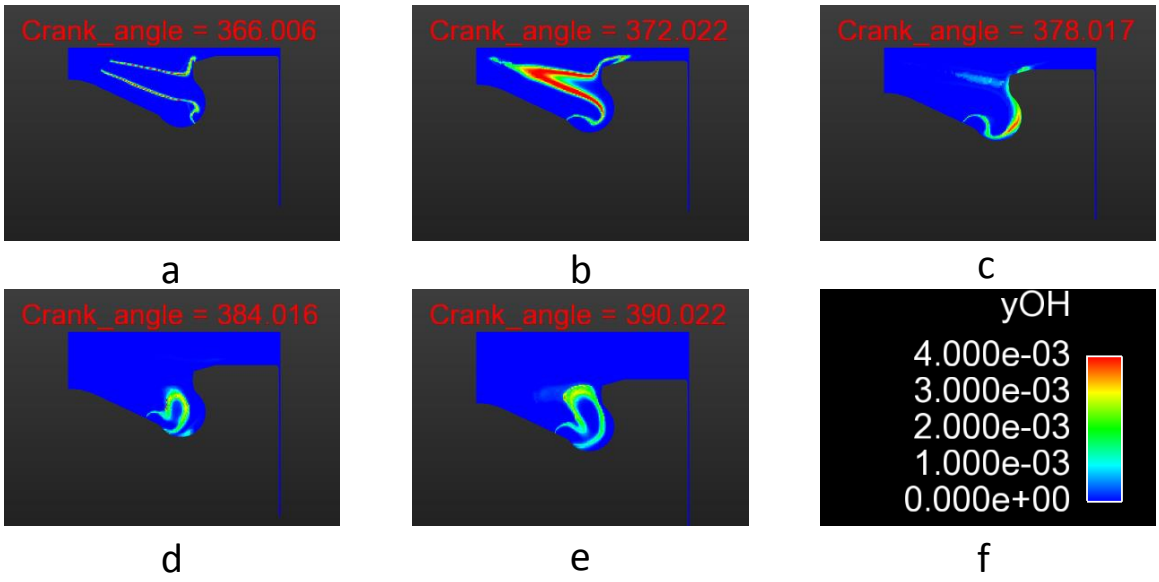

Figure 4.45 OH evolution for BMEP=3.3 bar at 30 PES from (a) 366 CAD to (e) 390 CAD; (f) shows the scale for OH in mass fraction

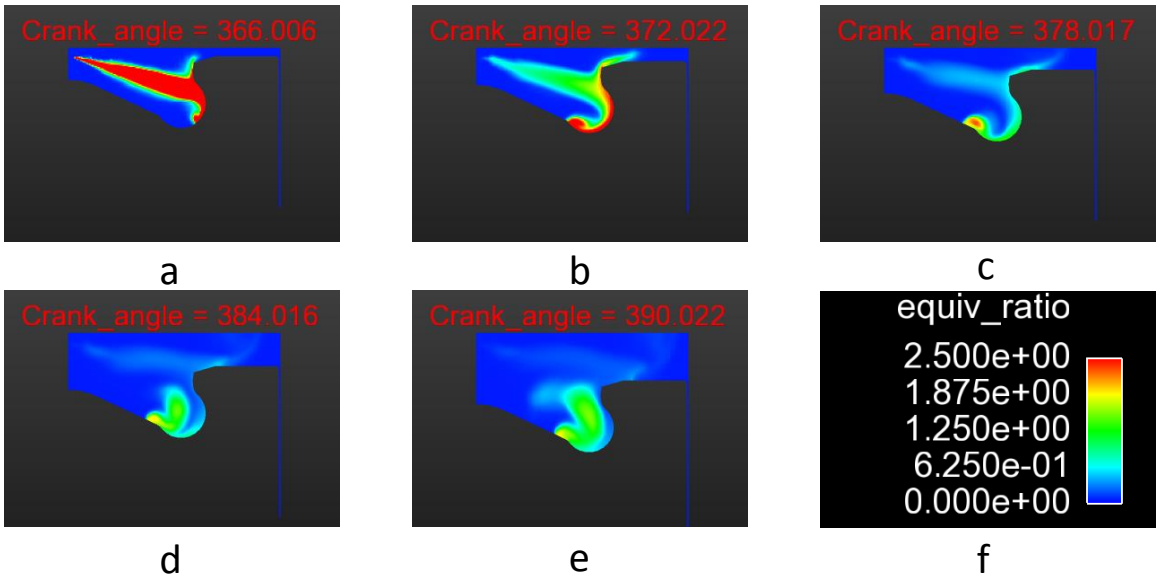

Figure 4.46 Equivalence ratio evolution for BMEP=3.3 bar at 30 PES from (a) 366 CAD to (e) 390 CAD; (f) shows the scale for equivalence ratio

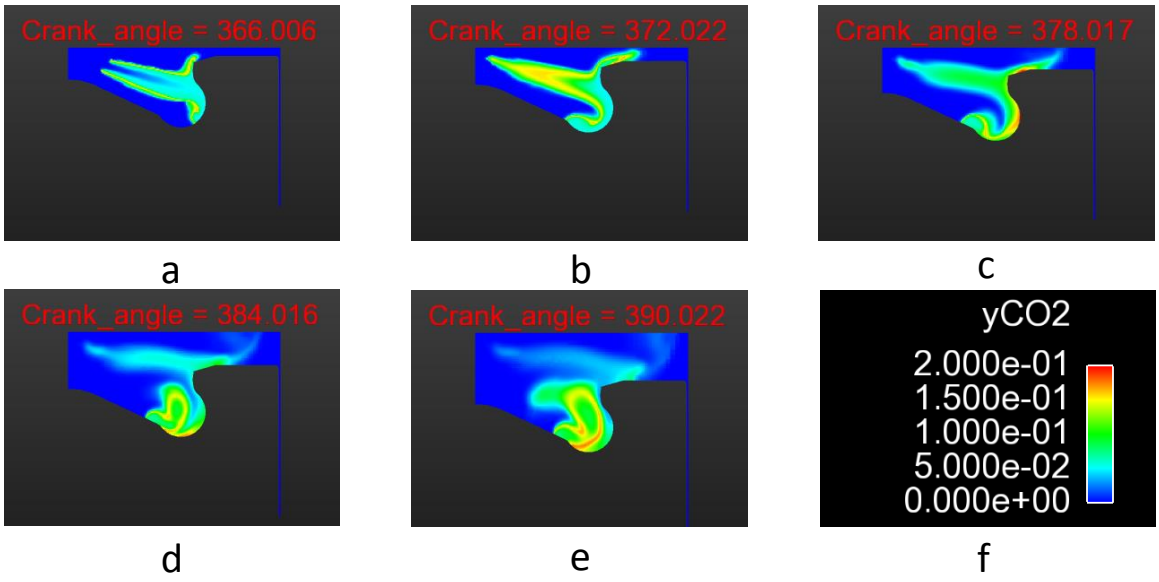

Figure 4.47 CO_2 evolution for BMEP=3.3 bar at 30 PES from (a) 366 CAD to (e) 390 CAD; (f) shows the scale for CO_2 in mass fraction

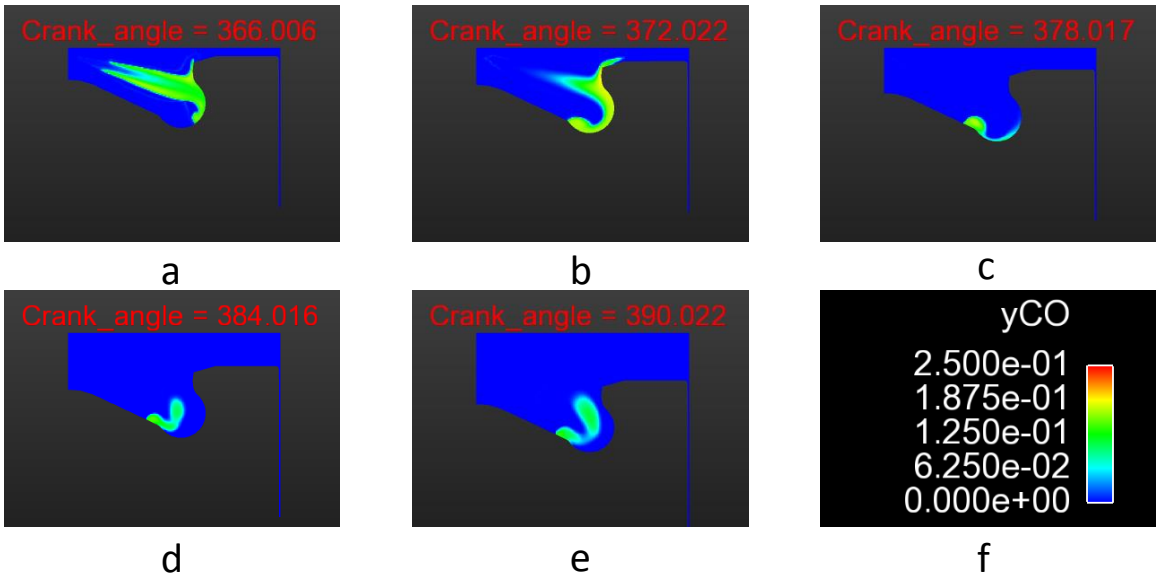

Figure 4.48 CO evolution for BMEP=3.3 bar at 30 PES from (a) 366 CAD to (e) 390 CAD; (f) shows the scale for CO in mass fraction

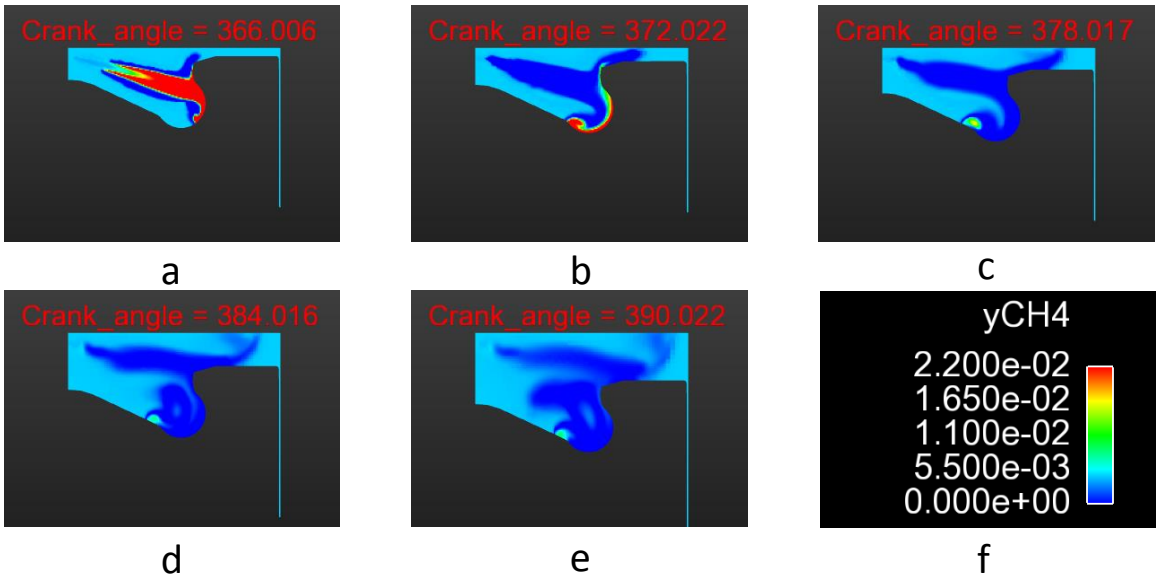

Figure 4.49 CH_4 evolution for BMEP=3.3 bar at 30 PES from (a) 366 CAD to (e) 390 CAD; (f) shows the scale for CH_4 in mass fraction

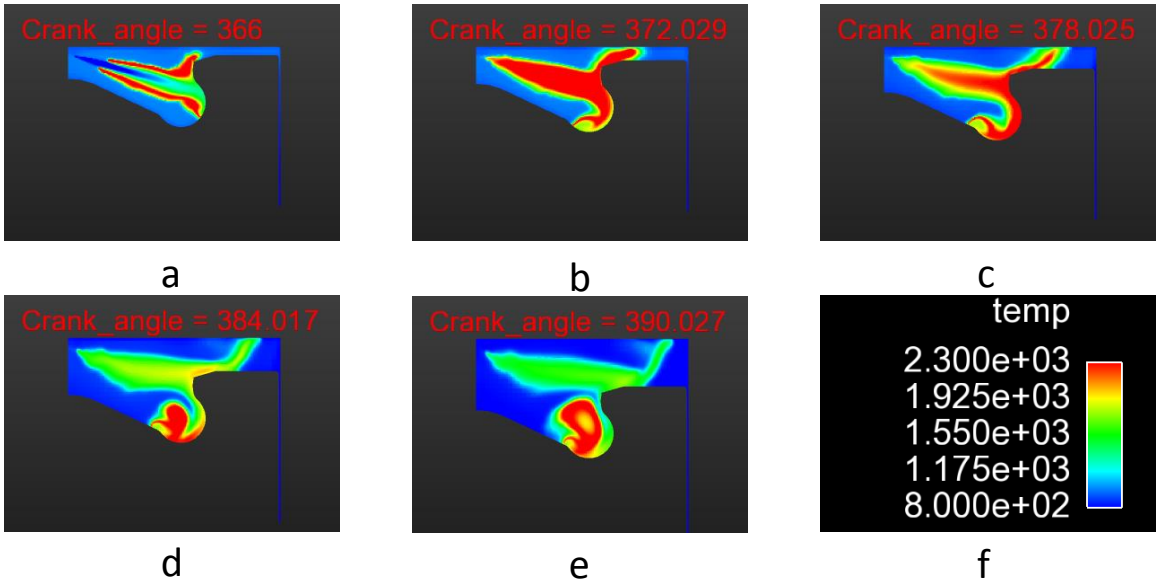

Figure 4.50 Local temperature evolution for BMEP=3.3 bar at 60 PES from (a) 366 CAD to (e) 390 CAD; (f) shows the scale for temperature in Kelvin.

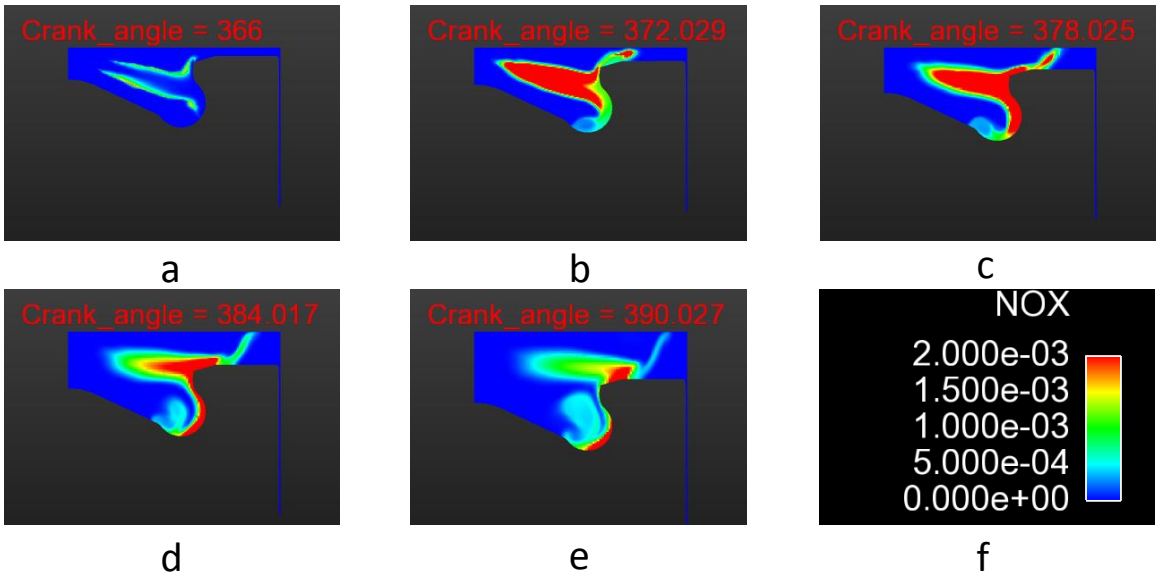

Figure 4.51 NOx evolution for BMEP=3.3 bar at 60 PES from (a) 366 CAD to (e) 390 CAD; (f) shows the scale for NOx in mass fraction

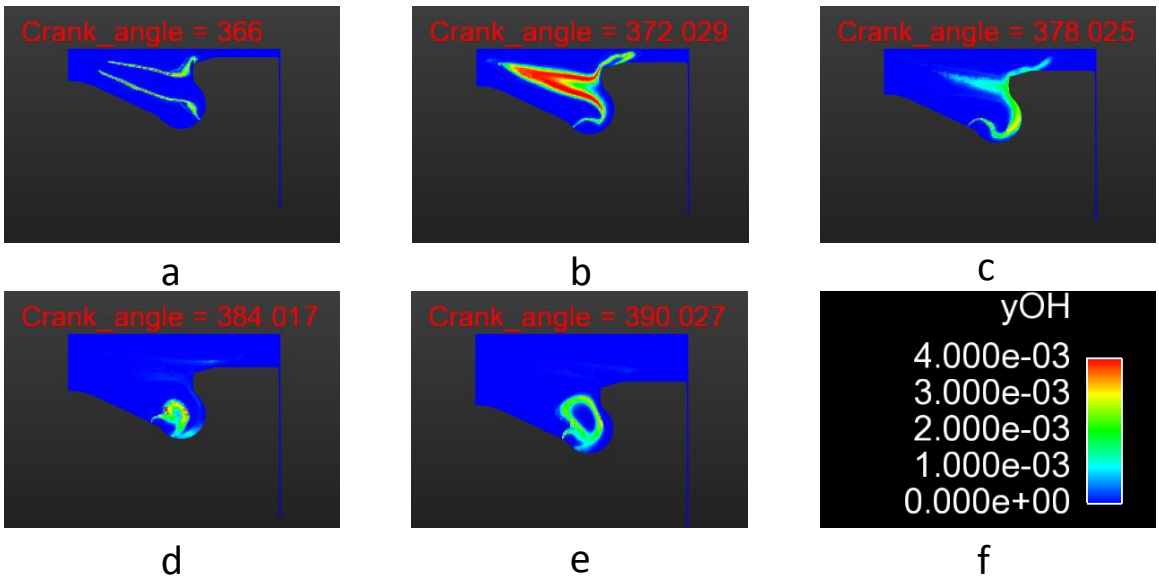

Figure 4.52 OH evolution for BMEP=3.3 bar at 60 PES from (a) 366 CAD to (e) 390 CAD; (f) shows the scale for OH in mass fraction

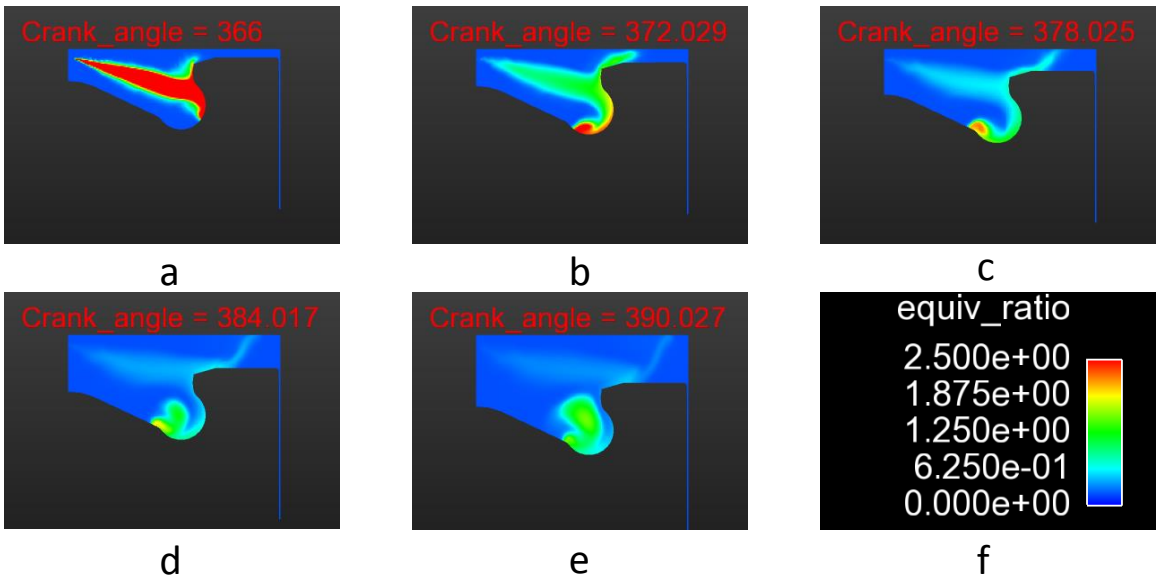

Figure 4.53 Equivalence ratio evolution for BMEP=3.3 bar at 60 PES from (a) 366 CAD to (e) 390 CAD; (f) shows the scale equivalence ratio

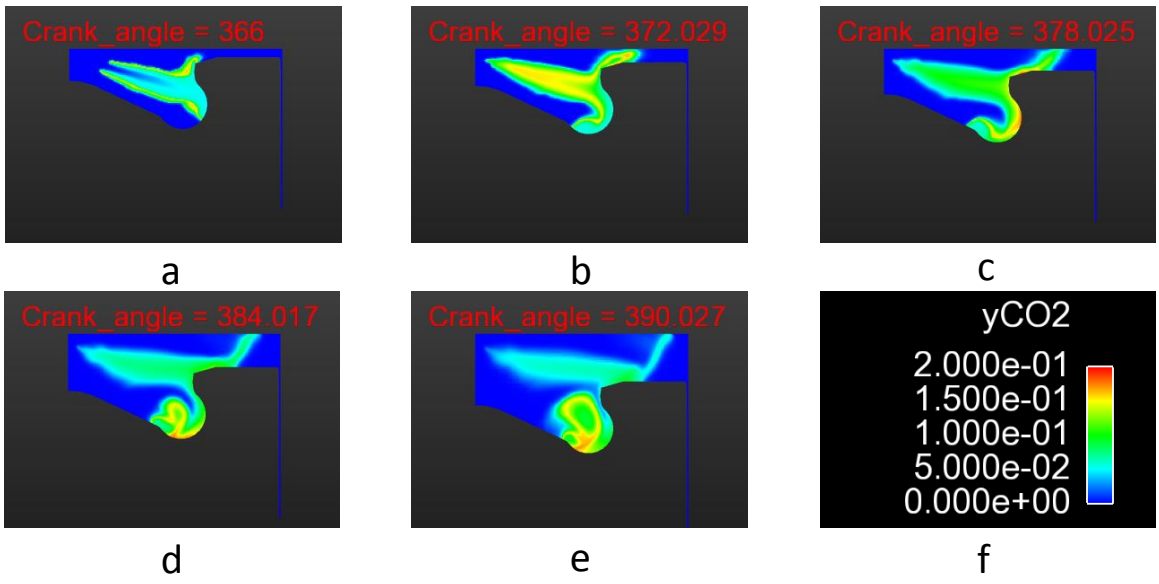

Figure 4.54 CO_2 evolution for BMEP=3.3 bar at 60 PES from (a) 366 CAD to (e) 390 CAD; (f) shows the scale for CO_2 in mass fraction

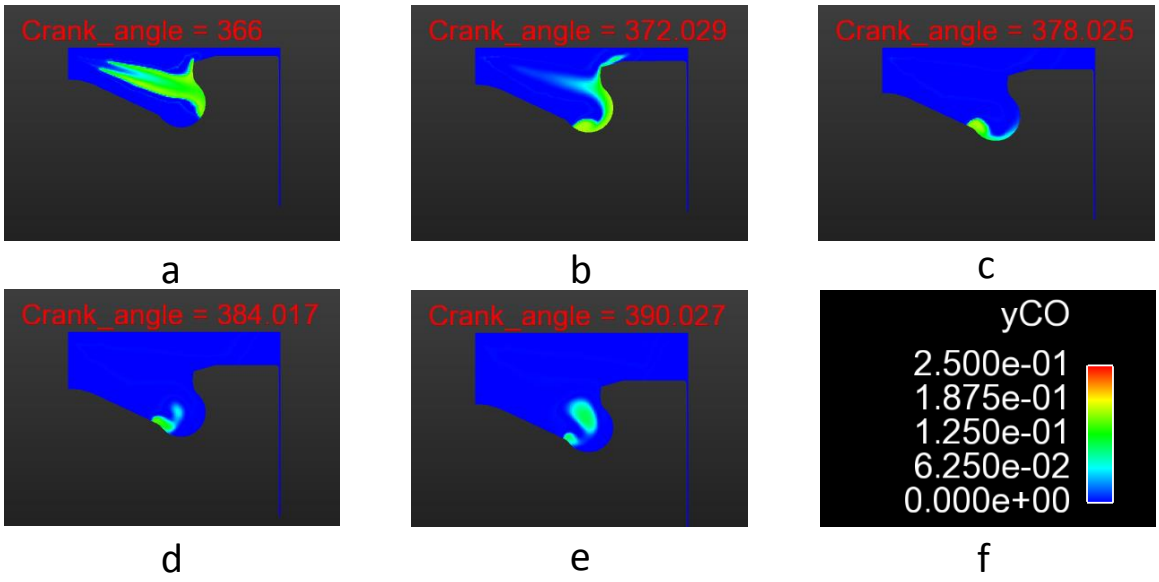

Figure 4.55 CO evolution for BMEP=3.3 bar at 30 PES from (a) 366 CAD to (e) 390 CAD; (f) shows the scale for CO in mass fraction

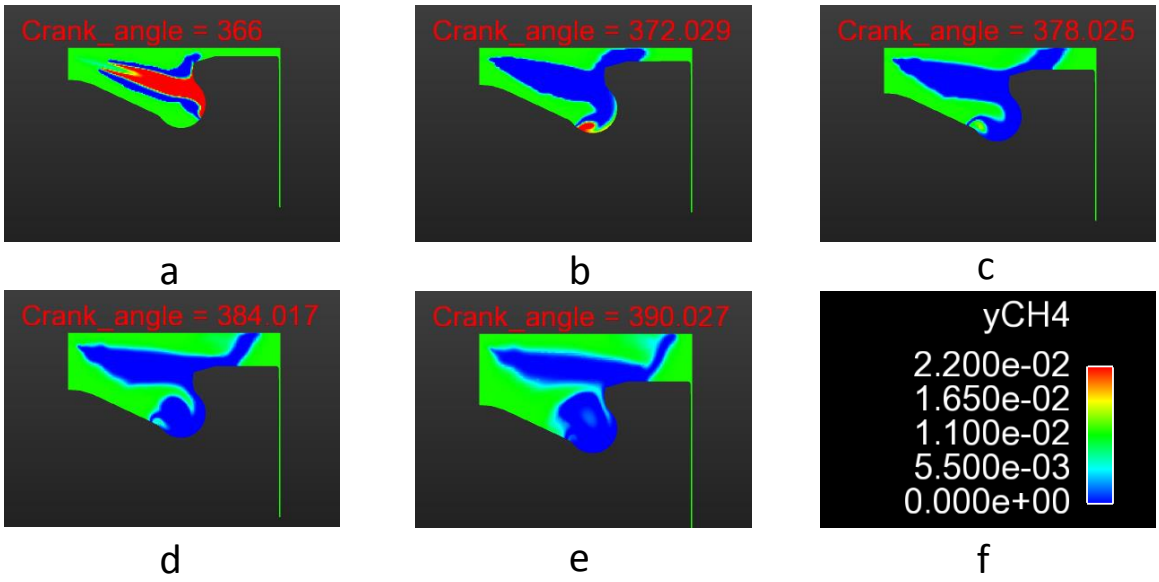

Figure 4.56 CH_4 evolution for BMEP=3.3 bar at 60 PES from (a) 366 CAD to (e) 390 CAD; (f) shows the scale for CH_4 in mass fraction

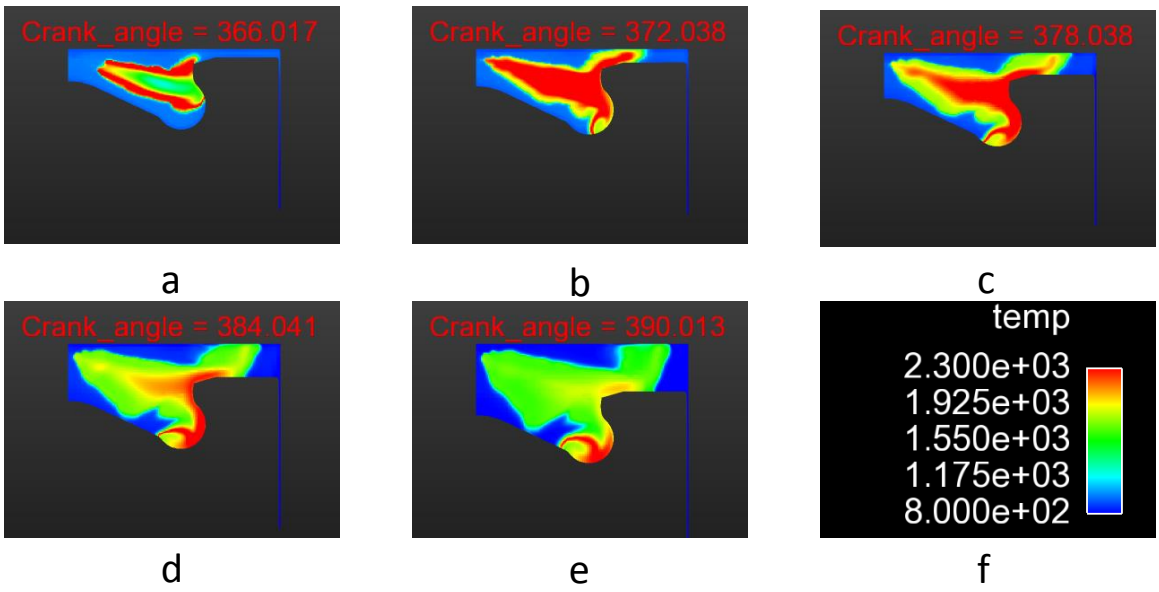

Figure 4.57 Local temperature evolution for BMEP=3.3 bar at 80 PES from (a) 366 CAD to (e) 390 CAD; (f) shows the scale for Temperature in Kelvin

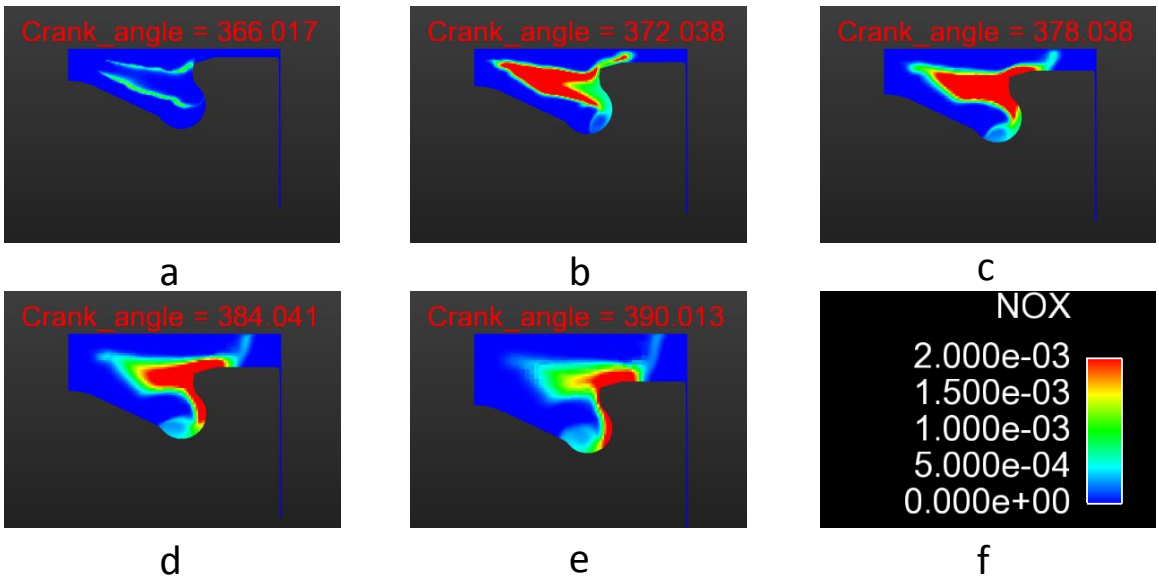

Figure 4.58 NOx evolution for BMEP=3.3 bar at 80 PES from (a) 366 CAD to (e) 390 CAD; (f) shows the scale for NOx in mass fraction

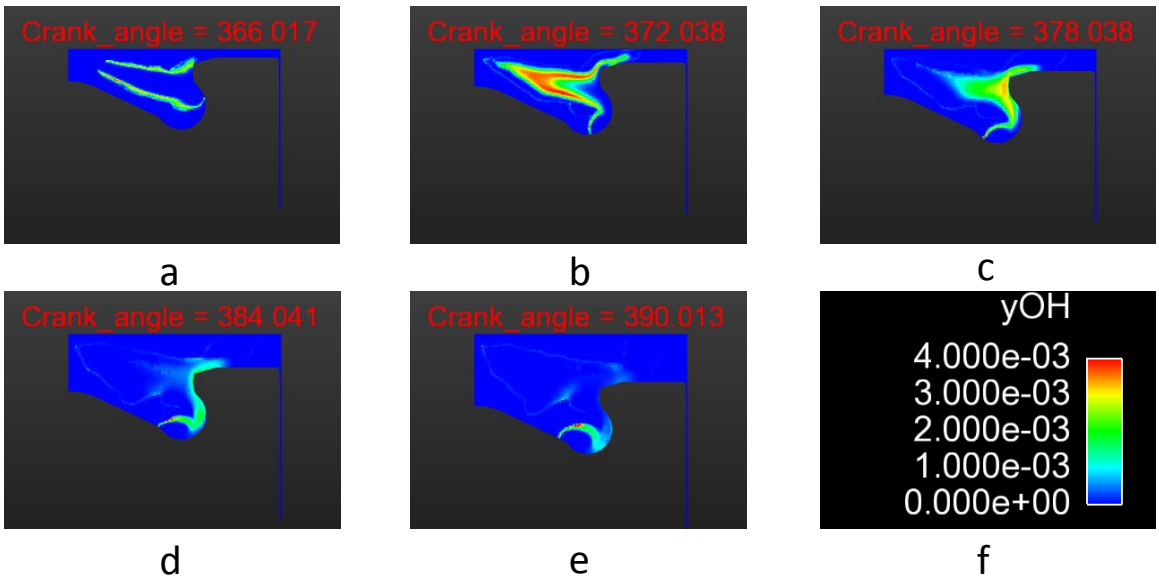

Figure 4.59 OH evolution for BMEP=3.3 bar at 80 PES from (a) 366 CAD to (e) 390 CAD; (f) shows the scale for OH in mass fraction

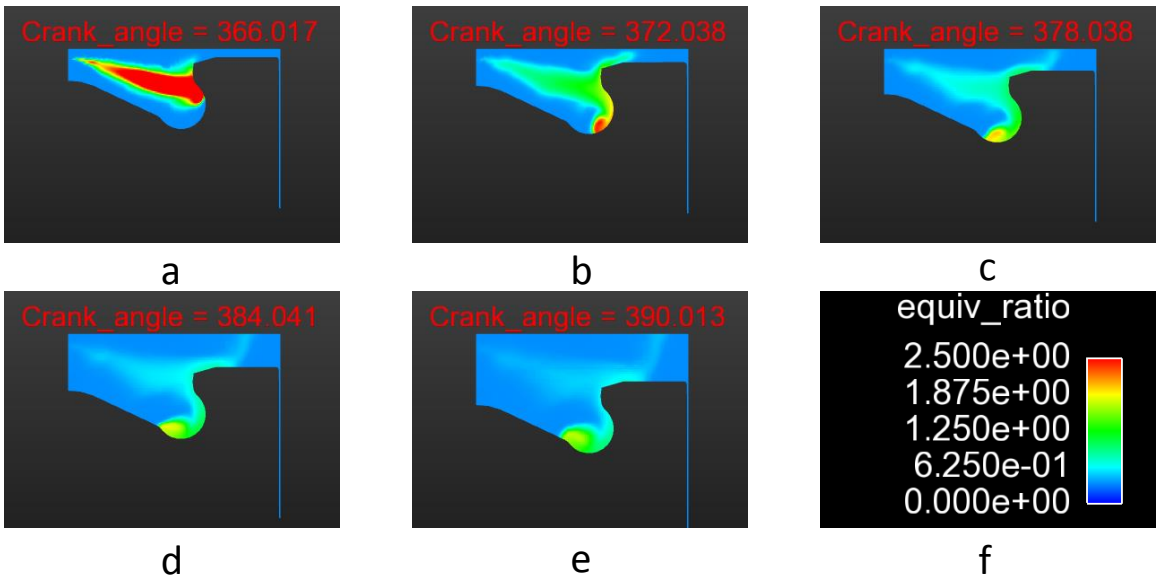

Figure 4.60 Equivalence ratio evolution for BMEP=3.3 bar at 80 PES from (a) 366 CAD to (e) 390 CAD; (f) shows the scale for equivalence ratio

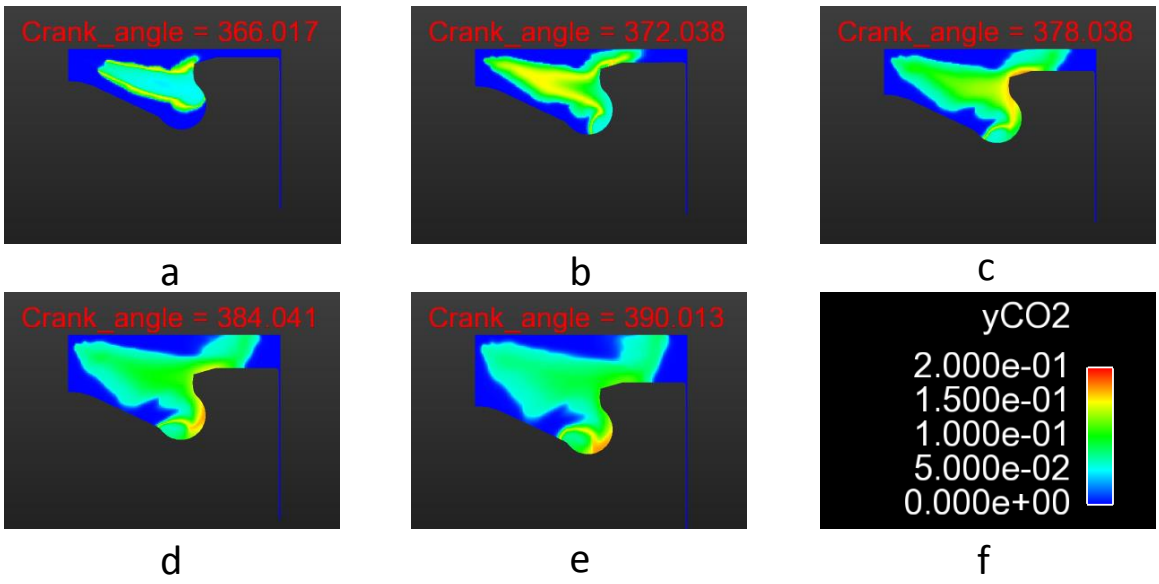

Figure 4.61 CO_2 evolution for BMEP=3.3 bar at 80 PES from (a) 366 CAD to (e) 390 CAD; (f) shows the scale for CO_2 in mass fraction

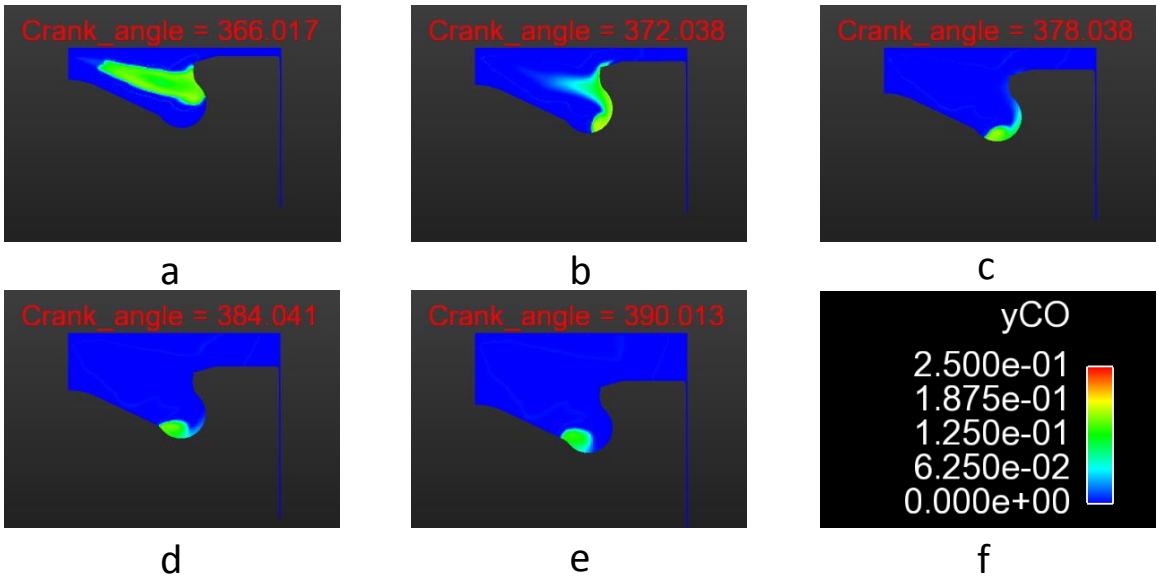

Figure 4.62 CO evolution for BMEP=3.3 bar at 80 PES from (a) 366 CAD to (e) 390 CAD; (f) shows the scale for CO in mass fraction

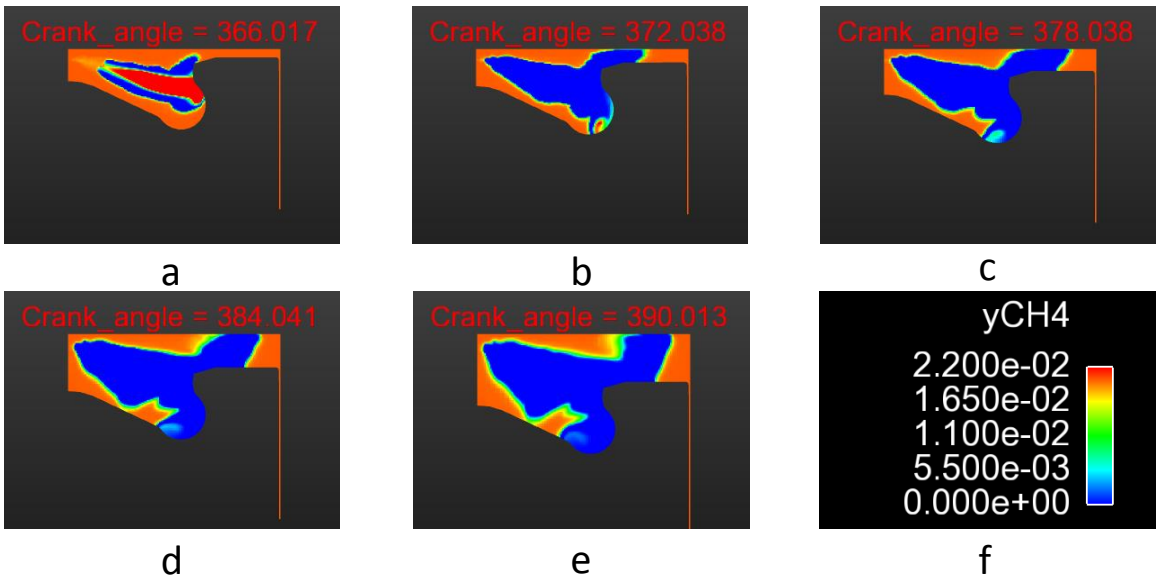

Figure 4.63 CH_4 evolution for BMEP=3.3 bar at 80 PES from (a) 366 CAD to (e) 390 CAD; (j) shows the scale for CH_4 in mass fraction

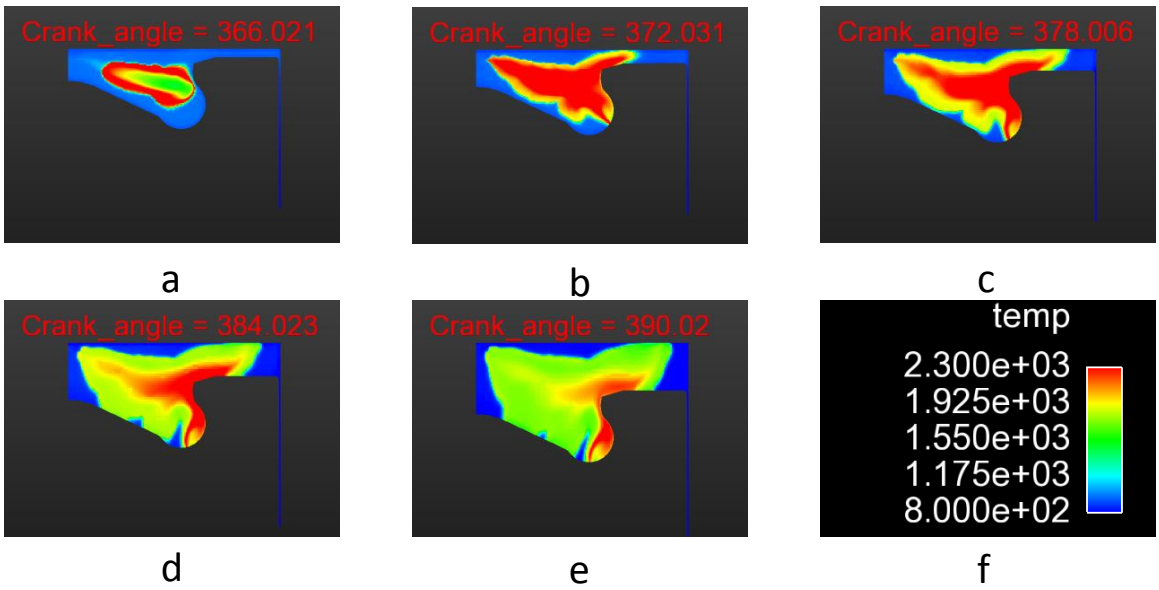

Figure 4.64 Local temperature evolution for BMEP=3.3 bar at 90 PES from (a) 366 CAD to (e) 390 CAD; (f) shows the scale for temperature in Kelvin

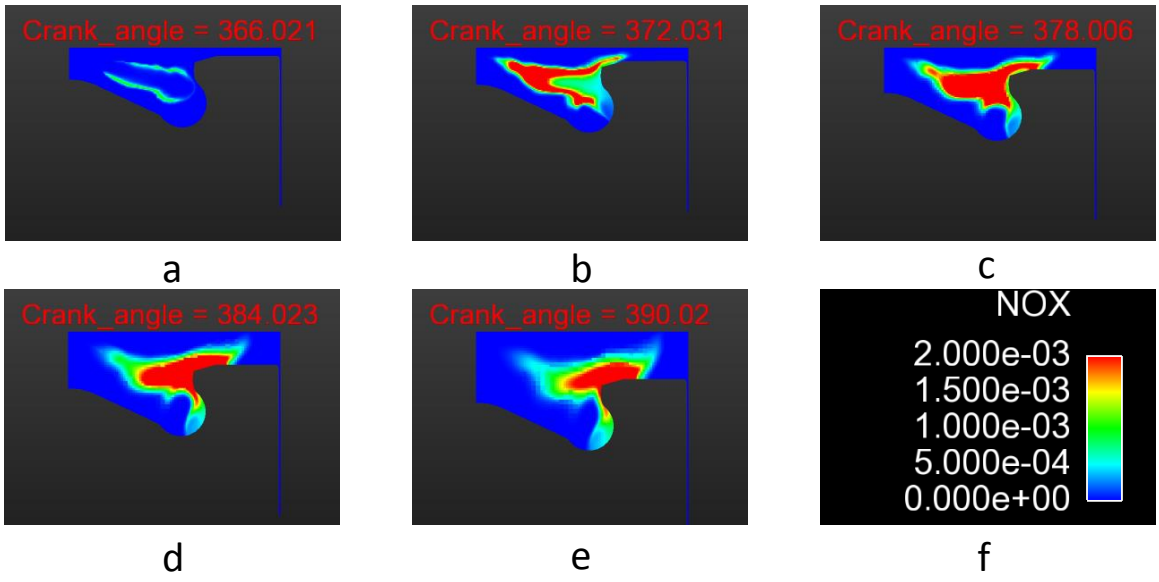

Figure 4.65 NOx evolution for BMEP=3.3 bar at 90 PES from (a) 366 CAD to (e) 390 CAD; (f) shows the scale for NOx in mass fraction

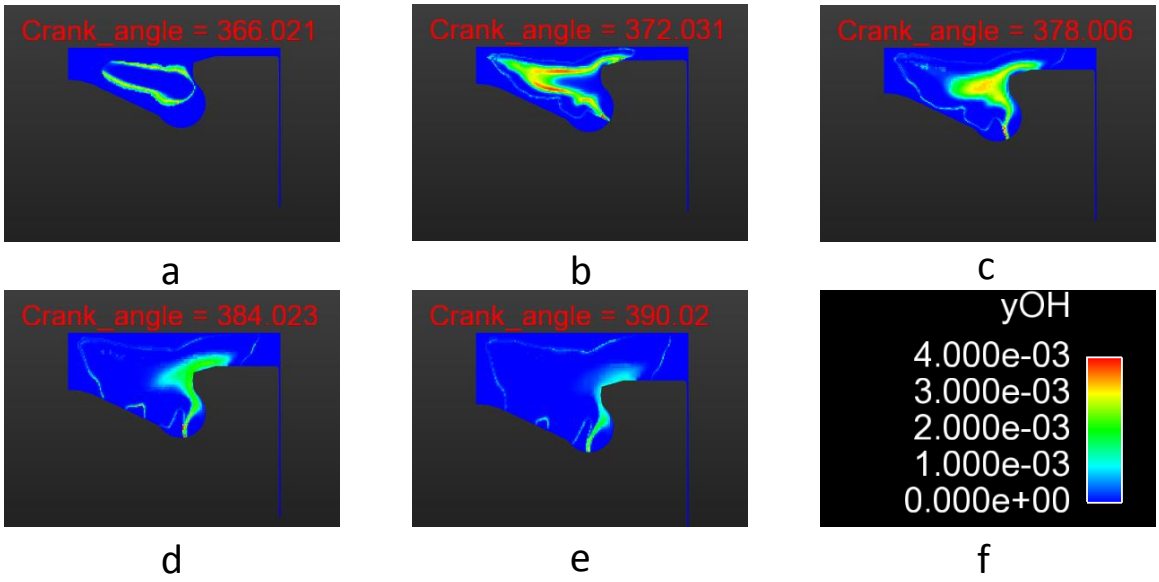

Figure 4.66 OH evolution for BMEP=3.3 bar at 90 PES from (a) 366 CAD to (e) 390 CAD; (f) shows the scale for OH in mass fraction

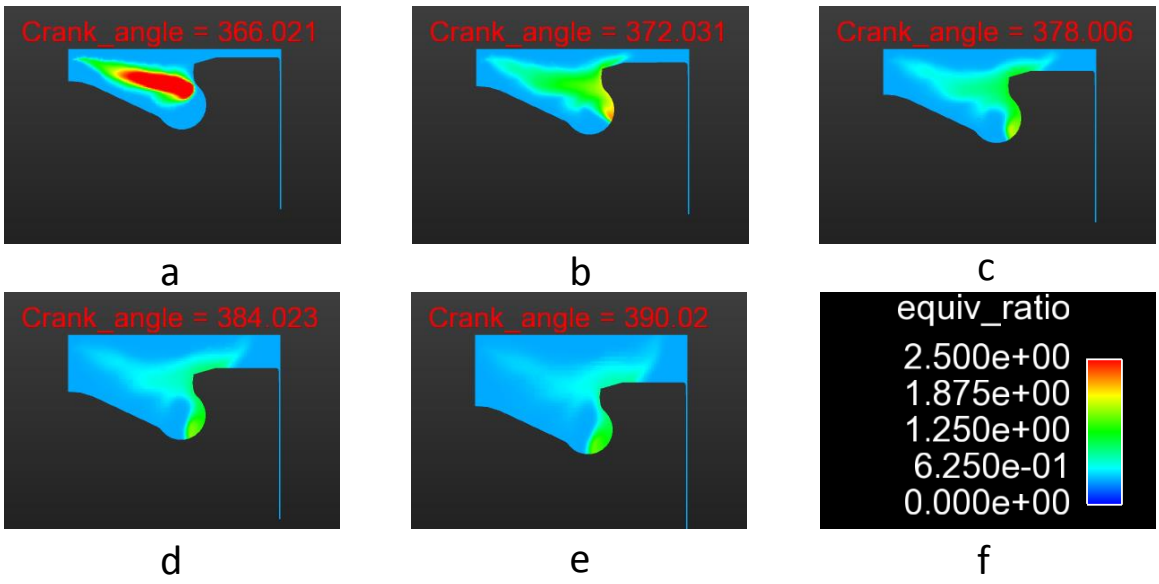

Figure 4.67 Equivalence ratio evolution for BMEP=3.3 bar at 90 PES from (a) 366 CAD to (e) 390 CAD; (f) shows the scale for equivalence ratio

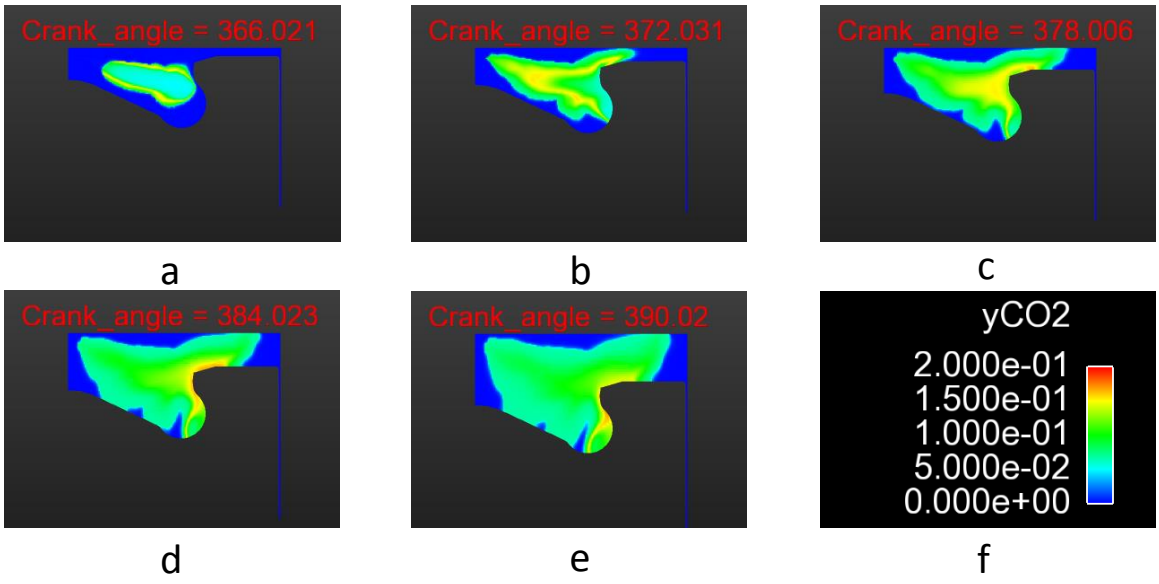

Figure 4.68 CO_2 evolution for BMEP=3.3 bar at 90 PES from (a) 366 CAD to (e) 390 CAD; (f) shows the scale for CO_2 in mass below

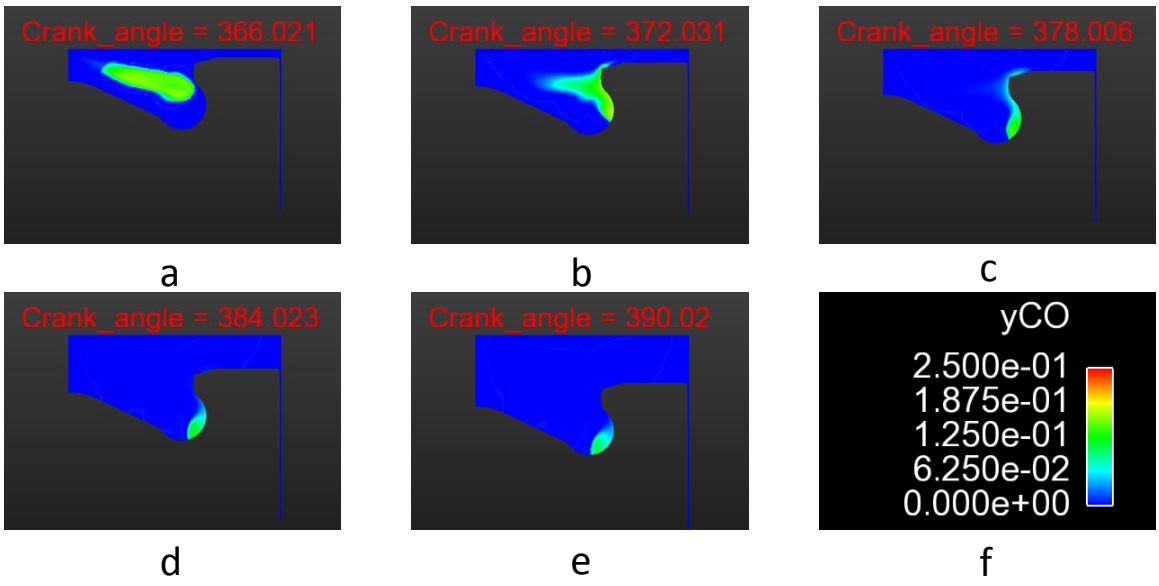

Figure 4.69 CO evolution for BMEP=3.3 bar at 90 PES from (a) 366 CAD to (e) 390 CAD; (f) shows the scale for CO in mass fraction

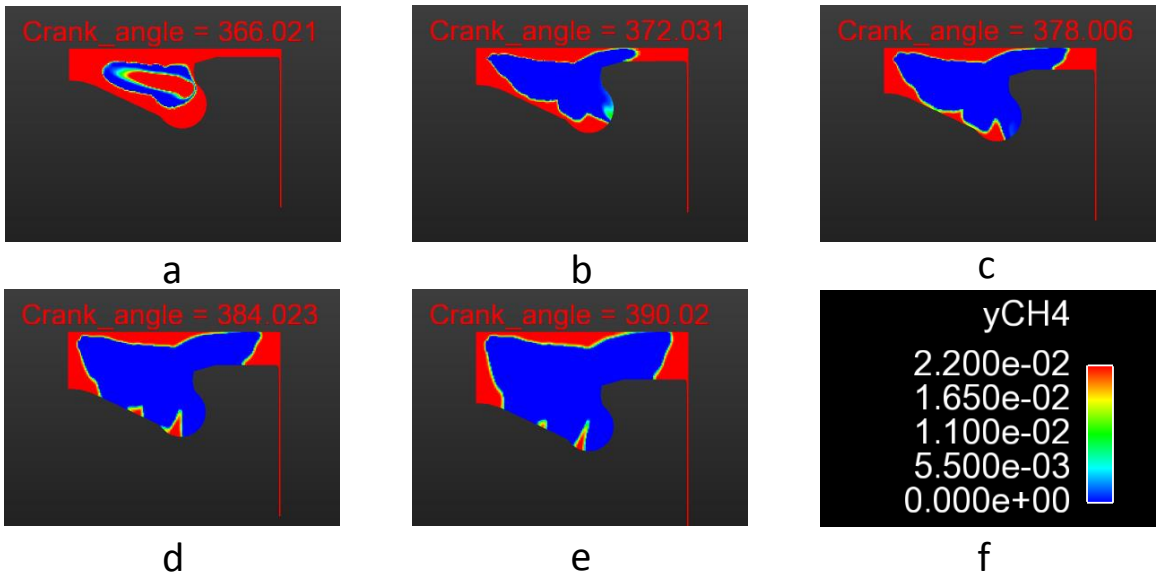

Figure 4.70 CH_4 evolution for BMEP=3.3 bar at 90 PES from (a) 366 CAD to (e) 390 CAD; (f) shows the scale for CH_4 in mass fraction

4.5 Parametric Study (swirl ratio sweep)

From results presented above for diesel-methane dual fuel combustion, it is evident that the overall combustion process is not spatially spread throughout the combustion chamber. For example, the methane-air mixture near the cylinder walls and the crevices remain unburned, leading to high HC emissions, especially at high PES. One way to enhance combustion inside cylinder is by increasing organized fluid motion, which in heavy-duty diesel engines might mean increased swirl. Swirl can be varied inside the cylinder by changing the shape of the intake manifold or the intake runner/port combination or by simply installing a swirl control valve just before the intake ports in a multi-intake valve engine configuration. Swirl is defined in terms of swirl ratio in IC engines. The swirl ratio is a dimensionless quantity, which Heywood [10] defines as the ratio of the angular velocity of a solid-body rotating flow ω (that is equal to the angular momentum of the actual fluid flow inside the cylinder) to the crankshaft rotational velocity. Six different swirl ratios (0, 0.3, 0.6, 0.9. 1.2, 1.5) are selected for this parametric study at 80 PES and 3.3 bar BMEP; other initial, boundary, and operating conditions are listed in Table 4.4. All other operating conditions (not mentioned in Table 4.4.) are kept similar to the dual fuel simulations discussed in Section 4.4.

Table 4.4 Swirl ratio sweep of diesel-methane dual fuel combustion at 3.3 bar BMEP and 80 PES

Swirl ratio	PIVC (bar)	TIVC (K)	Diesel injected (kg/cycle/cyl)	Methane injected (kg/cycle/cyl)	Cylinder head Temp.(K)	Liner Temp. (K)	Piston Temp. (K)
0	1.61	367	1.5E-05	5.7E-05	430	410	470
0.3	1.61	367	1.5E-05	5.7E-05	430	410	470
0.6	1.61	367	1.5E-05	5.7E-05	430	410	470
0.9	1.61	367	1.5E-05	5.7E-05	430	410	470
1.2	1.61	367	1.5E-05	5.7E-05	430	410	470
1.5	1.61	367	1.5E-05	5.7E-05	430	410	470

In-cylinder pressure, AHRR, ISNOx, ISCO, ISHC, CA50 and indicated mean effective pressure (IMEP) are plotted respectively from Figure 4.71 to Figure 4.77 for different swirl ratio cases. Comparison plots of local temperature, NOx, OH, equivalence ratioCO_2, CO and CH_4 for three different swirl ratios of 0, 0.6 and 1.5 are shown from Figure 4.78 to Figure 4.84. The color maps are presented in a section (i.e., XZ plane) that was obtained by cutting the computational domain (viewing from the top) in the middle of the sector along the cylinder axis.

It can be observed from Figure 4.71 and Figure 4.72 that with increasing swirl ratio, the peak pressure and second stage of AHRR increase. On the other hand, the onset of ignition is not affected significantly by the swirl ratio while the first stage of AHRR is actually decreased. These trends can be explained based on the fact that increasing swirl ratio tends to provide a better distribution of the fuel-air mixture throughout the combustion chamber and enhances combustion rates. Consequently, the peak pressures and the second stage of AHRR are increased with increasing swirl ratio. However, swirl does not seem to affect the onset of ignition as much, likely due to the increased importance of the spray breakup, droplet evaporation, and chemical kinetic mechanism in

controlling preignition reactions. The faster burn rates are also evident from the combustion phasing (CA50) trend shown in Figure 4.76. Combustion phasing shows a slight advancement (toward TDC) with increasing swirl ratio. Swirl also promotes the combustion of a higher fraction of the trapped charge, increasing the IMEP of the engine as shown in Figure 4.77. This can also be confirmed as cumulative heat release increases from 2028 J at 0 swirl ratio to 2425 J at 0.6 swirl ratio to 2629 at swirl ratio of 1.5. Emission trends are affected more significantly with increasing swirl. Better mixing at higher swirl ratios and faster burn rates increase local temperatures inside the cylinder, resulting in higher ISNOx emissions at high swirl ratios. The ISNOx trend shows a slight decrease up to a swirl ratio of 0.3 (since the IMEP increase outweighed the NOx mass increase up to this swirl ratio) and subsequently increases for higher swirl ratios as shown in Figure 4.73. On the other hand, both ISHC and ISCO decrease significantly with increasing swirl ratio as shown in Figures 4.74 and 4.75, respectively. This may be explained based on the enhanced combustion rates, which cause higher local temperatures inside the cylinder, improving both HC and CO oxidation rates. It is important to remember that most of the HC emissions in diesel-methane dual fuel combustion arise from unburned methane near the cylinder walls and within the crevices. With increasing swirl ratio, mixing inside the cylinder increases and this promotes a more efficient and effective combustion of the unburned methane, reducing the engine-out HC emissions. From the temperature color maps shown in Figure 4.78, it is evident that with increasing swirl ratio, the high temperature regions are better distributed spatially inside the cylinder, leading to the combustion of previously unburned methane at low swirl conditions. This can also be seen from the equivalence ratio color maps shown in Figure

4.81. It must also be noted that with increasing swirl ratio, the out-of-plane velocities are increased and the spray moves out of the XZ sectional plane, which causes better mixing of the diesel fuel with the surrounding methane-air mixture and a better spread of combustion around the cylinder. Similarly, the presence of CO_2 is a strong indication of the local completeness of the combustion process. With increasing swirl ratio, higher CO_2 concentrations are observed throughout the sectional XY plane, as seen in Figure 4.82. These CO_2 trends are also accompanied by evidence of better (more complete) CO oxidation with increasing swirl ratio as shown in Figure4.83; as explained before, the higher CO oxidation rates may be attributed to enhanced combustion rates and the associated increase in cylinder temperatures. The ISHC trends are also corroborated by the methane mass fraction color maps shown in Figure 4.84. With increasing swirl ratio, methane combustion is improved, and therefore, the methane mass fractions near the cylinder walls and the cylinder head are reduced, thereby reducing ISHC emissions. It is important note, however, that increasing swirl ratio does not appear to substantially reduce the methane originating from the piston top-land crevice and from near the fuel injector nozzle.

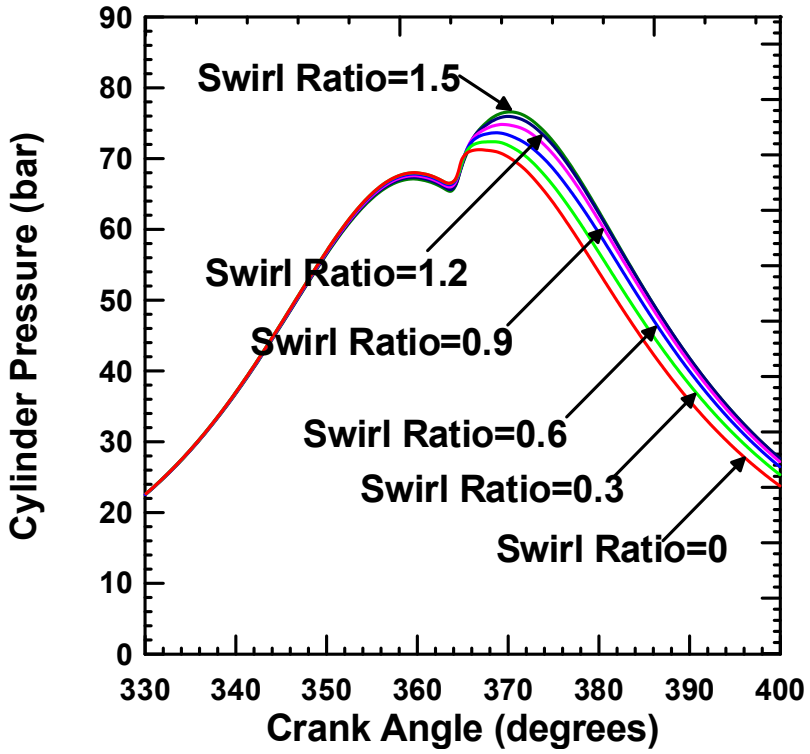

Figure 4.71 Pressure plots for 80 % methane PES at BMEP=3.3 bar from swirl 0 to 1.5

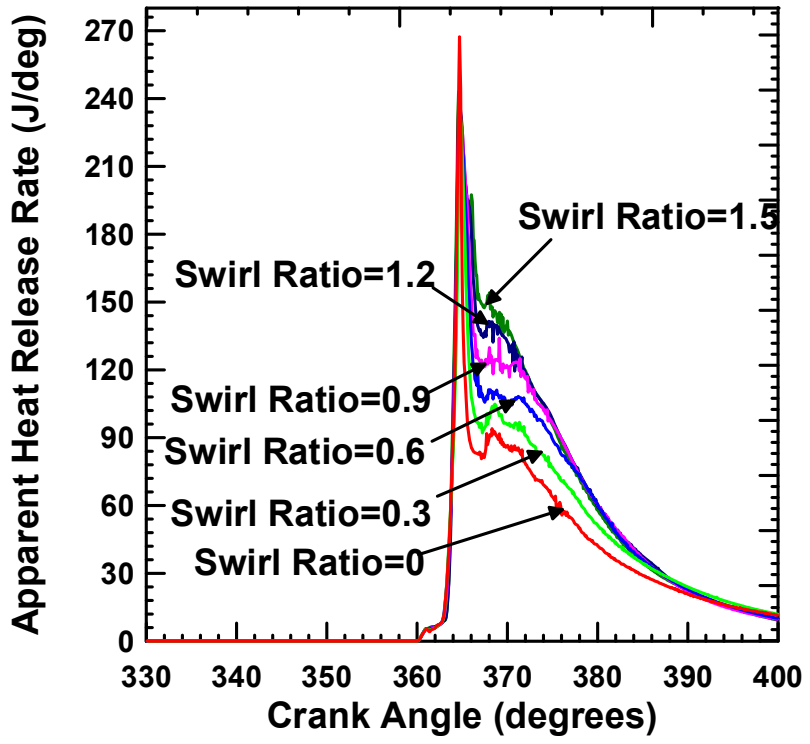

Figure 4.72 AHRR plot for 80 % methane PES at BMEP=3.3 bar from swirl 0 to 1.5

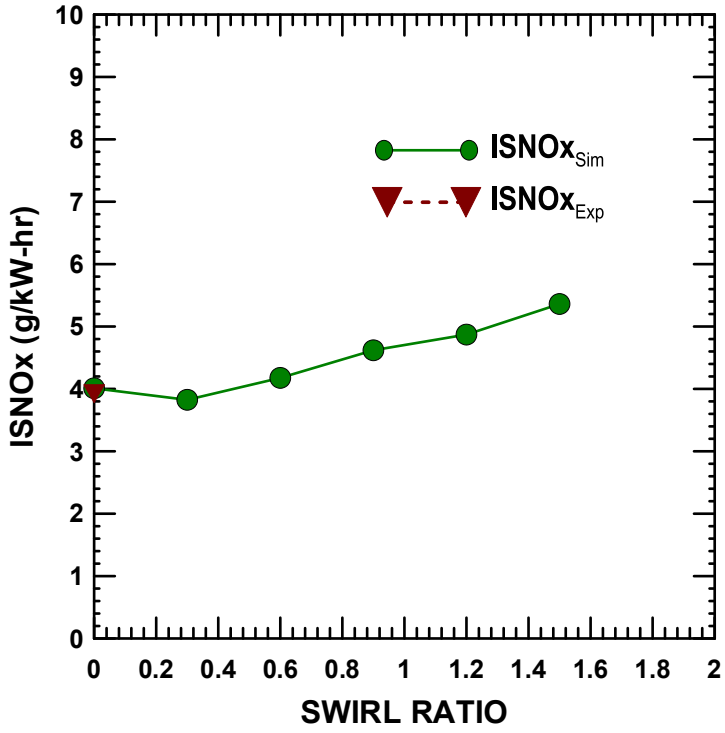

Figure 4.73 ISNOx plot for 80 % methane PES at BMEP=3.3 bar from swirl 0 to 1.5

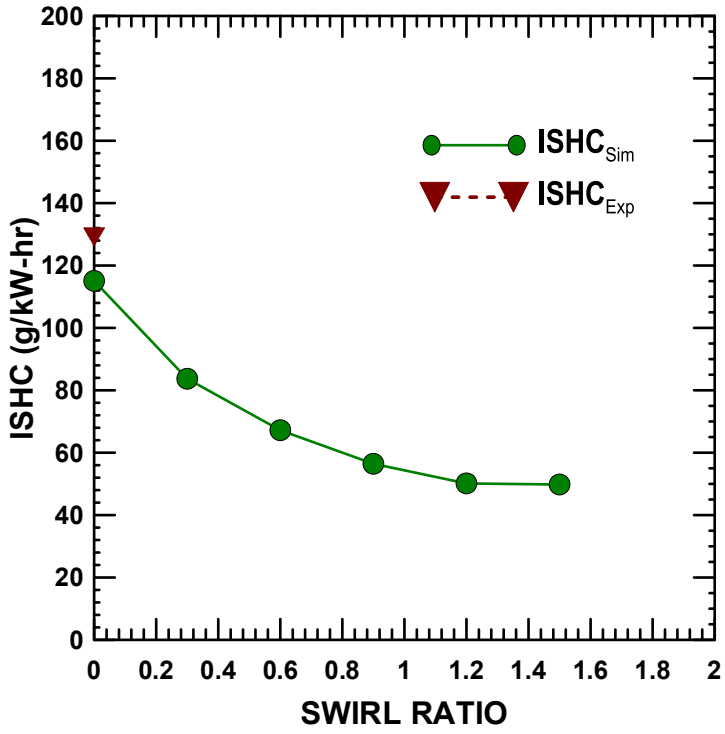

Figure 4.74 ISHC plot for 80 % methane PES at BMEP=3.3 bar from swirl 0 to 1.5

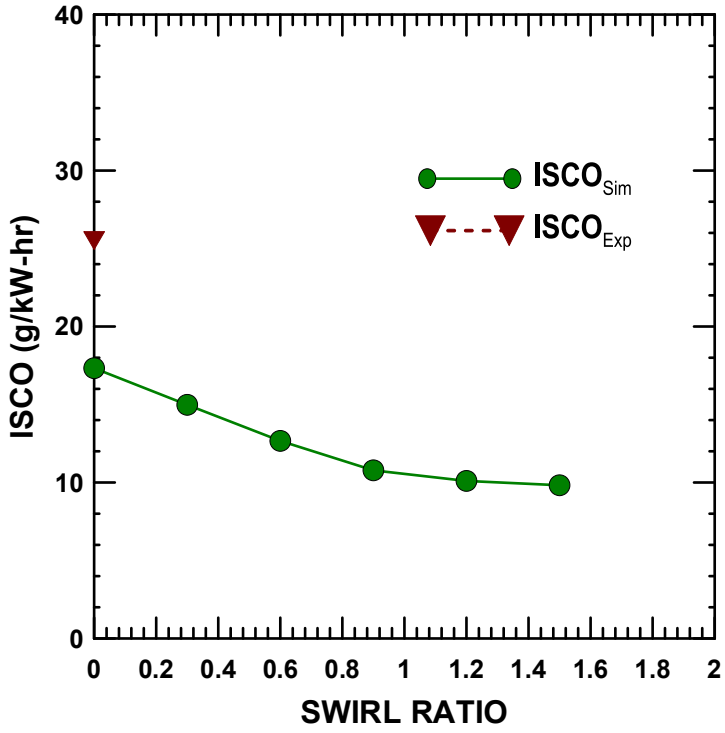

Figure 4.75 ISCO plot for 80 % methane PES at BMEP=3.3 bar from swirl 0 to 1.5

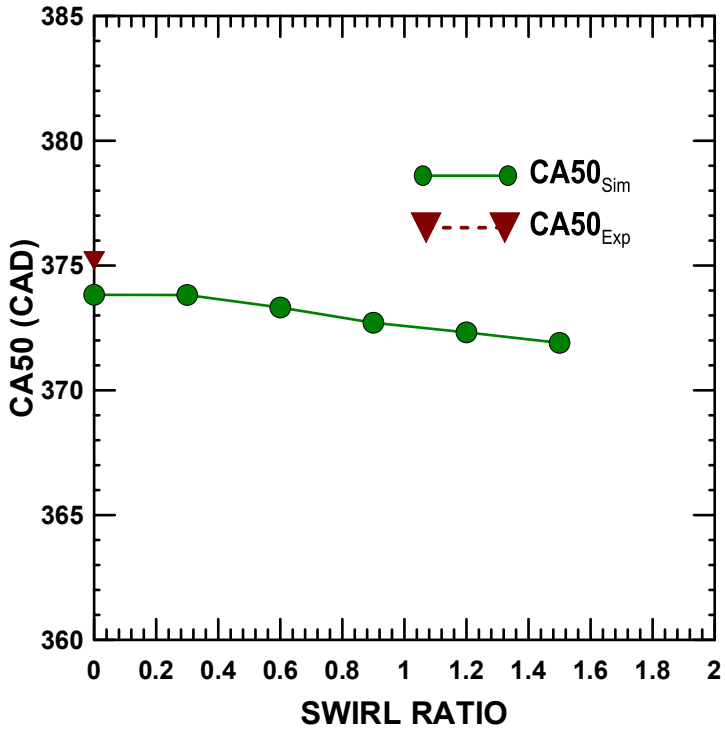

Figure 4.76 CA50 plot for 80 % methane PES at BMEP=3.3 bar from swirl 0 to 1.5

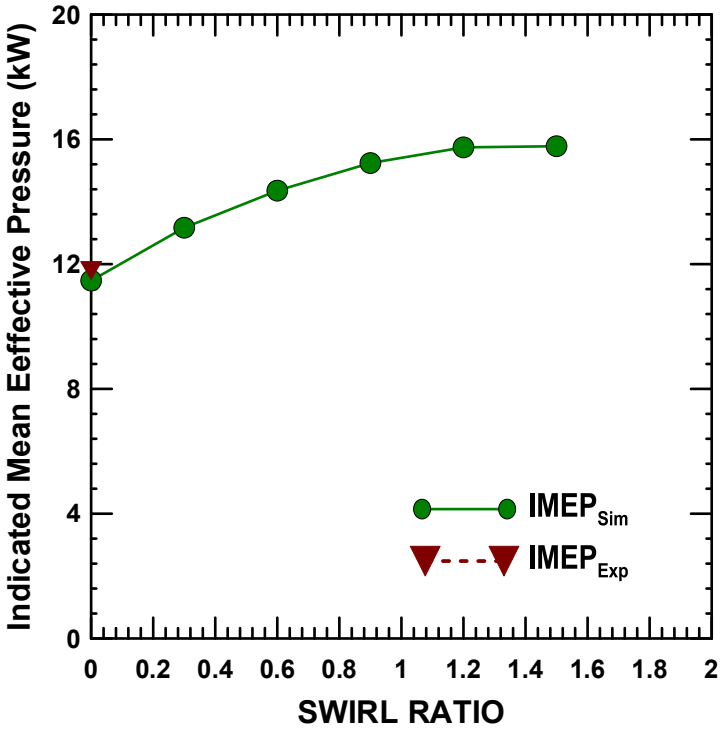

Figure 4.77 IMEP plot for 80 % methane PES at BMEP=3.3 bar from swirl 0 to 1.5

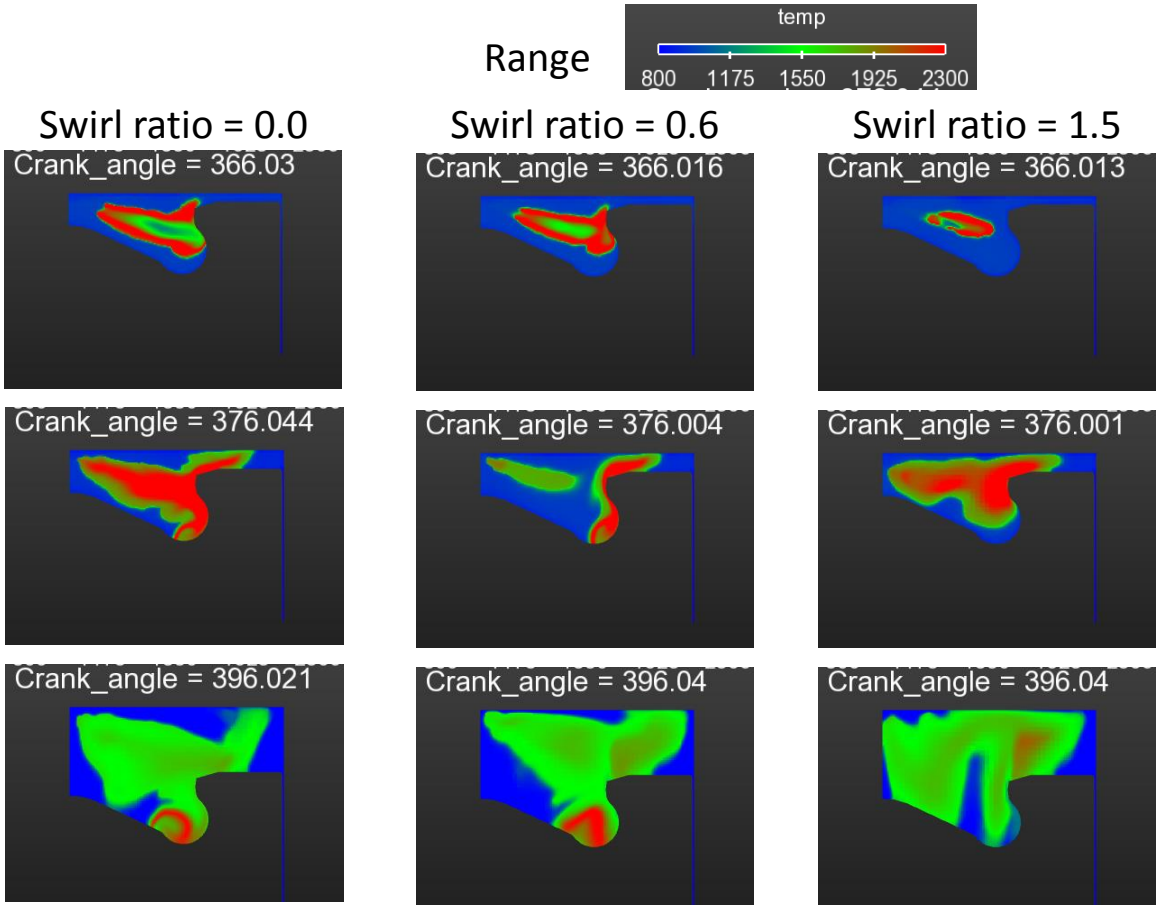

Figure 4.78 Comparison of temperature distribution inside cylinder at BMEP=3.3 bar for PES 80% for swirl ratio 0.0, 0.6 and 1.5 from left to right at three different crank angle of 366, 376, 396 in Kelvin.

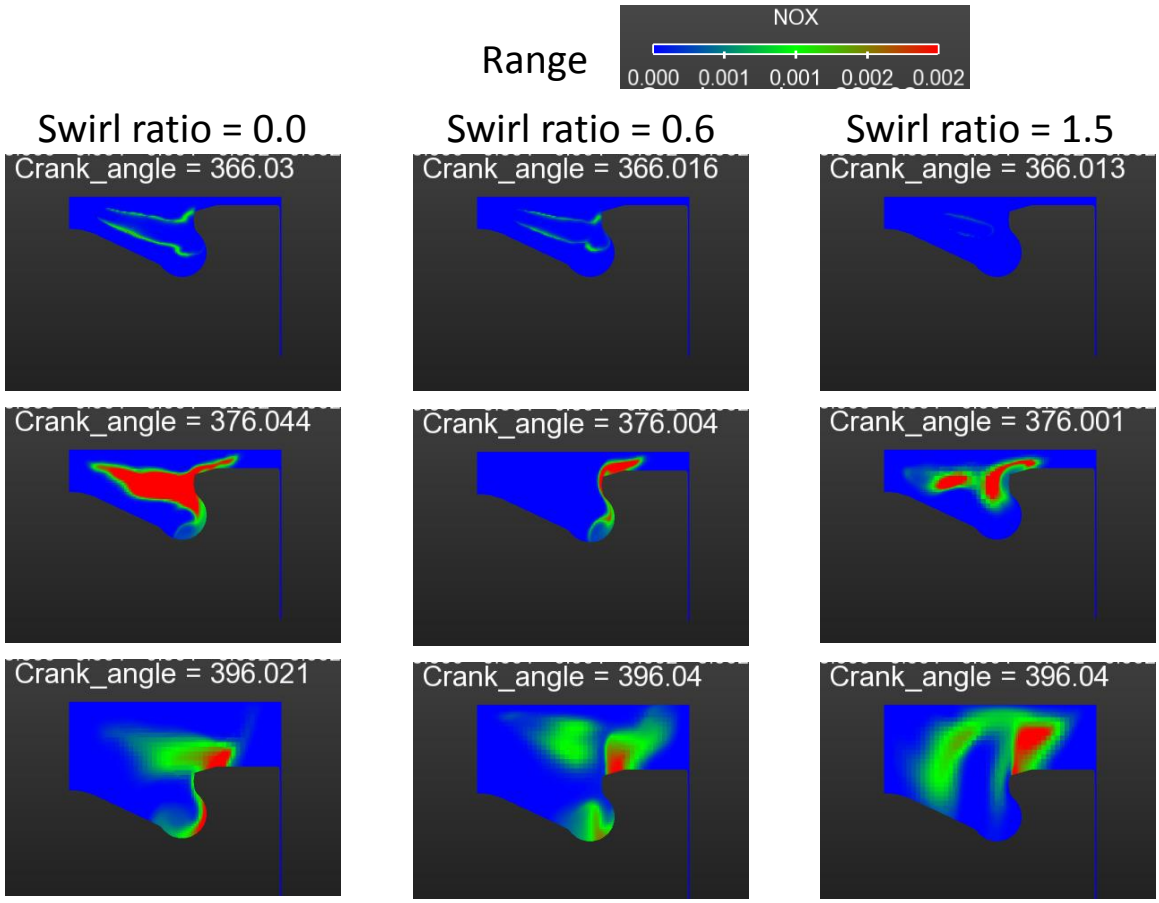

Figure 4.79 Comparison of NOX distribution inside cylinder at BMEP=3.3 bar for PES 80% for swirl ratio 0.0, 0.6 and 1.5 from left to right at three different crank angle of 366, 376, 396 in mass fraction.

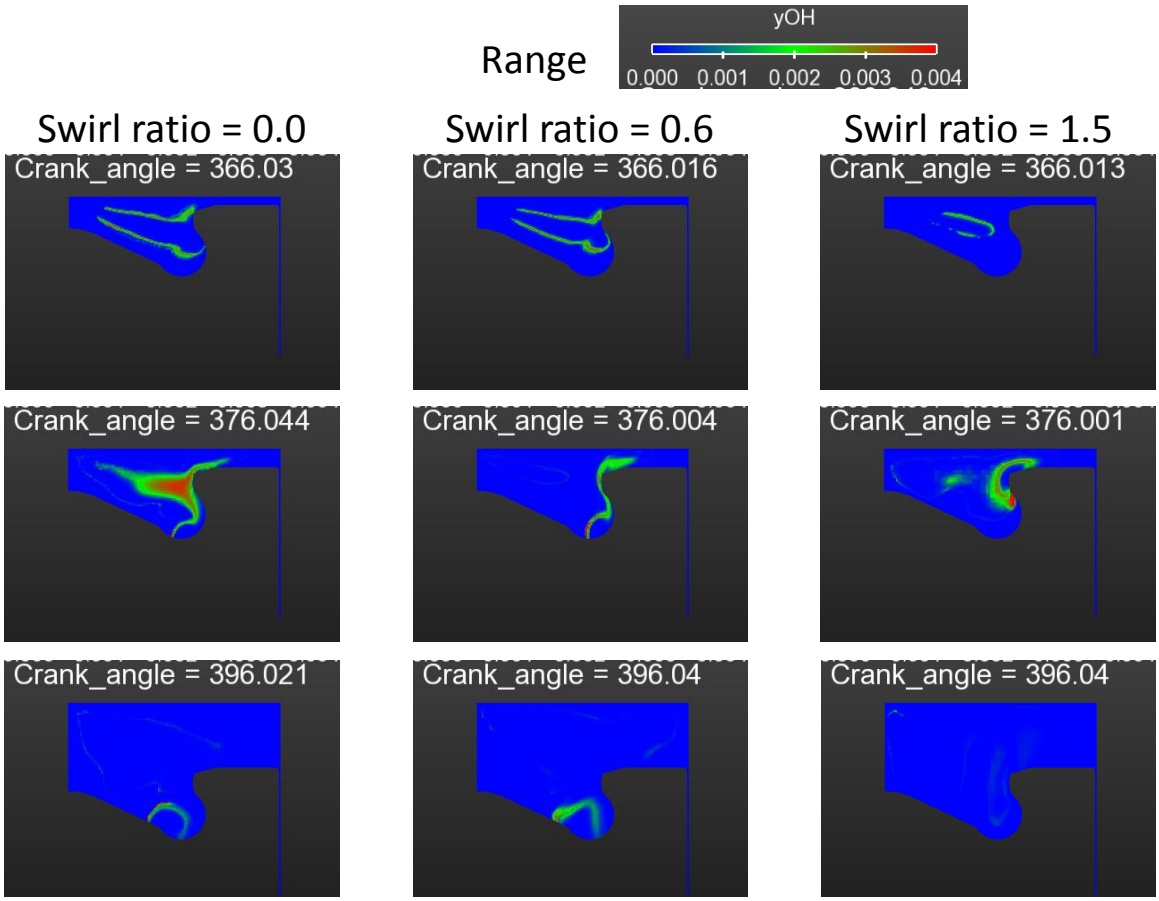

Figure 4.80 Comparison of OH distribution inside cylinder at BMEP=3.3 bar for PES 80% for swirl ratio 0.0, 0.6 and 1.5 from left to right at three different crank angle of 366, 376, 396 in mass fraction.

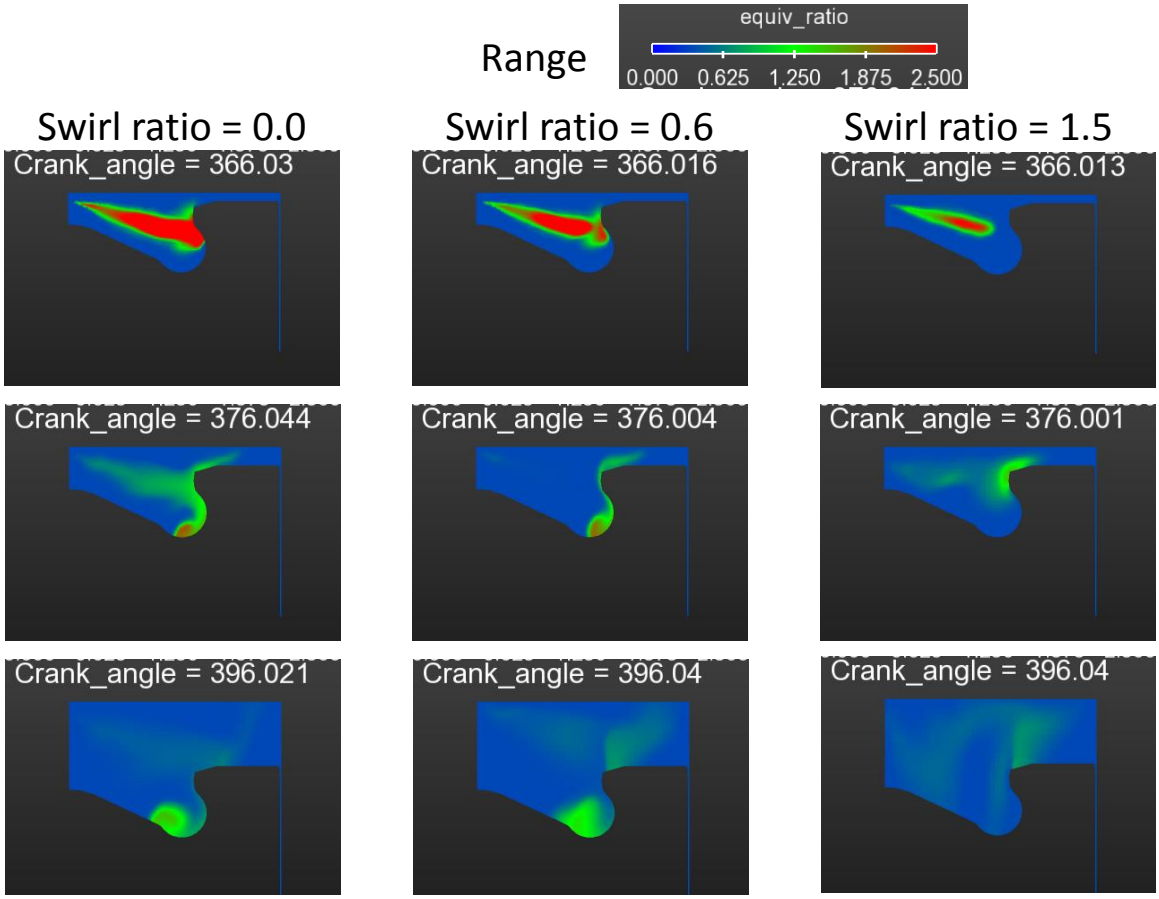

Figure 4.81 Comparison of equivalence ratio distribution inside cylinder at BMEP=3.3 bar for PES 80% for swirl ratio 0.0, 0.6 and 1.5 from left to right at three different crank angle of 366, 376, 396 in.

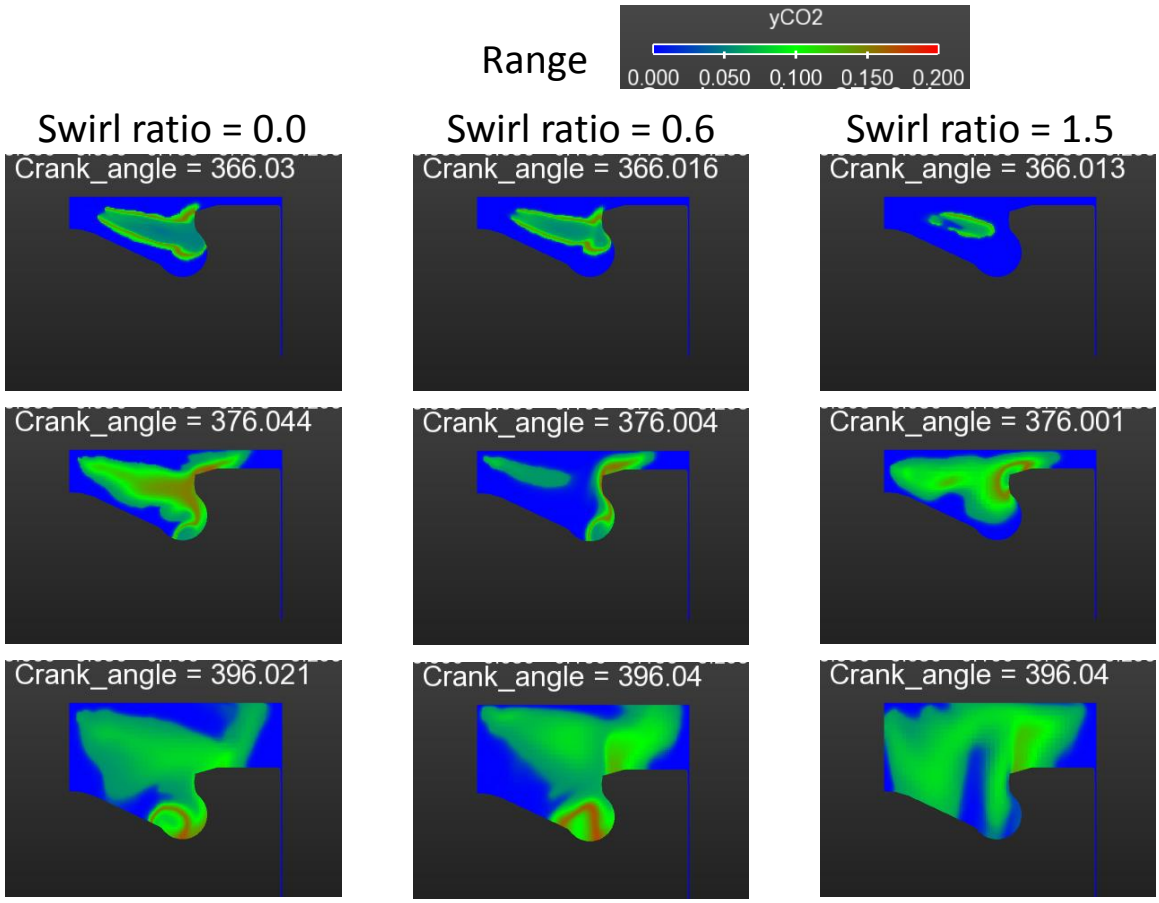

Figure 4.82 Comparison of CO_2 distribution inside cylinder at BMEP=3.3 bar for PES 80% for swirl ratio 0.0, 0.6 and 1.5 from left to right at three different crank angle of 366, 376, 396 in mass fraction.

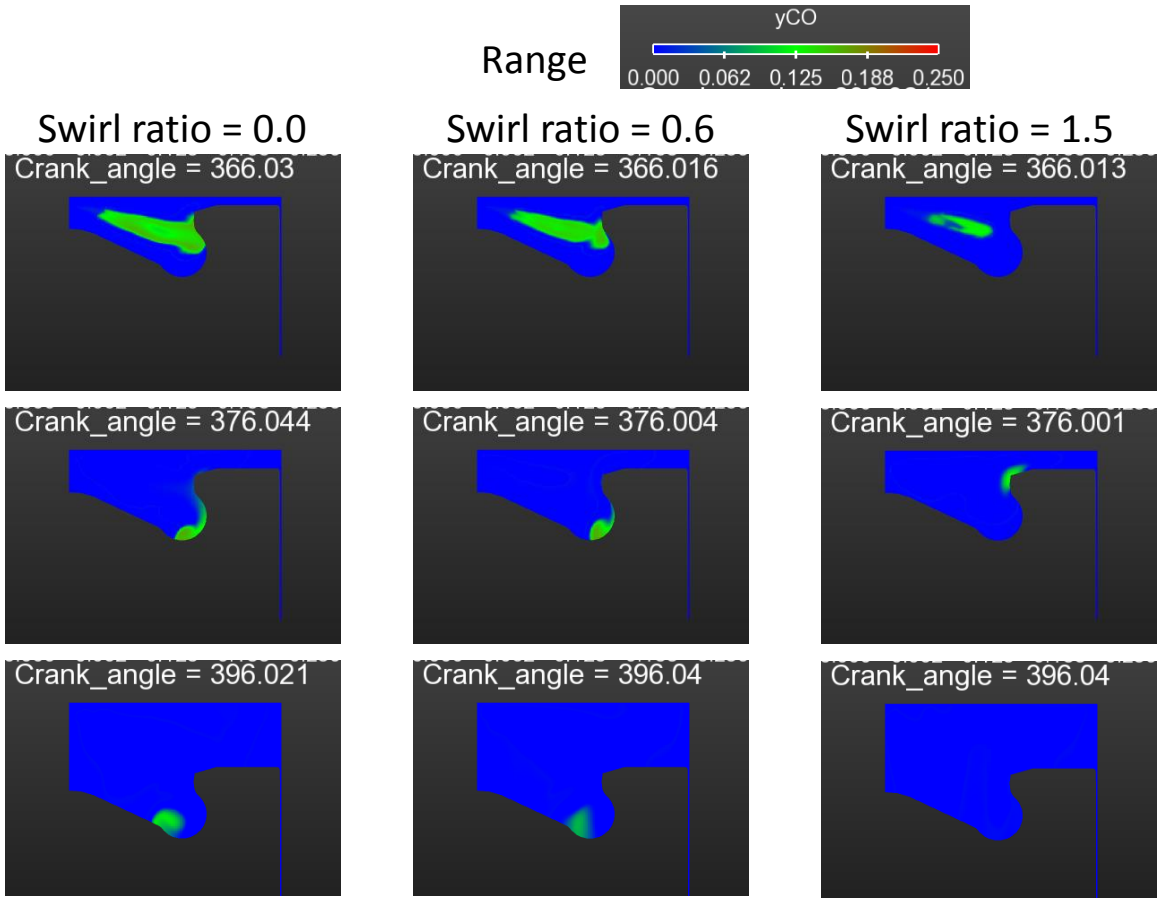

Figure 4.83 Comparison of CO distribution inside cylinder at BMEP=3.3 bar for PES 80% for swirl ratio 0.0, 0.6 and 1.5 from left to right at three different crank angle of 366, 376, 396 in mass fraction.

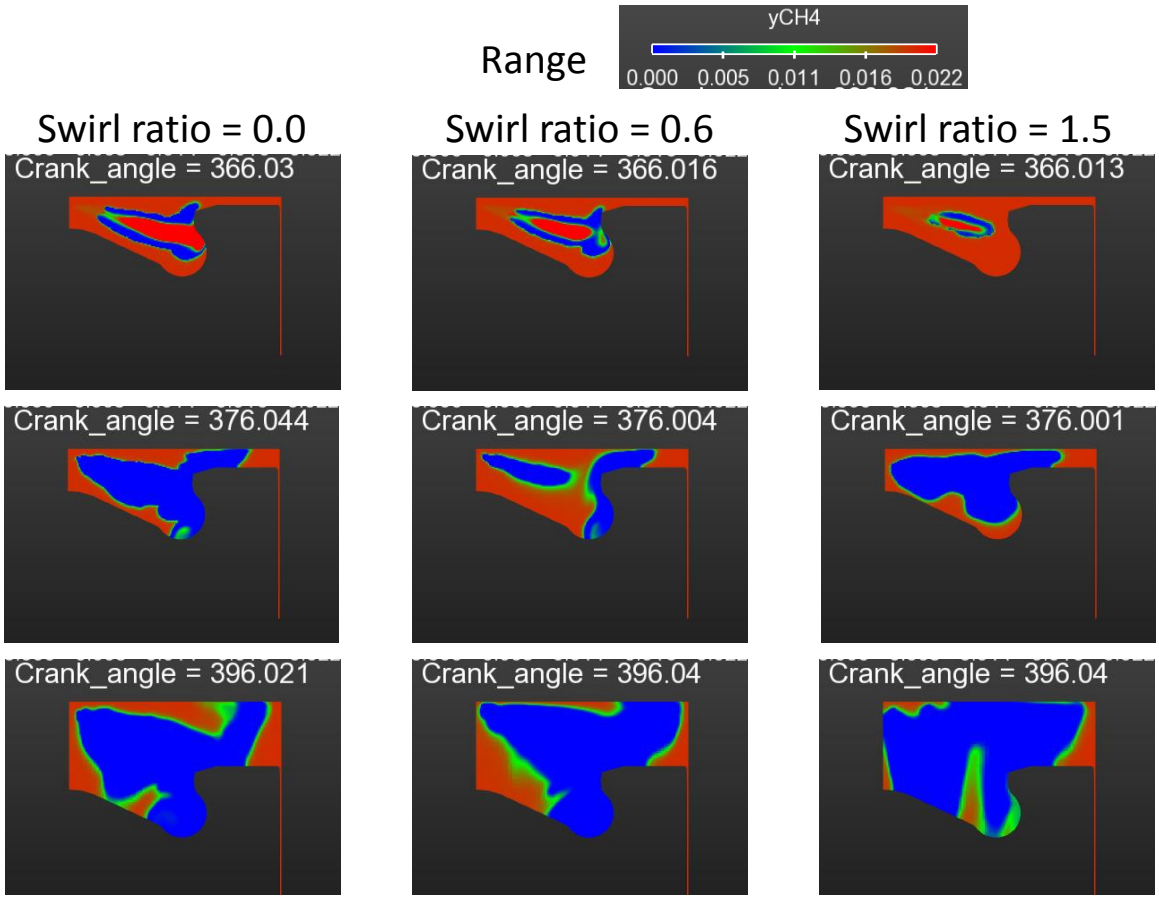

Figure 4.84 Comparison of CH_4 distribution inside cylinder at BMEP=3.3 bar for PES 80% for swirl ratio 0.0, 0.6 and 1.5 from left to right at three different crank angle of 366, 376, 396 in mass fraction.

CHAPTER V

CONCLUSIONS AND FUTURE WORK

5.1 Conclusions

The present work focused on CFD simulations of diesel-methane dual fuel combustion in a single-cylinder research engine. The simulations were first validated with pure diesel combustion data over a range of engine loads from 2.5 to 7.5 bar brake mean effective pressure (BMEP) at a constant engine speed of 1500 rpm. Subsequently, the simulations were validated with diesel-methane dual fuel combustion data. Dual fuel combustion was examined across a wide range of methane percent energy substitution (PES) values from 30 percent to 90 percent at a constant engine speed of 1500 rpm and an engine load of 3.3 bar BMEP; in this regard, it may be noted that pure diesel operation corresponded to 0 PES. Finally a parametric study was performed to characterize the influence of increased swirl ratio on dual fuel combustion. The results obtained from the CFD studies lead to the following important conclusions:

- For diesel combustion, the simulations predicted the in-cylinder pressure evolution and the ignition delays with good accuracy. The first stage of the apparent heat release rate (AHRR) was predicted quite well but there were some discrepancies in the prediction of the second stage AHRR. These discrepancies were attributed to possible uncertainties in the model initial conditions such as the injection rate profile (which had to be assumed because it was not experimentally

available), the initial temperature and initial pressure at intake valve closing, the swirl ratio, the injection included angle, and the initial turbulent kinetic energy.

- The NOx emission trends for pure diesel operation were predicted correctly and the predicted NOx values were also reasonable close to the experimentally measured values at different loads. Soot emissions are not available from experiment, method to convert smoke number to engine specific emission value need to be formulated and compared it with simulation results.
- For dual fuel combustion, the simulation predicted pressure traces and ignition delays within accepted limits. The initial peak of AHRR was consistently over-predicted compared to experiments, likely due to some of the same uncertainties in initial and boundary conditions listed above for diesel combustion. Combustion phasing trends and value are well predicted for all cases.
- Emission trends of NOx, CO, and HC for diesel-methane dual fuel combustion were predicted correctly except for the highest PES value of 90 percent. Error in assigning initial condition like intake temperature, swirl ratio, initial kinetic energy and chemical kinetic mechanism may be reason for inaccuracy to predict correct emission value at 90 PES.
- Higher HC emissions for diesel-methane dual fuel combustion indicated ineffective combustion occurring inside the cylinder. With increasing PES, the HC emissions increased significantly. The increase in HC emissions were attributed to higher concentrations of unburned methane (at higher PES) originating from near the cylinder walls and the crevices present in the cylinder.

- The swirl ratio parametric study was performed to characterize the impact of swirl on combustion and emissions. Increasing swirl ratio improves combustion inside the cylinder as indicated by higher peak pressures and higher second stage AHRR. This enhanced combustion at higher swirl ratios led to a significant reduction in engine-out HC and CO emissions.
- When the swirl ratio was increased from 0 to 0.6, there was a slight increase in NOx emissions of about 4%, while the decrease in HC and CO emissions were 41% and 26%, respectively.

5.2 Recommendations for future work

Based on the CFD studies performed in this work, the following recommendations for future work can be proposed.

- Needle lift data available from the SCRE can be used for a better estimation of the diesel injection duration and diesel start of injection to improve simulation results.
- The diesel injection rate can be measured experimentally and fed into the simulation to improve simulation accuracy
- More accurate initial conations such as swirl ratio, temperature and pressure at IVC can be obtained using 1D simulation tool like GT POWER. and used to improve the accuracy of the simulations.
- Chemical kinetics needs to be validated under different engine operating conditions such as injection timing sweep, injection pressure and EGR condition

and check if it can predict LTC condition found in diesel-methane dual fuel combustion and improve chemical kinetics if needed.

- With these improvements, the combustion model can be used for optimization of dual fuel engine combustion and to find the optimized conditions for achieving lower HC and CO emissions, while maintaining the low NOx benefits of dual fuel combustion at medium and low loads.
- With these improvements of this model, combustion model can be used for optimization of dual fuel engine combustion and find optimized point for lower HC and CO emission maintaining lower NOx at medium or low load.

REFERENCES

[1] M.M. Abdelaal, A.H. Hegab, Combustion and emission characteristics of a natural gas-fueled diesel enginewith EGR, Energy Convers. Manag. 64 (0) (2012) 301–312.

[2] K.K. Srinivasan, S.R. Krishnan, Y. Qi, Cyclic combustion variations in dual fuel partially premixed pilot-ignited natural gas engines, J. Energy Resour. Technol.Trans. ASME (2014) 136(1), http://dx.doi.org/10.1115/1.4024855.

[3] U.S. Energy Information Administration, "Annual Energy Outlook 2017 with Projections to 2050," 0383(2017), (AEO2017).

[4] Wei L and Geng P 2016 A review on natural gas/diesel dual fuel combustion, emissions and Performance Fuel Processing Technology 142 264-278.

[5] Sundar Rajan Krishnan , Kalyan Kumar Srinivasan, Mostafa Shameem Raihan , The effect of injection parameters and boost pressure on diesel-propane dual fuel low temperature combustion in a single-cylinder research engine, Fuel Volume 184, 15 November 2016, Pages 490–502.

[6] SR Krishnan Biruduganti,Y Mo,S R Bell and KC Midkigg, Performance and heat release analysis of pilot-ignited natural gas engine,Int J Engine Research.vol.no.3 JER02201,2002

[7] E. Scott Guerry, Mostafa S. Raihan, Kalyan K. Srinivasan, Sundar R. Krishnan , Aamir Sohail, Injection timing effects on partially premixed diesel–methane dual fuel low temperature combustion, Applied Energy Volume 162, 15 January 2016, Pages 99–113.

[8] U.S. Environmental Protection Agency, “Greenhouse Gas Emissions and Fuel Efficiency Standards for Medium- and Heavy-Duty Engines and Vehicles— Phase 2’’ ENVIRONMENTAL PROTECTION AGENCY DEPARTMENT OF TRANSPORTATION, 73478-74274, 81 FR 73478

[9] Anderson, B., Bartlett, K., Frolking, S., Hayhoe, K., Jenkins, J. and Salas, W. (2010), Methane and Nitrous Oxide Emissions from Natural Sources, Office of Atmospheric Programs, US EPA, EPA 430-R-10-001, Washington DC

[10] Heywood, J. B. (1988). Internal combustion engine fundamentals. New York: Mcgraw-hill.

[11] Dec, J. E. (1997). A Conceptual Model of DI Diesel Combustion Based on Laser-Sheet Imaging. SAE Transactions, 106(3), 1319-1348.

[12] Dec, J. E. (2009). Advanced compression-ignition engines—understanding the in-cylinder processes. Proceedings of the Combustion Institute, 32(2), 2727-2742.

[13]. Krishnan, S. R., Gong, W., Fiveland, S. B., Srinivasan, K. K., Singh, S., Willi, M., ... & Midkiff, K. C. (2004). Strategies for reduced NOx emissions in pilot-ignited natural gas engines. Journal of engineering for gas turbines and power, 126(3), 665-671.

[14] Hanson, R., Kokjohn, S., Splitter, D., and Reitz, R., "An Experimental Investigation of Fuel Reactivity Controlled PCCI Combustion in a Heavy-Duty Engine," SAE Int. J. Engines 3(1):700-716, 2010, doi:10.4271/2010-01-0864.

[15] Northrop, W., Bohac, S., and Assanis, D. (2009), "Premixed Low Temperature Combustion of Biodiesel and Blends in a High Speed Compression Ignition Engine," SAE Int. J. Fuels Lubr. 2(1):28-40, doi:10.4271/2009-01-0133.

[16] Splitter, D., Reitz, R., and Hanson, R., "High Efficiency, Low Emissions RCCI Combustion by Use of a Fuel Additive," SAE Int. J. Fuels Lubr. 3(2):742-756, 2010, doi:10.4271/2010-01-2167.

[18] Kook, S., Bae, C., Miles, P., Choi, D. et al., "The Influence of Charge Dilution and Injection Timing on Low-Temperature Diesel Combustion and Emissions," SAE Technical Paper 2005-01-3837, 2005, doi:10.4271/2005-01-3837.

[19] Polk, A.C., Carpenter, C.D., Guerry, E.S., Dwivedi, U., Srinivasan, K.K., Krishnan, S.R., and Rowland, Z.L. . Diesel-ignited propane dual fuel low temperature combustion in a heavy-duty diesel engine. Trans. ASME: Journal of Engineering for Gas Turbines and Power, 136(9), 091509 (Apr 18, 2014), Paper No: GTP-14-1085; doi: 10.1115/1.4027189.

[20] Polk, A. C., Carpenter, C. D., Srinivasan, K. K., & Krishnan, S. R. An investigation of diesel–ignited propane dual fuel combustion in a heavy-duty diesel engine. Fuel, 132, 135-148.

[21] Karim, G. A. (2003). Combustion in gas fueled compression: ignition engines of the dual fuel type. ASME Journal of Engineering for Gas Turbines and Power, 125(3), 827-836.

[22] Sundar Rajan Krishnan, , Kalyan Kumar Srinivasan, Mostafa Shameem Raihan, The effect of injection parameters and boost pressure on diesel-propane dual fuel low temperature combustion in a single-cylinder research engine,Fuel Volume 184, 15 November 2016, Pages 490–502

[23] E. Scott Guerry, Mostafa S. Raihan, Kalyan K. Srinivasan, Sundar R. Krishnan, , Aamir Sohail, Injection timing effects on partially premixed diesel–methane dual fuel low temperature combustion, Applied Energy ,Volume 162, 15 January 2016, Pages 99–113

[24] LijiangWei, Peng Geng, A review on natural gas/diesel dual fuel combustion, emissions and performance, Fuel Processing Technology 142 (2016) 264–278

[25] Königsson, F., Dembinski, H., and Angstrom, H., "The Influence of In-Cylinder Flows on Emissions and Heat Transfer from Methane-Diesel Dual Fuel Combustion," SAE Int. J. Engines 6(4):1877-1887, 2013, doi:10.4271/2013-01-2509.

[26] Singh, S., Kong, S., Reitz, R., Krishnan, S. et al., "Modeling and Experiments of Dual-Fuel Engine Combustion and Emissions," SAE Technical Paper 2004-01-0092, 2004, doi:10.4271/2004-01-0092.

[27] Zhang, Y., Kong, S., and Reitz, R., "Modeling and Simulation of a Dual Fuel (Diesel/Natural Gas) Engine with Multidimensional CFD," SAE Technical Paper 2003-01-0755, 2003, doi:10.4271/2003-01-0755.

[28] Donateo, T., Strafella, L., and Laforgia, D., "Effect of the Shape of the Combustion Chamber on Dual Fuel Combustion," SAE Technical Paper 2013-24-0115, 2013, doi:10.4271/2013-24-0115.

[29] Abd Alla, G., Soliman, H., Badr, O., and Abd Rabbo, M., "A Computational Investigation of the Effect of Exhaust Gas Recirculation on the Performance of a Dual Fuel Engine," SAE Technical Paper 2000-01-2040, 2000, doi:10.4271/2000-01-2040

[30] Belaid-Saleh, H., Jay, S., Kashdan, J., Ternel, C. et al., "Numerical and Experimental Investigation of Combustion Regimes in a Dual Fuel Engine," SAE Technical Paper 2013-24-0015, 2013, doi:10.4271/2013-24-0015.

[31] Zhang, B., Mazlan, S., Jiang, S., and Boretti, A., "Numerical Investigation of Dual Fuel Diesel-CNG Combustion on Engine Performance and Emission," SAE Technical Paper 2015-01-0009, 2015, doi:10.4271/2015-01-0009

[32] Donateo, T., Carlucci, A., Strafella, L., and Laforgia, D., "Experimental Validation of a CFD Model and an Optimization Procedure for Dual Fuel Engines," SAE Technical Paper 2014-01-1314, 2014, doi:10.4271/2014-01-1314.

[33] Wang, M., Xu, Z., Li, M., and Lee, C., "Numerical Study and Parameter Optimization on a Diesel - Natural Gas Dual Fuel Engine," SAE Technical Paper 2016-01-0769, 2016, doi:10.4271/2016-01-0769.

[34] A.Rahimi, E Fatehifar, R Khoshbakhti Saray Proceedings of the Institution of Mechanical Engineers, Part D: Journal of Automobile Engineering Vol 224, Issue 9, pp. 1141 - 1159

[35] Wijeyakulasuriya S, Jupudi RS, Givler S, et al. Multidimensional Modeling and Validation of Dual-Fuel Combustion in a Large Bore Medium Speed Diesel Engine. ASME. Internal Combustion Engine Division Fall Technical Conference, Volume 1: Large Bore Engines; Fuels; Advanced Combustion ():V001T01A006. doi:10.1115/ICEF2015-1077

[36] Richards, K. J., Senecal, P. K., and Pomraning, E., CONVERGE (v2.3), Convergent Science, Madison, WI (2015). To refer to the company, use "Convergent Science".

[37] Senecal PK, Pomraning EE, Richards KJ, Som SS. Grid-Convergent Spray Models for Internal Combustion Engine CFD Simulations. ASME. Internal Combustion Engine Division Fall Technical Conference, ASME 2012 Internal Combustion Engine Division Fall Technical Conference ():697-710. doi:10.1115/ICEF2012-92043.

[38] Issa, R. I., "Solution of the Implicitly Discretised Fluid Flow Equations by Operator-Splitting," Journal of Computational Physics, Volume 62, 1986.

[39] Reitz, R. D., and Diwakar, R., "Structure of High-Pressure Fuel Sprays," SAE Paper No.870598, 1987

[40] O'Rourke, P. J., and Amsden, A. A., "The TAB Method for Numerical Calculation of Spray Droplet Breakup," SAE Paper No. 872089, 1987.

[41] Reitz, R. D., "Modeling Atomization Processes in High-Pressure Vaporizing Sprays, " Atomisation and Spray Technology, Volume 3, p. 309, 1987.

[42] Jennifer C. Beale,Rolf Deneys Reitz,' Modeling spray atomization with the Kelvin-Helmholtz/Rayleigh-Taylor hybrid model. Atomization Sprays 9:623-650, Atomization and Sprays · November 1999, DOI: 10.1615/AtomizSpr.v9.i6.40

[43] Schmidt, D. P., and Rutland, C. J., "A New Droplet Collision Algorithm," Journal of Computational Physics, Volume 164, p. 62, 2000.

[44] Naber, J., and Reitz, R. D., "Modeling Engine Spray/Wall Impingement," SAE Paper No.880107, 1988

[45] Senecal, P. K., Pomraning, E., and Richards, K. J., "Multi-Dimensional Modeling of Direct-Injection Diesel Spray Liquid Length and Flame Lift-off Length using CFD and Parallel Detailed Chemistry," SAE Paper No. 2003-01-1043, 2003.

[46] Raihan, Mostafa Shameem, "A comparative study of diesel ignited methane and propane dual fuel low temperature combustion in a single cylinder research engine, " MSSTATE, 2014

[47] Bohach Taylor C, "An experimental investigation of crank-resolved exhaust pressure profiles in a single cylinder research engine with emphasis on the potential of harvesting exhaust energy," MSSTATE, 2014